



DEGREE PROJECT IN ENGINEERING PHYSICS,
SECOND CYCLE, 30 CREDITS
STOCKHOLM, SWEDEN 2019

Investigating the Application of Self-Actuated Passive Shutdown System in a Small Lead-Cooled Reactor

GOVATSA ACHARYA

Master's Programme in Nuclear Energy Engineering (120 credits ECTS)

Investigating the Application of Self-Actuated Passive Shutdown System in a Small Lead-Cooled Reactor

Govatsa Acharya

TRITA-SCI-GRU 2019:127

SH204X: Master's Thesis (30 credits ECTS)

June 2019

Supervisor: Dr. Sara Bortot

Examiner: Prof. Janne Wallenius

Place: KTH Royal Institute of Technology

School of Engineering Sciences

SE-100 44 Stockholm, Sweden

The application of passively or self-actuated passive safety systems in nuclear reactors allow to simplify the overall plant design, besides improving economics and reliability, which are among the high-level goals set out by the Generation IV International Forum. This thesis focuses on investigating the application of a self-actuated, passive shutdown system for a small, modular lead-cooled fast reactor, and on its implications on the dynamic response to an initiating event. The application of passive shutdown systems for a lead-cooled reactor is not studied extensively, due to the general consensus that lead as a coolant, is too dense to achieve any passive shutdown by gravity. On the contrary, dense liquid lead as a coolant is viewed to be extremely efficient in buoyancy-driven passive shutdown.

Initially neutronic parameters were determined using a combination of Monte Carlo codes, OpenMC and Serpent, by carrying out sensitivity analyses on a critical, hot-state core at middle of life. The reactivity worths of the intended shutdown assemblies and control assemblies were then determined. According to a first-order approximation approach, the passive insertion of shutdown rods was assumed to be influenced by gravity, pressure drag and viscous drag due to flow against the assembly and finally the buoyant force.

Sensitivity analyses were performed for a spectrum of models with varied drag coefficients, in addition to determining the effect of addition of ballast to the assembly and finally to assess the effect of changing coolant flow rate. The time of insertion of the shutdown assembly from its parking position in the core was determined for each of these scenarios. An optimised shutdown foot profile was designed to allow the quickest passive insertion and then implemented in BELLA multi-point dynamics code, in order to perform dynamic analyses of a transient overpower scenario.

This study provides evidence for the viability and reliability of gravity-driven shutdown systems in a heavy liquid metal cooled reactor, and also providing specific data for buoyancy-driven insertion. Further studies could be carried out to investigate the application of such systems in different reactors cooled by, for instance, lead-bismuth or mercury, and also to improve the efficiency of safety systems in sodium cooled reactors.

SAMMANFATTNING

Tillämpningen av passiva, eller helt självaktuerade passiva säkerhetssystem i kärnreaktorer möjliggör förenklingar i den övergripande reaktordesignen. Utöver detta förbättras även ekonomin och tillförlitligheten, vilket är en del av de mål som satts upp av Generation IV International Forum. Detta examensarbete fokuserar på att undersöka tillämpningen av självaktuerade passiva säkerhetssystem i en liten, modulär blykyld snabbreaktor, och studera dess påverkan på det dynamiska svaret från en störning från jämviktsläget. Tillämpningen av passiva avstängningssystem i blykylda reaktorer är ett inte allt för välstuderat forskningsområde. Detta på grund av att rådande konsensus är att bly som kylmedium har en alldeles för hög densitet för att gravitationsdriven passiv avstängning skall vara möjlig. Flytande bly med hög densitet anses å andra sidan vara extremt effektivt vid flytkraftsdriven passiv avstängning.

Neutroniska parametrar bestämdes initialt med en kombination av de två Monte Carlo koderna OpenMC och Serpent genom att utföra känslighetsanalyser på en kritisk reaktor i ett varmt tillstånd och i mitten av bränslecykeln. Reaktivitetsvärdena hos reaktorns avstängningsknippen och styrvastknippen bestämdes därefter. I enlighet med en approximation av första ordningen antogs passiv införsel av avstängningsstavar enbart påverkas av gravitationen, formmotståndet, visköst motstånd orsakat av flödet längst med knippet och slutligen av flytkraften.

Känslighetsanalyser genomfördes för ett antal modeller med varierande motståndskoefficienter. Beteendet vid varierande ballast bestämdes, och slutligen bestämdes knippets beteende vid ett varierande flöde av kylmedium. Tiden det tar att föra in avstängningsknippena från deras parkeringsposition i reaktorhärden beräknades för vart och ett av de tidigare nämnda scenarierna. En optimal profil på avstängningsknippets fot togs fram för att uppnå den snabbaste möjliga passiva införseln av avstängningsknippena, och detta implementerades i BELLA, en multipunktdynamik kod, för att kunna genomföra dynamiska studier av ett transient scenario.

Denna studie ger bevis på gångbarheten och pålitligheten hos gravitationsdrivna avstängningssystem i en reaktor kyld av flytande metall, och den ger också data från en flytkraftsdriven införsel. Framtida arbeten kan utföras för att undersöka implementeringen av sådana system i andra typer av reaktorer kylda av, till exempel blyvismut eller kvicksilver, men också för att öka effektiviteten av säkerhetssystemen i natriumkylda reaktorer.

ACKNOWLEDGEMENTS

At the end of this extremely fruitful work and the wonderful two years in the beautiful city of Stockholm, the Author would like to express deepest appreciations to his colleague and friend Fredrik Dehlin, for all the stimulating discussions and debates and being a constant source of motivation throughout the duration of study.

The Author is grateful to Ignas Mickus for his suggestions, ideas and ability to answer difficult questions encountered during the thesis.

The Author would like to express his indebtedness to Janne Wallenius for being the foundations and granting support and freedom to work on *Blykalla Reaktorers* (LeadCold Reactors) novel reactor.

None of this would be possible without Sara Bortot, for her untiring, encouraging supervision and guidance helped complete this thesis. The Author is forever thankful to her, for believing in the work with a keen scientific temper and optimism and being there to listen to and resolve any and all the doubts and questions thrown at her.

Special thanks to *Vetenskapsrådet* (VR-Swedish Research Council) for funding this project.

Finally, no words would suffice to express heartfelt gratitude to the Author's family in India, for their blessings, support, encouragement and unending love.

The Author
Govatsa Acharya
Thursday 20th June, 2019

आपूर्यमाणमचलप्रतिष्ठं समुद्रमापः प्रविशन्ति यद्वत् /
तद्वत्कामा यं प्रविशन्ति सर्वे स शान्तिमाप्नोति न कामकामी //

श्रीमद् भगवद्गीता - २: ७०

“A person who is not disturbed by the incessant flow of desires—that enter like rivers into the ocean which is ever being filled but is always still—can alone achieve peace, and not the man who strives to satisfy such desires”

Śrīmad Bhagavadgītā – 2:70

List of Figures	i
List of Tables	iv
Preface	
1 Introduction	1
1.1 Motivation	3
1.2 Objectives	4
1.3 Thesis Organisation	5
2 Reactor Description	6
2.1 Plant Description	6
2.2 Core Description	8
2.3 Shutdown System	10
3 Background	11
3.1 Active Safety	11
3.2 Passive Safety	11
3.3 Inherent Safety	12
3.3.1 Reactivity Coefficients	13
3.4 Actively Actuated Systems	15
3.5 Passively or Self Actuated Systems	15
3.6 Current Experience	16
4 State of the Art	18
4.1 Literature Review	18
4.2 Computational Tools	19
5 Methods and Preliminary Study	21
5.1 1D Thermal Hydraulics Model	21
5.2 Hot Core Geometry Model	26
5.3 Neutronics Model	29
5.3.1 Results	35

6	Passive Shutdown System Design	50
6.1	Overview	50
6.1.1	Tungsten-Rhenium Diboride	51
6.2	Gravity Driven Insertion Model	53
6.2.1	Underlying Physics	54
6.2.2	Assembly Foot Design	64
6.2.3	Mathematical Model	70
6.2.4	Results	73
6.3	Buoyancy Driven Insertion Model	83
6.3.1	Underlying Physics	83
6.3.2	Results	84
6.4	Transient Analysis	91
6.4.1	Results	93
7	Summary and Conclusions	97
7.1	Practical Implications	98
7.2	Future Research	98
	References	99
A	Supplementary Data and Calculations	105
A.1	Convective Heat Transfer Coefficient	105
A.2	Thermal Expansion	107
A.3	Neutronics: Reactivity Coefficients	108
A.4	Transient Analysis	109

LIST OF FIGURES

1.1	Generation IV roadmap	2
2.1	Layout of 4 SEALER-UK unit plant	6
2.2	Layout of twin SEALER-UK units positioned underground	7
2.3	CAD representation of the SEALER-UK primary system	8
2.4	Coremap of SEALER-UK	10
5.1	Heat transfer from fuel to the coolant	21
5.2	Calculation scheme for the 1D T/H sub channel analysis	22
5.3	Predicted temperature profiles at steady state	24
5.4	Temperature profiles at steady state	25
5.5	Representative graphics of fuel rod and assembly wrapper	26
5.6	Parabolic excess reactivity profile	29
5.7	Core assembly multi-universe mapping	31
5.8	Axial slice and radial slice of the SEALER-UK fuel assembly	31
5.9	Radial slice of the SEALER-UK CR assembly, SD assembly and RF assembly	32
5.10	Axial slice of the core in YZ plane as modelled in OpenMC	33
5.11	Axial slice of the core in XZ plane as modelled in OpenMC	33
5.12	Radial slice of the SEALER-UK core showing the fuel assemblies, CR assemblies, SD assemblies and RF assemblies	34
5.13	k_{eff} evolution as a function time	35
5.14	Representative graphics for position of CR and SD assemblies	36
5.15	S-curve for CR bank	38
5.16	S-curve for SD bank	38
5.17	Assembly wise power distribution	39
5.18	Core averaged axial power distribution	39
5.19	Variation of reactivity with fuel temperature	42
5.20	Height of fuel pellet perturbed in fuel rod	43
5.21	Variation of reactivity with fuel temperature	43
5.22	Diameter of fuel pellet perturbed in fuel rod	44
5.23	Variation of reactivity with fuel temperature	45
5.24	Variation of reactivity with coolant temperature	46
5.25	Assembly wrapper pitch perturbed in the core	47
5.26	Variation of reactivity with diagrid temperature	48

5.27	Coolant void zones	49
6.1	Comparison of crystallographic structures for WB_2 and ReB_2	52
6.2	Density of $WReB_2$ for different tungsten fractions	52
6.3	Representative graphics of the shutdown assembly and the channel	53
6.4	Various forces acting on the body	55
6.5	Coolant density variation along the core height	58
6.6	Representative graphics showing different coolant zones	58
6.7	Representative graphics showing pressure and shear forces acting on a body in a flowing fluid	59
6.8	Average drag coefficient for cross flow over a smooth circular cylinder and a smooth sphere	61
6.9	The development of the boundary layer for flow over a flat plate and the different flow regimes	61
6.10	Plots of skin friction coefficient for smooth and rough flat plate at laminar, transition and turbulent flow regimes	63
6.11	Representative images of the considered profiles	65
6.12	Geometry images for different profiles	66
6.13	Mesh cross section for different profiles	67
6.14	Drag coefficients for different profiles	69
6.15	Drag coefficients for the 45° cone profile	70
6.16	Graphical representation of the fall	71
6.17	Calculation scheme for the 1D gravity driven insertion analysis	72
6.18	Variation of velocity and acceleration of the assembly	73
6.19	Variation of forces on the shutdown assembly	74
6.20	Variation of distance with time for different densities of assembly foot	75
6.21	Variation of time of insertion with assembly foot density	76
6.22	Assembly wise coolant velocity distribution	77
6.23	Variation of distance with time for different assembly coolant velocity	78
6.24	Variation of time of insertion with coolant velocity	79
6.25	Variation of distance with time for different form drag coefficients	80
6.26	Variation of forces on the shutdown assembly	81
6.27	Variation of velocity and acceleration of the shutdown assembly	82
6.28	Various forces acting on the body for the two cases	84
6.29	Variation of velocity and acceleration of the assembly	85
6.30	Variation of forces on the shutdown assembly	86
6.31	Variation of distance with time for different densities of assembly head/foot	87
6.32	Variation of time of insertion with assembly head/foot density	88
6.33	Variation of distance with time for different assembly coolant velocity	88
6.34	Variation of time of insertion with coolant velocity	89
6.35	Variation of distance with time for different form drag coefficients	90
6.36	Variation of time of insertion with drag coefficient	90
6.37	Schematics of the different components of BELLA	91
6.38	Schematics of the core components of BELLA	92
6.39	Schematics of the passive shutdown block of BELLA	93
6.40	Total power changes during transient overpower scenario	94
6.41	Total reactivity changes during transient overpower scenario	95

6.42	Reactivity changes of the shutdown system during transient over- power scenario for different cases of actuation	95
6.43	Temperature changes during shutdown delayed by the deactivation of the Curie point latch	96
A.1	Triangular sub channel in a hexagonal assembly	105
A.2	Temperature dependence of thermal expansion coefficient	107
A.3	Thermal expansion of each discretised element	108
A.4	Variation of reactivity with fuel clad temperature	108
A.5	Variation of reactivity with wrapper temperature	109
A.6	Reactivity coefficient contribution during transient overpower scenario	109
A.7	Coolant flow rate changes during transient overpower scenario	110
A.8	Total power changes during transient overpower scenario	110
A.9	Total reactivity changes during transient overpower scenario	111
A.10	Temperature changes during transient overpower scenario	111
A.11	Coolant flow rate changes during transient overpower scenario	112

LIST OF TABLES

1.1	Operable nuclear power reactors at year-end 2017	1
2.1	Key parameters of SEALER-UK	9
5.1	Parameters for T/H evaluation	25
5.2	Coefficient of thermal expansion correlations	27
5.3	Thermal expansion in materials expressed as percentages	29
5.4	CR bank and SD bank reactivity worth	37
5.5	Results for different insertion cases	37
5.6	Kinetic parameters at <i>MoL</i>	40
5.7	k_{eff} at different cross section temperatures	41
5.8	k_{eff} at different fuel axial expansions	44
5.9	k_{eff} at different fuel radial expansions	45
5.10	k_{eff} at different coolant temperatures	46
5.11	k_{eff} at different diagrid temperatures	47
5.12	k_{eff} at different void zones	48
6.1	Absorber theoretical density	51
6.2	(n,total) cross section	51
6.3	Dimensions of the assembly parameters	54
6.4	Characteristics of the three coolant zones	59
6.5	Areas of interest	63
6.6	Velocity considered for CFD simulations	66
6.7	Mesh statistics	68
6.8	FLUENT settings	68
6.9	Drag coefficients as computed by FLUENT	69
6.10	Times of insertion for different densities of assembly foot	76
6.11	Times of insertion for different assembly coolant velocity	78
6.12	Times of insertion for different drag coefficient cases	80
6.13	Dimensions of the assembly parameters	83
6.14	Areas of interest	83
6.15	Times of insertion for different densities of assembly head/foot	87
6.16	Times of insertion for different assembly coolant velocity	89
6.17	Times of insertion for different drag coefficient cases	89

The thesis describes the study performed during Master's program at KTH Royal Institute of Technology. The Author wishes to inform the reader that the topic for the thesis was broad and covered different fields, as is always the case in nuclear engineering design, starting from thermal hydraulics, thermal mechanics and neutronics to fluid mechanics.

The thesis, under the aegis of self-actuated passive shutdown systems for lead cooled reactors, was performed along with the Author's colleague, whose topic of choice had a synergetic approach, that required similar preliminary study, but eventually leading towards a different thesis. In order to avoid duplication of work, different approaches were chosen, for instance in neutronics the Author performed characterisation using a completely different code, that enabled to retain the uniqueness and novelty.

The preliminary study on thermal hydraulics required sharing the work to have a consensus on the geometry modelling of the core. The Author contributed to developing and debugging the code to perform sub channel analysis. The burnup calculations were performed by the Author's colleague, using Serpent Monte Carlo code, as the OpenMC code chosen by the Author did not have this ability at the time of this study. The work subsequent to the neutronics characterisation of the core was performed individually by the Author.

Several compromises had to be made with the methodology, due to constraints with computing resources, required for extensive fluid dynamic simulations in FLUENT or full core modelling in OpenFOAM. A quicker first order approximation route around these potentialities had to be adopted. It is also worthwhile to mention that some of the initial goals of the thesis were ambitious, and would have required more time and resources to accomplish them, and would be interesting research topic for the future.

The world needs a clean, carbon-free energy in order to combat climate change and reduce green house gas (GHG) emissions. The Paris Agreement [1] requires countries to restrict GHG emissions, to limit global temperature rise to 1.5°C by 2050. One of the main contributors to GHG is the energy industry, which accounts for 31% of the volume released to the atmosphere [2]. This arises from the fossil fuel based power plants. Countries are taking several measures to reduce their share of emissions, by moving to non fossil fuel burning plants. Nuclear energy is one such source that has consistently provided GHG free energy. According to *International Atomic Energy Agency* (IAEA), nuclear energy accounted for roughly 10% of worlds electricity generation [3]. As of 2017 it provided 2506TWh of electricity, with an installed capacity of 392GWe [4]. If the goal of limiting temperature rise within 2°C is to be met before 2050, the capacity of nuclear power has to increase to 930GWe [5], which would be 17% of global electricity production.

According to *World Nuclear Association* (WNA), the number of operable reactors at the end of 2017 stood at 448 with 4 new reactor coming online in 2018 and 54 under construction [4]. Table 1.1 summarises the types of reactor in operation. Light Water Reactors (LWRs) are the most popular reactor type, that includes the Boiling Water Reactors (BWRs) and Pressurised Water Reactor (PWRs), followed by Pressurised Heavy Water Reactors (PHWRs), Light Water Graphite-moderated Reactors (LWGRs) and Gas Cooled Reactors (GCRs). These reactors operate in a thermal neutron spectrum (neutron energy $<1\text{eV}$). Only a few Fast Neutron Reactors (FNRs) operate in a fast neutron spectrum (neutron energy $>1\text{keV}$).

Table 1.1: Operable nuclear power reactors at year-end 2017 [4]

Reactor type	No. of reactors
BWR	75 (-2)
FNR	3
GCR	14
LWGR	15
PHWR	49
PWR	292 (+3)
Total	448 (+1)

These thermal reactors have issues regarding sustainability and economics. They use Low Enrichment Uranium (LEU) as the fuel, resulting in inefficient utilisation of resources. They also operate on the direct cycle, where the final spent fuel is stored in disposal sites, though they still retain useful fuel resources. This issue could be resolved by developing fast spectrum reactors that not only efficiently utilise the fuel, but also support recycling of the spent fuel, thereby closing the fuel cycle. The new breed of reactors, termed *Generation IV* or *Gen. IV* reactors, are currently under research and development throughout the world. Figure 1.1 depicts the roadmap set up for the Gen. IV technology by the *Generation IV International Forum* (GIF). The reactors currently in operation over the world are Gen. III and lower, the first Gen. III+ reactor to come into operation was Novovoronezh II-Unit 1 in 2017 and Unit 2 was connected to the grid in May 2019 [4].

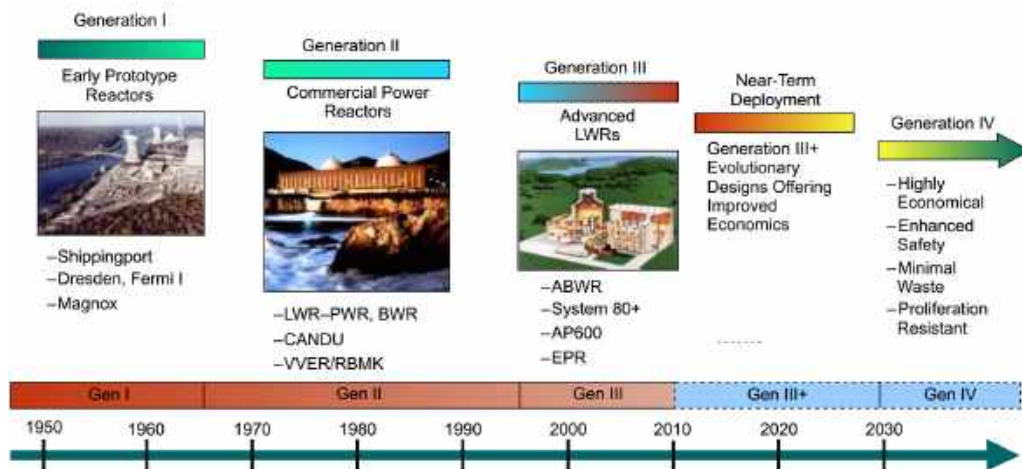


Figure 1.1: Generation IV roadmap [6]

The Gen. IV technology is being developed with a long term focus, with clearly defined goals. As defined by GIF, the high-level goals can be enumerated as:

- *Sustainability 1&2* - Gen. IV systems will be sustainable in the long run, meets GHG reduction terms, and utilises fuel effectively, with minimised waste production and subsequently improves the environment and public health.
- *Economics 1&2* - Gen. IV systems will have an economically viable approach to energy generation with advantageous life cycle costs and will be financially stable option with risks comparable to other energy systems.
- *Safety and reliability 1,2&3* - Gen. IV systems will provide superior safety and reliability, with minimised risk of core damage and lower severity in case of accidents. Gen. IV systems will also have enhanced mitigation systems necessitating no need for off-site emergency response.
- *Proliferation resistance and physical protection* - Gen. IV systems will adopt designs that increases impediments to proliferation, while also increasing physical protection against theft.

1.1 Motivation

Dutifully bound to the stated goals of Gen. IV systems, a new family of reactors is under active development at LeadCold Reactors (*Sv: Blykalla Reaktorer*) [7]. LeadCold is a spin-off company of KTH Royal Institute Technology Reactor Physics division. The company is working on the design, safety analysis and nuclear chemistry of fast neutron Gen. IV reactors. The company's flagship design, abbreviated for simplicity, is SEALER. The *Swedish Advanced Lead Reactor* (SEALER) is a small lead-cooled reactor designed to produce electricity in both off-grid and on-grid regions.

SEALER has a very small footprint, a non-refuelled core with a long life span. This serves to operate in inaccessible terrains and regions, which require continuous supply of power and heat. The Canadian variant of the reactor, SEALER-Canada [8], was designed for this very purpose, to be a safe, reliable and sustainable source of energy in the off-grid regions of the Arctic. This reactor can be accommodated for a power range of $3\text{-}10\text{MW}_e$. These design choices reflect the commitment to Gen. IV goals.

The small core is fuelled with uranium dioxide (UO_2) pellets, with enrichment slightly lesser than 20%, to achieve critical operation in a fast neutron spectrum. Lead is preferred as a coolant keeping in mind the objectives of sustainability and safety for such a small reactor. The adverse affects of employing lead have been mitigated by making use of novel techniques to create a barrier on the core structure surfaces and clad surfaces [8]. The design incorporates passive safety features to further enhance safety and security optics. Designing a small reactor, with passive features, without mid-life refuelling or reshuffling also makes it economically cheaper.

The aforementioned Canadian variant is a first generation SEALER design, owing to its fuel density and primitive performance. The next generation of the reactors are fuelled by a denser uranium nitride (UN) fuel, facilitating better utilisation and performance [7]. This UK variant, expanded as *Small, Economic and Agile Lead-Cooled Reactor for the United Kingdom* (SEALER-UK) is a small, modular, lead-cooled fast reactor (LFR) designed to produce 55MW_e (or 140MW_{th}) of power. LeadCold envisages this reactor to be a very inherently and passively safe. The design also features a small battery-like design, requiring no refuelling or reshuffling. The modular characteristic enables easy transportation and installment, at reduced costs. These and many other proposed features for this reactor make it a very competitive Gen. IV design.

As mentioned earlier, SEALER-UK is the latest design in this family, under constant research and development. Being a new entrant in the Gen. IV space, the reactor has to undergo robust study and analysis. SEALER-UK was among the few reactors chosen by the UK government to be studied for feasibility and economic viability in the UK [9],[7]. This resulted in a contract being awarded to LeadCold to further develop certain aspects of the proposed design and make a detailed study on safety features. Further, the Swedish Research Council (*Sv: Vetenskapsrådet (VR)*) grant was awarded to develop and assess aspects relating to safety, in particular, passively operable, either self actuated or actively actuated, shutdown systems that can act reliably for a variety of accident scenarios and also to investigate the feasibility of employing self actuating passive safety systems in liquid

metal cooled reactors. These broad aims are expressed as the following goals.

- *Development of computational tools and its benchmark. Substantial progress has been made in developing code systems such as BELLA [10], FAST [11] and GeNFoam [12].*
- *Determination and setup of framework for the interaction of control systems and safety in accordance with GIF's Integrated Safety Assessment Methodology (ISAM) [13]*
- *Assessment of available passive safety systems, modelling, characterisation and its development for application in different reactor technologies.*
- *Development of control strategy and control system architecture.*
- *Complete safety assessment incorporating all the above objectives.*

The approach to a safety-informed design requires development of tools and systems to analyse for various scenarios. The emphasis in the Gen. IV technology development is on passive and inherent safety. To this effect, one of the features of the reactor, namely passive shutdown and safety is the locus of this thesis.

1.2 Objectives

The motivation, discussed previously, puts forth certain milestones that needs to be achieved. This study will focus mainly on the passive safety aspects and its consequences on reactor dynamic safety. SEALER-UK is the reactor design that the proposed systems will be investigated. While this is the immediate goal of the study, the application of the passive safety systems to other kind of reactors will be undertaken. The initial objectives of the thesis is as follows:

- SEALER-UK reactor characterisation - This involves preparing the core model at a critical point of its life cycle followed by performing static neutronic calculations using a Monte-Carlo code.
- Neutronic characterisation of the shutdown assemblies - This involves mapping the reactivity worth of the shutdown rods at different positions in the core. This is accomplished by making use of a Monte-Carlo code.
- Development of self actuated passive shutdown system for SEALER-UK - This involves study on the passive gravity-driven and buoyancy-driven insertion of shutdown assembly, with detailed analysis to optimise the assembly aiming to reduce insertion times.
- Dynamic safety assessment of the designed system using multi-physics transient analysis tools - This involves of dynamic simulation of the intended shutdown system using the state-of-the-art multi-physics solver GeNFoam that is based on OpenFOAM. Additionally the system is to be incorporated in BELLA, the multi-point dynamics code, that is modified to the SEALER-UK characteristics, and the reactor's response to transients will be studied.

1.3 Thesis Organisation

The thesis is arranged as follows. Chapter 2 provides the relevant information about the reactor and the proposed plant design. The key parameters of the core are explained and a general outline of the shutdown system is provided.

Chapter 3 delves into the background necessary to understand the concepts that will be discussed later on in the thesis. This chapter gives a comparative description of active safety systems, passive safety systems and inherent safety systems. At the end of the chapter the current experience in dealing with passive systems is provided.

Chapter 4 presents a literature survey of the available data regarding passive shutdown system that can be used in numerical modelling of gravity-driven and buoyancy-driven systems. The chapter also outlines the major software tools that were useful in performing the study.

Chapter 5 gives a comprehensive analysis of preliminary thermal hydraulic, thermo mechanical and neutronic characterisation of the core starting from first principles. The results obtained from the preliminary study is also discussed here.

Chapter 6 focuses on the entire design and analysis of the shutdown system, both driven by buoyancy and gravity. The methodology of the analysis, the background of the proposed materials and conservative sensitivity analysis of critical parameters is discussed. A dynamic response of the core to an overpower transient is also explained.

Finally Chapter 7 gives concluding remarks, implications, key recommendations and possible future work associated with the thesis.

2.1 Plant Description

The plant design and configuration is presented in the SEALER-UK feasibility report. The overall objectives of the reactor plant is listed:

- Preferred plant accommodates four reactor units, producing $220MW_{th}$ electricity for 25 calendar years of operation.
- Plant availability of 90% with power conversion efficiency $>40\%$.
- Limiting on-site construction time to <24 months.
- Passivise core safety features, thereby reducing safety systems.
- Nuclear battery design, no refuelling, reduced operational maintenance.

Figure 2.1 shows the conceptual layout of the plant built with four units of the $55MW_e$ reactors sharing a common turbine building. Also seen in the figure are the eight cooling towers acting as ultimate heat sink and four stacks on each reactor building for auxiliary cooling systems.

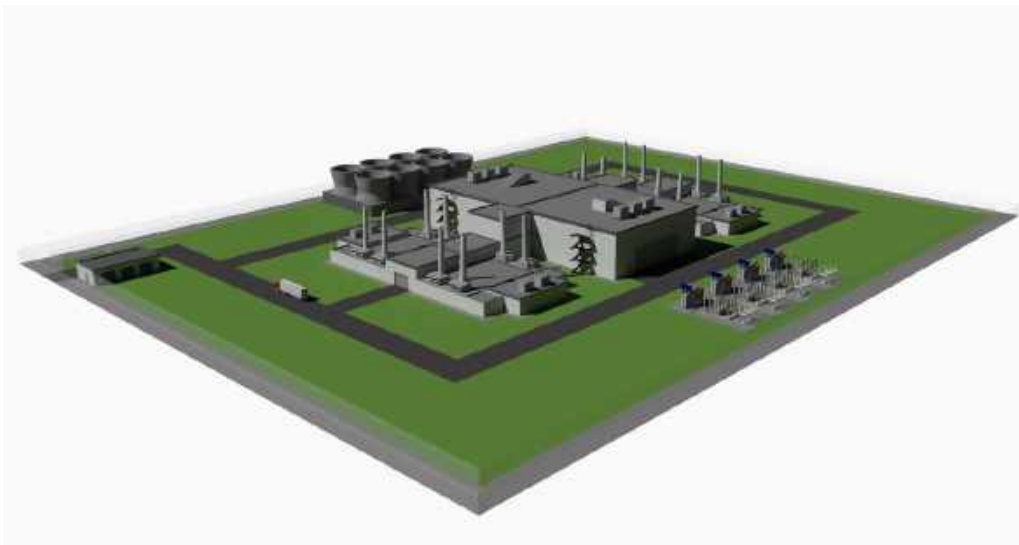


Figure 2.1: Layout of 4 SEALER-UK unit plant [Published with permission from LeadCold]

The reactor layout have the benefit of flexibility of location either below-surface or over-surface. Minimisation of cost of shielding from air-borne accidents and environmental shielding is achieved by having the reactors underground, as shown in Figure 2.2. In low lying areas prone to flooding, the reactor can be located over-ground. The reactor is submersed in the reactor cavity with water being the passive decay heat removal system.



Figure 2.2: Layout of twin SEALER-UK units positioned underground [Published with permission from LeadCold]

Being a small and modular reactor has its advantages. The plant is designed with ninety different systems which is markedly lesser than systems incorporated in LWRs. Implementing passive, self actuated systems reduces the complexity of the plant further. Each reactor unit is equipped with a slew of safety systems. These include the *Reactor Vessel Auxiliary Cooling* (RVAC) systems, *Direct Reactor Auxiliary Cooling* (DRAC) systems, *Passive Decay Heat Removal System* (PDHRS), reactivity control and shutdown systems, to name a few. The modular reactor has a carefully designed primary system. This includes the three vessels, *core barrel*, *primary vessel* and *guard vessel*, lids, pumps for forced coolant circulation and steam generators for power conversion.

The core barrel envelops the core and acts as a barrier between the cold leg and hot leg. The primary vessel is the next barrier that houses all the primary system components. The coolant in the primary system is not pressurised however, to prevent coolant loss due to any rupture in the primary vessel, it is encompassed in the guard vessel. Figure 2.3 depicts the primary system as a CAD model.

Overall the vessel dimensions are such that they could be transported along UK's railroad with little inconvenience. The cross section of the vessel show the fuel assemblies inside the core barrel, surrounded by the cold leg and the pumps and steam generators in the upper portion of the hot leg, numbering ten each. The height of the steam generators from the cold leg, that is the distance between thermal centers of hot leg and cold leg, is optimised to facilitate natural convection in case of a *loss-of-flow* accident. The control systems and the proposed shutdown systems are located above the core. It is this proposed shutdown rods that is the focus of this thesis. The following section gives an overview of the reactor core.

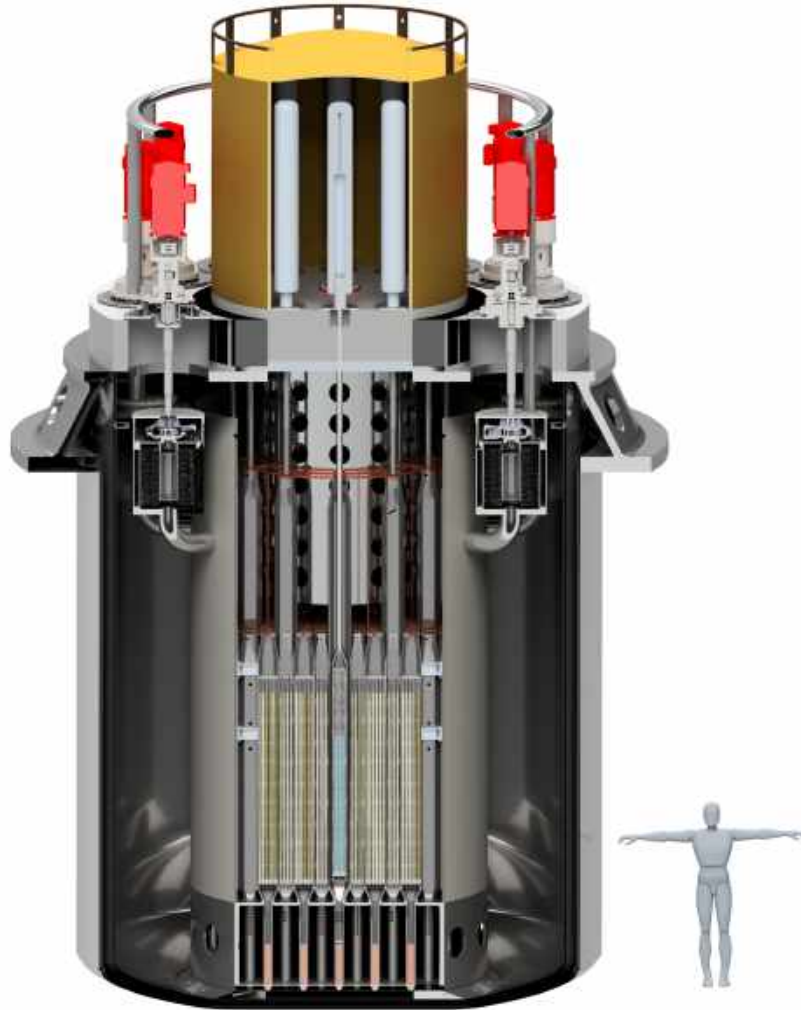


Figure 2.3: CAD representation of the SEALER-UK primary system [Published with permission from LeadCold]

2.2 Core Description

The core is small, power-dense and made of hexagonally arranged fuel assemblies. The nitride fuel is made of 11.8% enriched *uranium-235* (U^{235}) with the nitrogen being enriched to 99.5% in *nitrogen-15* (N^{15}), which is necessary to limit the formation of *carbon-14* (C^{14}) from *nitrogen-14* (N^{14}), which has high absorption cross section. Nitride fuel is the obvious choice to achieve the objective of designing a very compact core, with enhanced fuel performance at reduced costs. The burnup attained by the core and the subsequent reactivity swing is minimised which further reduces the necessity of having an expensive control system. Good thermal conductivity, comparatively high pellet density and the high melting point of nitride fuels also permit higher power density. Nitride fuel brings to the design table its own challenges. One of them is the *pellet-clad mechanical interaction* (PCMI) that tends to happen when achieving high burnup, due to high fuel swelling [14] that have lead to several pin failures in the past. This entails having a fuel-pellet gap filled with pressurised *helium* to avoid PCMI. Lead as a coolant along with considerable amount of fast fluence in the core reduces the options available for clad material.

To mitigate this, the much effective austenitic grade $1515Ti(Si)$ steel is employed, that is proven to have good creep properties but less than preferable corrosion resistance in a lead environment provided a suitable coating of alumina forming alloys is given to the clad tubes. This coating is achieved by pulsed electron beam GESA process [15] of 6% *aluminium* containing *FeCrAl-RE* steel. This ferritic steel with 4% *aluminium* is used as the structural material for the clad in shutdown rods, reflector rods and hex-cans. *FeCrAl-RE* is modified *FeCrAl* steel alloy consisting of Reactive Elements (Ti, Zr, Nb, Y) to achieve good thickness of the coating [16]. The key core parameters of SEALER-UK are provided in Table 2.1.

Table 2.1: Key parameters of SEALER-UK

Parameter	Value	Units
Fuel element	Uranium Nitride	
Thermal power	140	MW
Fuel enrichment	11.8	$\%wtU^{235}$
Theoretical density	14.3	g/cm^3
Fuel assemblies	85	Hexagonal lattice
Fuel pins/assembly	271	
Active zone (DxH)	2.04x1.30	m
Primary vessel (DxH)	4.2x6.0	m
Coolant	Lead	
Core inlet temperature	420	$^{\circ}C$
Core outlet temperature	550	$^{\circ}C$
Coolant flow rate	7410	kg/s
Coolant pressure	1	atm
Pumps/steam generators	10/10	
Control element	Boron Carbide	
Boron enrichment	19.9	$\%wtB^{10}$
Theoretical density	2.5	g/cm^3
Control assemblies	6	Reactor edge
Control rods/assembly	19	
Shutdown element	Tungsten-Rhenium Diboride	
Tungsten diboride fraction	48	$\%atWB_2$
Theoretical density	12.3	g/cm^3
Shutdown assemblies	6	Reactor corner
Shutdown rods/assembly	7	
Reflector element	Yttrium Stabilised Zirconia	
Theoretical density	6.3	g/cm^3
Reflector assemblies	72	
Reflector rods/assembly	37	

The coremap of the reactor is shown in Figure 2.4. The control assemblies and shutdown assemblies are shown extracted. The control assemblies are positioned along the reactor edges. This system enables maintaining criticality of the core, by compensating for the reactivity swing due to burnup. The control rod absorber pellets are made of conventional *boron carbide* (B_4C) consisting of natural boron. While there are better neutron absorbers with higher absorption cross section than

boron, the requirement of reactivity worth of a single assembly being minimised, to less than 0.2\$, enables the use of suitable and stable form of boron as a carbide.

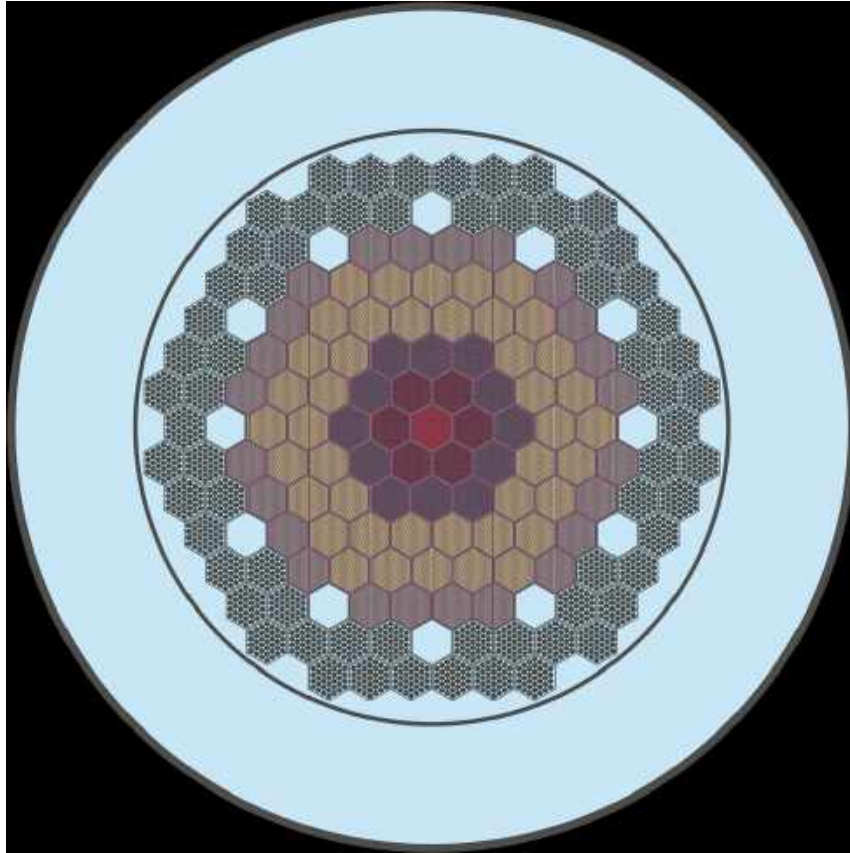


Figure 2.4: Coremap of SEALER-UK [Published with permission from LeadCold]

The core is surrounded by radial reflectors, to keep the core critical by reflecting leaking neutrons into the core and to also limit neutron damage to the core barrel. *Yttrium stabilised zirconia (YSZ)* is the material making the reflector rod pellets. *Zirconium nitride (ZrN)* acts as the insulator and reflector, above and below the fuel pellet, respectively. The fuel rod, in addition to the fuel pellet and *ZrN* insulators, consists of a lower *B₄C* shield and an upper fission gas plenum. The gas plenum is necessary to accommodate the volatile fission products formed due to burnup, and also since the nitride fuel is not very effective retainer of gaseous products. A pre-stressed spring holds the fuel rod components in place inside the clad.

2.3 Shutdown System

LeadCold envisages an unconventional shutdown system for SEALER reactors. The proposed shutdown rod absorber is a novel material that has a theoretical density greater than liquid lead. The super-hard metal boride is composed of *tungsten rhenium diboride (WReB₂)*, which has been synthesised and studied very recently [17], [18]. The rationale for opting this absorber is that the reactor can exploit the passive feature of gravity assisted insertion. This would enable simplification and enhance reliability of the essential safety system, that would be beneficial from economic standpoint as well.

It is necessary to distinguish some aspects relating to these systems: *active safety systems*, *passive safety systems* and *inherent safety systems*. Often missed is the demarcation between passive safety and self actuated passive safety, that warrants some explanation. These concepts are explained forthwith.

3.1 Active Safety

Active safety refers to systems that intend to protect from an abnormal event. These systems may be activated by human intervention or by automatic control systems that senses abnormal operation. These engineered systems rely predominantly on some form of electric power or external mechanical force to perform their intended function of thwarting a severe accident. Systems that provide active safety may include electric motors, pumps and hydraulics, electromagnets, that are termed *active components*. The burnup control system is an example of active safety system. It serves to compensate for increased reactivity, constantly adjusting the inserted height by appropriate actuators, to maintain a critical power level.

Conventional LWRs have a multitude of active systems in place such as safety injection systems, automatic depressurisation systems, containment spray systems, chemical and volume control systems. These systems actively sense the operating conditions and any deviation from normalcy will activate them. Active safety requires continuous supply of power for reliable function. Station blackouts and failure of backup power will quickly lead to runaway conditions, similar to the accident faced in Fukushima Daiichi [19]. This shows active safety necessitates backup systems that are redundant to primary systems. Active systems also require thorough risk and failure assessments and validations that tend to incur financial costs.

3.2 Passive Safety

IAEA defines a passive system as that which either majorly comprises of passive components or makes limited use of active components to activate a passive operation [20]. Passive components unlike active component requires no input or action to function. These components instead rely on material physical properties, laws of

nature or stored energy. External disturbances such as loss of electric power, that seriously hamper functioning of active system, has no such adverse effect of passive systems. Dependence on natural laws, that are consistent everywhere, increases reliability in comparison to dependence on backup systems, human intervention to provide redundancy in case of failure. There are shortcomings in passive systems with regards to failure resulting from mechanical wear, structural failure or human error.

Since the definition of passive safety is conditional, the *passivity* of the system can be categorised. Certain systems that have no active components may rank high in passivity than systems having some active component. There are systems that have features intermediary between active and passive definitions, where part of the function is handled by external agent and subsequent function is passive or vice versa. The spectrum in between the two can be loosely categorised as [20]:

- *Category A* - Systems with no input signal, no external forces or power sources, no moving mechanical parts or working fluids. Barriers such as primary vessels, reactor containment come under this category.
- *Category B* - Systems with no input signal, no external forces or power sources, no moving mechanical parts but with moving fluids. Emergency cooling system with boron injection achieved due to hydrostatic instabilities, passive decay heat removal system are examples for this category.
- *Category C* - Systems with no input signal, no external forces or power source, but with moving mechanical parts irrespective of moving fluids. Overpressure protection devices based on fluid release through valves is one such example.
- *Category D* - Systems where actuation is accomplished by an active component while execution is passive. Emergency core cooling systems based on gravity driven flow falls under this category.

Passive systems having a failure-proof design is economical as it reduces the cost of having additional redundant systems and simplifies the control strategy. This simplification also adds to reducing human error during critical operations.

3.3 Inherent Safety

While sometimes difficult to distinguish from passive safety, inherent safety has a different approach to safety, by making informed conceptual design and material choice [20]. The safety is intrinsic to the fundamentals of reactor operation. Material choice of the fuel, clad, structures, coolant and their associated thermo-chemistry and thermo-mechanics play an important role in the reactor. Hazards associated with abnormal phenomenon related to the above are inherent hazards. It is the aim of an inherently safe design to eliminate such hazards. While none of the practical reactors can eliminate all possible intrinsic hazard, it can achieve inherent safety with respect to elimination of a that particular hazard. A reactor that is inherently safe implies that it is absolutely safe in any adverse condition.

3.3.1 Reactivity Coefficients

Objective of any design is to increase safety, ideally having completely deterministic safety. Any deficiency in accomplishing this is compensated by having engineered safety (*passive* or *active safety*). These engineered systems aim to improve reliability, while still having a probability of failure, unlike inherent safety characteristics. It is here that rigorous testing and validation of systems to diverse operation conditions helps alleviate risk of failure. Relevant inherent safety characteristics in a fast reactor (FR) are the feedback reactivity coefficients, which are defined solely by the choice of design and materials. These coefficients contribute to safety when the reactor is perturbed from nominal operating conditions, such as material temperature changes affecting density and dimensions [21]. Consequently the temperature reactivity coefficient can be considered to be sum of these individual temperature coefficients of nuclear, density and volume changes. Equation 3.1 gives the relation between the multiplication factor and the reactivity.

$$\rho = \frac{k_{eff} - 1}{k_{eff}} \quad (3.1)$$

The effective neutron multiplication factor is represented by the *six-factor formula* as in Equation 3.2. η is the thermal fission factor, f is the thermal utilisation factor, p is resonance escape probability, ϵ is fast fission factor, L_f and L_t are fast and thermal non-leakage probability. The reactivity coefficient is interdependent on these factors.

$$k_{eff} = \eta f p \epsilon L_f L_t \quad (3.2)$$

The reactivity coefficient as a consequence of change in temperature is expressed as Equation 3.3. The coefficients can be consequences of temperature change of the fuel or moderator or any other component, each behaving differently. Some of the more relevant of these coefficients are explained below.

$$\alpha = \frac{d\rho}{dT} \quad (3.3)$$

- *Doppler coefficient* - This coefficient is driven by the changes in temperature of certain elements. Temperature affects the resonance escape probability of neutrons due to changes in spectral lines. The atoms owing to temperature have their resonance peaks broadened which increases neutron capture. Depending on the neutron spectrum of the core, increase in temperature can increase this probability of capture leading to a negative temperature coefficient (fissionable U^{238} fuels), or reduce the probability of capture at resonance cross section leading to positive temperature coefficient (fissile U^{235} fuels). This coefficient is widely called *fuel temperature coefficient* (FTC) or *Doppler coefficient* due to Doppler broadening of resonance peaks, similar to the effect seen in light and sound waves. The Doppler coefficient is negative in low enrichment fuels, as the resonance absorption in U^{238} , that would lead to non fission capture, exceeds that of U^{235} , that would lead to more fission capture. Harder spectrum, as in the case of nitride fuels, tends to have lower Doppler coefficient as the resonance region does not extend far into high neutron energies. Since this effect is inherently linked to temperature and directly dependent on neutron

population behaviour, its effect is instantaneous and is one of the first safety parameter against abnormal events.

- *Moderator temperature coefficient* - This is that component of reactivity which measures the effect of change in coolant temperature. Additionally, changes in coolant pressure and its effect is measured by the *moderator pressure coefficient*, that has higher significance in PWRs than FRs. Changes in moderator temperature however, result in changes in density. Decreasing density with increasing temperature results in reduced moderation and increased leakage that adds to negative reactivity in under-moderated LWRs, and positive reactivity in over-moderated LWRs. In *sodium-cooled fast reactors* (SFRs) however while the effect of leakage is to reduce reactivity, the reduced moderation and subsequent hardening of the spectrum tend have either positive or negative effect on reactivity depending on fuel composition. The net effect of the leakage component may be positive or negative [22]. In LFRs increasing temperature reduces density of coolant more than in SFRs, increasing the prominence of design on *moderator temperature coefficient* (MTC). The coefficient is more popularly known in context of fast reactors as *coolant density coefficient*, rather than MTC, because in FRs coolant does not perform the role of moderation to an extent as in LWRs. In addition to spectral hardening and increased leakage, parasitic capture in lead contributes to this coefficient. Parasitic capture is not an issue in sodium coolant, however it adds to the reactivity in LFRs. Reduced density implies fewer lead atoms absorbing neutron, which increases neutron economy and hence the MTC. The sign is generally positive unless specifically designed to achieve negative reactivity coefficient.
- *Coolant void coefficient* - Generally speaking LWRs are designed considering formation of steam bubbles in the core, and in the thermal spectrum these bubbles tend to reduce reactivity due to reduced moderation. The void coefficient is therefore negative. CANDU reactors operating with separate coolant and moderator have a small but positive void coefficient, that pose no serious risk to the reactor [23]. Formation of voids pose a similar effect as increasing the moderator temperature, in SFRs. Careful design of the core geometry and the fuel can achieve negative void effect. Voiding in LFRs is dominated by neutron scattering effect, that results in a positive reactivity.
- *Dimensional coefficient* - Core dimensions are linked to its operating temperature, that when changes, will lead to thermal expansion or contraction. When temperature of the fuel pellet increases, it leads to both axial and radial thermal expansion. Considering only the increase in surface area due to expansion, will lead to increase in neutron leakage bringing down the neutron economy. This is true for changes in dimensions of the fuel and overall core. The fuel axial coefficient is more prominent than radial coefficient, as there is partial insertion of control rods due to axial expansion, which has more contribution to reducing reactivity. However, changes in the fuel assemblies themselves, due to expansion in core support structure, tend to reduce fast fission, due to increased leakage and coolant moderation in fast reactors. From neutronics perspective fast reactors are more critical when the fuel is compacted and dense, in contrast to LWRs which require intermediary moderation for ther-

mal fission to occur. So radial core expansion is detrimental to the fission process, subsequently aiding to negative reactivity.

Combination of the first three coefficients is called the *power coefficient*, which gives the overall effect of a perturbed parameter on the total power of the core. A core is designed to have a negative power coefficient to improve intrinsic safety. Intrinsic safety is not limited to the aforementioned coefficients alone. Several other design characteristics add to inherent safety. The coefficients explained here under this context are useful later in the thesis.

3.4 Actively Actuated Systems

From earlier discussion, it is evident that certain systems cannot "think" on its own and require an active component to initiate the operation. Such systems that are initiated by means of active components are called actively actuated systems. Actively actuated systems rely on a host of sensors, monitors, instrumentation and automatic control to detect any unusual incident. These sensors and monitors (such as thermocouples, neutron flux monitors, pressure gauges, flow monitors *et cetera*) continuously send signals to a computer that assesses the situation. Sensing unusual conditions in the particular parameter, the computer signals the systems designed to mitigate that particular abnormality to act. While modern designs try to replace them with passive systems, achieving full passivity has a long way to go, for active systems have been in use for a long time, are cheaper than passive systems and have been thoroughly validated. Several such active components may actuate a single system, for example a shutdown system may be triggered for different accident scenarios, involving various sub-systems, nevertheless eventually shutting down the reactor. It is worth noting that while initiation is active, operation can be either active or passive.

3.5 Passively or Self Actuated Systems

Similar to a passively operable system, passive or self actuation means that the process of activation is independent of electric signals and is reliant on natural phenomenon. Limiting the scope of discussion to the case of shutdown systems, the *self actuated shutdown system (SASS)* are generally triggered by changes in coolant temperature or coolant flow characteristics. What *SASS* contributes to the reactor is inherent safety, with the entire system contained inside the reactor reducing complexity, minimising size and improving economics and reliability. Such systems are immune to human intervention, power failures or incorrect sensor readings [24]. What is essential for a self actuated component is that it should perform *sensing function*, *triggering function* and it should have *locking and release function*. The component should also be *fail safe*, defined by IAEA [20] as the behaviour of a system or a component following failure, that nevertheless performs intended function. Implementing such devices adds to redundancy, diversity and independence of the shutdown system [25].

Depending on the natural phenomenon the device is based on, SASS have varied conceptual designs. A few of the devices that could potentially be implemented in LFRs are listed [25]:

- *Lithium expansion module* - LEM makes use of Li^6 absorber suspended, from a reservoir placed near the core outlet, by the surface tension of the liquid gas interface just above the active zone. Any increase in outlet temperature expands the lithium which forces down the liquid gas interface thereby introducing negative reactivity, as Li^6 is a good neutron absorber. This device is also capable of providing positive reactivity by having positioned the liquid gas interface inside the active zone.
- *Lithium injection module* - LIM injects Li^6 into the active zone from a reservoir with pressurised gas, that has a thermal freeze seal which melts when core outlet temperature increases beyond its melting point.
- *Curie point latches* - These devices are electromagnetic latches that hold on to an armature when it is magnetised. Any rise in coolant temperature beyond the Curie point of the electromagnet, results in loss of magnetic force, detaching the armature.
- *Enhanced thermal effect mechanism* - This device consists of temperature sensitive elements that respond to various effects like thermal expansion, shape-memory or phase transition, that are triggered by increasing coolant outlet temperature. Thermostatic switches are another type of passively activated devices that cuts the power supply to an electromagnet holding the shutdown rods.

The devices mentioned here are quite modern inventions that require rigorous testing and validation for a variety of accident scenarios. Japanese fast reactor program RAPID [26] proposes to use the LEM and LIM as the means to improve inherent safety. Comparative assessment of the many available SASS devices pointed out that electromagnetic latch and thermostatic switch have better performance in *anticipated transient without scram* (ATWS) [27]. Study on SASS for SEALER-UK is beyond the scope of this thesis, and is of interest for future research.

3.6 Current Experience

The available literature on the passive shutdown system designs for *liquid metal cooled fast reactor* (LMFR) is quite minimal. There is no robust working experience in passive shutdown systems in LMFRs, however innovative and modern reactor concepts propose to adopt such systems. With specific regards to gravity driven shutdown systems, it is CANDU reactors that currently operate with such passive shutdown system, in addition to a secondary boron injection shutdown system [23]. LMFRs that propose the use of gravity or buoyancy assisted shutdown are:

- *ALFRED* - Advanced Lead Fast Reactor European Demonstrator is a pool type lead cooled $300MW_{th}$ reactor developed under the Lead cooled European Advanced Demonstration Reactor (LEADER) program. The reactor is implemented with two independent, redundant and diverse shutdown systems, where one of the systems passively insert shutdown assembly by buoyancy and the second system inserts absorber rods by pneumatic system [28].

- *MYRRHA* - Multipurpose hYbrid Research Reactor is an *accelerator driven system* (ADS) reactor developed by SCK-CEN operating with *lead-bismuth eutectic* (LBE) as the coolant. It incorporates diverse shutdown systems that are inserted passively by buoyancy and gravity [29].
- *SVBR 75/100* - This is an 75-100 MW_{th} LBE reactor where the safety rods incorporate fusible locks which passively inserts the rods when coolant temperature exceeds its melting point [30]
- *PEACER/PASCAR* - Proliferation-resistant, Environment-friendly, Accident tolerant, Continual and Economical Reactor developed by NuTrECK is a LBE cooled fast reactor for power production and waste transmutation with two power ratings, 850 MW_{th} and 1560 MW_{th} . PEACER employs an active reactivity control system and two shutdown systems. One of them is motor driven active system, where as the second is a passive gravity driven shutdown system [31]. Developing on this design a smaller 100 MW_{th} Proliferation-resistant, Accident-tolerant, Self-supported, Capsular and Assured Reactor (PASCAR) incorporates a buoyantly driven shutdown system [32].
- *MONJU/DFBR* - The prototype fast breeder reactor MONJU is a sodium cooled 714 MW_{th} reactor built in in 1994 incorporated a SASS device to achieve gravity driven insertion. It however, could not perform tests as the reactor suffered sodium fires and was ultimately closed down. The Demonstration Fast Breeder Reactor is a 1600 MW_{th} sodium cooled reactor similar to MONJU, implementing *SASS* as a backup reactor shutdown system [33].
- *JSFR* - The Japanese Sodium cooled Fast Reactor is a next generation reactor successor to the DFBR that has advanced inherent/passive safety systems. The reactor also includes the much validated *SASS* as the third device in the backup shutdown system driven by gravity [34].
- *URANUS* - The Ubiquitous, Rugged, Accident forgiving, Non proliferating, and Ultra lasting Sustainer is a LBE cooled 100 MW_{th} reactor designed by KAERI. This reactor employs an ultimate shutdown system consisting of boron stainless steel balls that are passively inserted into the core by buoyancy, when the fusible plug holding the balls melts [35].
- *PGSFR* - The Prototype Gen. IV Sodium cooled Fast Reactor developed by KAERI adopts a passively gravity driven shutdown system in conjunction with a temperature sensitive SASS in addition to a secondary control rod drive mechanism (SCRDM) [36].
- *PFBR* - The Prototype Fast Breeder Reactor developed by IGCAR is a sodium cooled, pool type 500 MW_e reactor. In addition to having a negative void coefficient it comprises of Curie point magnets to actuate the passive insertion of shutdown rods by gravity [37].

The first ever nuclear reactor (built in 1942), the *Fermi Pile 1* or *Chicago Pile 1* (CP1), had two basic safety systems in place. First system was a gravity driven cadmium absorber rods held by a rope, while the second system was a solution of cadmium sulphate placed in buckets above the reactor pile [38].

Established technological work relevant to the thesis with regards to chosen method, data and numerical calculation tools is presented here.

4.1 Literature Review

Blandford *et al.* [39], [40], [41] describe an innovative buoyantly driven shutdown rod concept for a *Pebble Bed Advanced High Temperature Reactor* (PB-AHTR) that employs fluoride salt as the coolant. The shutdown rods are initially extracted above the core and when the coolant temperature increases due to an event, the rods are inserted on account of change in buoyancy. The insertion velocity is maximised by adopting a cylindrical profile that has the minimum surface to volume ratio. They performed experimental evaluation of numerical calculations, showing that dynamic response of the rod insertion for *loss of heat sink* (LOHS) accident provides good reactivity response. One of the conclusions they draw is that since the concept relies on changes in buoyancy, which due to molten fluoride salt yields small changes in density, the drag coefficient needs to be experimentally validated and minimised.

Lin *et al.* [42] presented numerical and experimental dynamic analysis for a control rod drop in *Thorium Molten Salt Reactor* (TMSR). The work provides displacement, velocity and acceleration profiles of the control rods driven by a motor, as a function of time spent during insertion. The study infers that hydrodynamic drag is the main contributor to resistance to faster and more effective insertion. In the molten fluoride coolant the control rods attain a maximum speed of $1.48m/s$, covering a total distance of $1.42m$ in $2.02s$ well under objective goal of limiting it to under $6s$. This paper provides insight into the time scales one can expect from a gravity assisted rod drop.

Babu *et al.* [43] made mathematical modelling and experimental study for the safety rod scram action in a sodium cooled reactor. Their work showed that there is good agreement between simple 1D modelling and full-fledged *computational fluid dynamic* (CFD) calculations. The authors also conclude that scram action is more influenced by hydraulic forces than frictional forces, and more importantly theoretical calculations matches well with experimental results thus validating the theoretical predictions.

Donis *et al.* [44] presented the details of a mathematical model for the control

rod drop in a pressurised water reactor and its experimental verification. This study gives a comprehensive set of equations that define the forces acting on the control rod. The authors consider shear forces contribution to be independent of flow velocity and is simply added to mechanical drag. This work also infers that a number of parameters relating to the geometry of system affect mathematical model and the final results. The study also shows good agreement between calculated insertion time and operational insertion time.

Taliyan *et al.* [45] describe the theoretical modelling and the studies carried out to predict the drop characteristics of shutdown rod and its experimental verification in PHWR. The equation of motion for the shutdown rods was formed by developing force balance, arising from various interactions in the channel. One observation made by the authors is that using simplified friction factor for flow in pipes yielded different results from the experiment results, and a correction factor was suggested.

Andriambololona *et al.* [46] describe methodology for numerical simulation of rod cluster control assembly in a PWR. The authors showed relevance of friction factor of guide tubes on the insertion characteristics. The study also proposes modification to the 3D numerical analysis by improving the mesh near contact surfaces of the rod with coolant fluid.

Rabiee and Atf [47] presented control rod drop analysis using averaged Navier-Stokes equation model in SIMPLE algorithm of FLUENT, the commercial CFD package of ANSYS, and implementing a layered dynamic mesh around the control rods. The authors also conducted a sensitivity analysis of the leakage flow in the channel and concluded that increased leakage from the control rod channel resulted in faster insertion times.

From the above studies it is evident that rigorous calculations and experimental validation have been made with regards to control rod drop action. The drop action however is also influenced by core configuration, safety rod design and coolant properties. The control rod insertion is therefore specific to the reactor. While a majority of the previous studies focus on LWRs only a small portion of it focuses on LMFR especially in LFRs. This necessitates numerical modelling and optimisation of the performance in each reactor design. The following section presents the various computational tools used in this thesis.

4.2 Computational Tools

To achieve the intended objectives of the thesis, a number of tools were used. These software were chosen to be reliable, state of the art tools that have proper validation for the intended use by various benchmarks. The following products were used during the course of the thesis.

- MATLAB/SIMULINK - Powerful products of MathWorks, MATLAB is a numerical computing environment that enables programming and visualisation while SIMULINK is a visual programming environment for modeling, simulating and analyzing dynamic systems [48]. MATLAB was used extensively for numerical calculations in thermal hydraulic analysis, shutdown rod insertion analysis, general purpose plotting of graphs and curve fitting using the built-in Curve Fitting Tool. The BELLA multi-point dynamics code is modelled in SIMULINK [10] which is used for transient analysis.

- OpenMC - OpenMC is a Monte Carlo particle transport simulation code for on neutron criticality calculations developed originally at Massachusetts Institute of Technology from 2011. It is capable of simulating 3D models based on constructive solid geometry with second order surfaces. OpenMC supports either continuous energy or multi-group transport [49]. The continuous-energy particle interaction data is based on a native HDF5 format that can be generated from ACE files used by the MCNP and Serpent Monte Carlo codes. OpenMC was extensively used in static neutronic characterisation of the core and in determination of reactivity coefficients by perturbation method. OpenMC was also used in determining the reactivity worth of the shutdown rods.
- Serpent - Serpent is a Monte Carlo reactor physics burnup calculation code developed at VTT Technical Research Center from 2004. The current version 2 of the code is used in traditional reactor physics applications, multi-physics simulations, coupled thermal hydraulic and coupled CFD simulations, neutron and photon transport simulations in dosimetry [50]. In the current study Serpent was used in burnup calculations of the fuel, to determine reactivity swing and fuel evolution with burnup, as OpenMC currently does not have the ability to perform burnup calculations. The JEFF-3.1.1 nuclear data evaluated library was used in both the Monte Carlo codes.
- FLUENT - ANSYS workspace is applied for simulating finite element models of structures, fluids, electromagnetics, electronics systems and mechanical components. FLUENT is CFD tool within the ANSYS workspace that has broad physical modelling capabilities to model flow, turbulence, heat transfer and reactions for industrial applications [51]. FLUENT was used in the thesis to determine primarily the drag coefficients of the shutdown assembly profile.

The method and approach followed during the thesis is described in this chapter. In compliance to the objectives of the thesis a simple sub channel analysis is performed to assess the steady state characteristics of the core, followed by the modelling of the hot state geometry of the core. Afterwards the static neutronic characterisation of the core is performed.

5.1 1D Thermal Hydraulics Model

The primary heat exchange between the fuel rod and the coolant is described by a simplified 1D model. The fuel rod is cylindrical with the nitride pellet enclosed within the clad. Figure 5.1 shows the cross section of the axially discretised model.

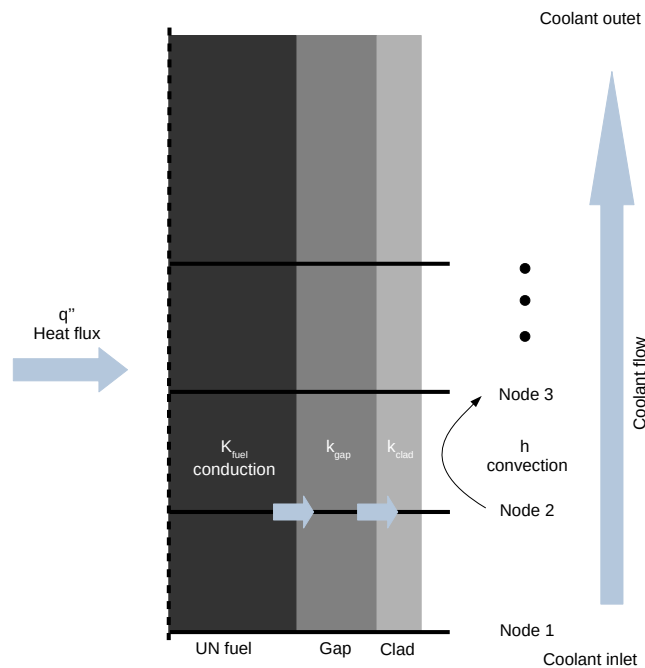


Figure 5.1: Heat transfer from fuel to the coolant

The considered heat transfer mechanisms are:

- Heat generation and conduction across the fuel pellet.
- Heat conduction across the gas gap. While the gas being a fluid also partakes in convection, this contribution to heat transfer is neglected.
- Heat conduction across the clad.
- Heat transfer by convection to the coolant.

Fuel assembly sub-channel is discretised axially into elements as shown in the figure. The thermal hydraulics (T/H) calculations are performed iteratively at each node, by developing a MATLAB script, according to the flowchart shown in Figure 5.2.

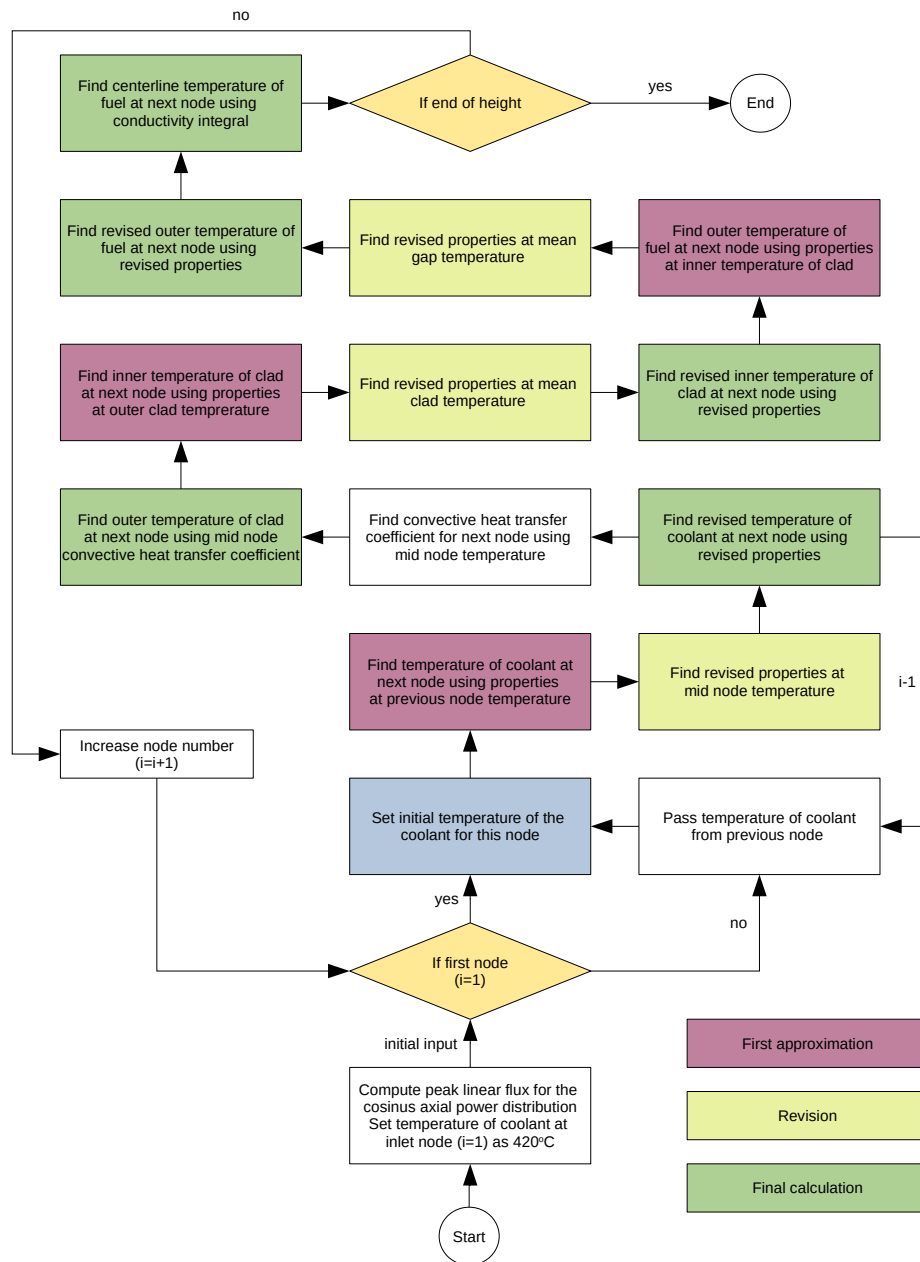


Figure 5.2: Calculation scheme for the 1D T/H sub channel analysis

The heat generation in the fuel pellet is non uniform in a cylindrical reactor. The axial power distribution follows a consinus profile [52] as defined in Equation 5.1.

$$q''(z) = q''_o \cos\left(\frac{\pi z}{\tilde{H}}\right) \quad (5.1)$$

q''_o is the peak heat flux (W/m^2) in the fuel pin given by Equation 5.2, \tilde{H} is the extrapolated height for the cosinus power distribution and z is the position along the height H .

$$q''_o = \frac{q''_{av} \pi H}{2\tilde{H} \sin\left(\frac{\pi H}{2\tilde{H}}\right)} \quad (5.2)$$

q''_{av} is the average heat flux (W/m^2) in the fuel pin given by Equation 5.3.

$$q''_{av} = \frac{q'_{av}}{\pi d_{Co}} \quad (5.3)$$

q'_{av} is the average linear power (W/m) in the fuel pin given by Equation 5.4 and d_{Co} is the outer diameter of the clad.

$$q'_{av} = \frac{P}{HN_{rods}} \quad (5.4)$$

P is the steady state thermal power generation, N_{rods} is the total number of fuel pins in the reactor. For the cosinus power heating of the bulk temperature of the coolant at a position z along the height is given by Equation 5.5.

$$T_{lb}(z) = T_{lbi} + \frac{q''_o P}{G c_{p_{pb}}} \frac{\tilde{H}}{\pi} \left[\sin\left(\frac{\pi z}{\tilde{H}} + \frac{\pi H}{2\tilde{H}}\right) \right] \quad (5.5)$$

T_{lbi} is the coolant temperature (K) at the inlet, G is the steady state mass flow rate (kg/s). $c_{p_{pb}}$ is the specific heat capacity of the coolant. The outer clad temperature is computed by convective heat balance to the coolant given by Equation 5.6.

$$T_{Co}(z) = T_{lb}(z) + \frac{q''(z)}{h} \quad (5.6)$$

h is the convective heat transfer coefficient¹ ($W/m^2/K$). The inner clad temperature is computed by conductive heat balance across the clad given by Equation 5.7.

$$T_{Ci}(z) = T_{Co}(z) + \frac{q''(z) d_{Co}}{2k_{clad}} \log\left(\frac{d_{Co}}{d_{Ci}}\right) \quad (5.7)$$

k_{clad} is the thermal conductivity ($W/m/K$) of the steel clad, d_{Ci} is the inner diameter of the clad. The surface fuel temperature is computed by cylindrical conductive heat balance across the gas gap given by Equation 5.8.

$$T_{Fo}(z) = T_{Ci}(z) + \frac{q''(z) d_{Co}}{2k_{gap}} \log\left(\frac{d_{Ci}}{d_{Fo}}\right). \quad (5.8)$$

k_{gap} is the thermal conductivity ($W/m/K$) of the gas gap, d_{Fo} is the outer diameter of the fuel pellet. The centerline fuel temperature is computed by the thermal conductivity integral given by Equation 5.9.

¹See Appendix A for details of convective heat transfer coefficient calculation

$$q' = 4\pi \int_{T_{Fo}}^{T_{Fi}} k_{fuel} dT \quad (5.9)$$

q' is the linear power (W/m) and k_{fuel} is the thermal conductivity² ($W/m/K$) of the nitride fuel. The height in the core corresponding to this region, where power is being generated, is termed *active zone* (AZ). The temperature profiles predicted for the coolant, clad and the fuel pellet of height $H = h_{fuel}$ are shown in Figure 5.3. The figure also shows the cosinus linear power distribution for extrapolated height \tilde{H} . While the fuel pellet temperatures is predicted to follow cosinus profile, the peak is shifted upwards along the coolant flow.

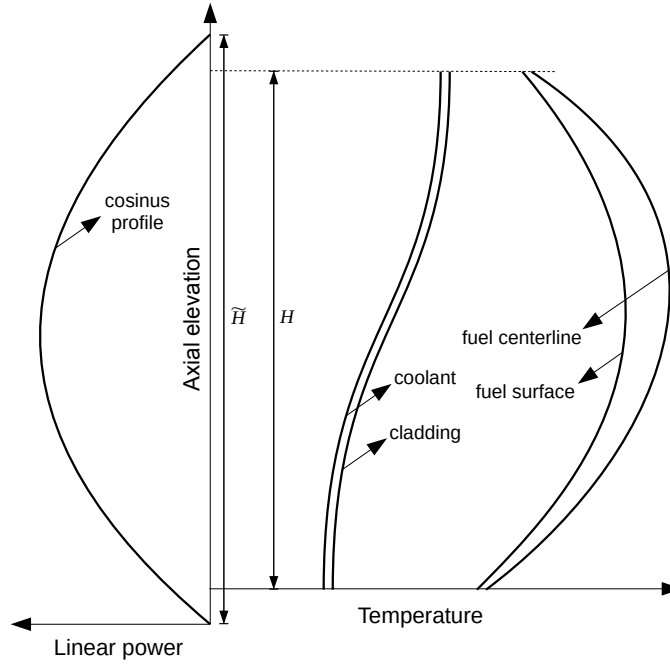


Figure 5.3: Predicted temperature profiles at steady state [Representative image [52]]

The properties of fluid, namely thermal conductivity (k_{pb}), specific heat capacity ($c_{p_{pb}}$), dynamic viscosity (μ_{pb}), density (ρ_{pb}) and thermal conductivity's of the fuel (k_{fuel}) and steel clad (k_{clad}) are functions of temperature³ and are used correspondingly during revision of properties at each step. It is to be noted that the thermal conductivity of the gas gap is not considered a function of temperature, and instead a constant thermal resistance (K/W) is considered in its place. To have an accurate representation of the system this thermal hydraulics model resolves second order effects, in a form of semi implicit linear interpolation method, as shown in the flowchart. The model however has its limitations. Heat transfer by radiation and frictional pressure loss along the channel are not not accounted for, implying a constant mass flow rate of the coolant throughout. Axial conduction in coolant is not considered, assumed to be small compared to convective heat transfer. Table 5.1 gives the relevant parameters required by the code.

²See Appendix A for details of the correlation

³See Appendix A for details of the correlations

Table 5.1: Parameters for T/H evaluation

Parameter	Value	Units
Fuel Element Height	130.50	cm
Extrapolated Height	168.28	cm
Fuel Diameter	0.812	cm
Clad Inner Diameter	0.856	cm
Clad Outer Diameter	0.960	cm
Fuel Rod Pitch	1.130	cm
Assembly Coolant Flow Rate	87	kg/s
Number of Assemblies/Rods	85/271	

The extrapolated height was determined by a dry run of a Monte Carlo code to determine axial power profile which used to find the preliminary axial peaking factor, at 1.298. The calculated preliminary temperature profiles as calculated from the MATLAB script are presented in Figure 5.4 and the preliminary results are summarised as follows.

Temperature	Mean	Max	Units
Coolant	485	550	C
Cladding Outer Surface	491	554	C
Cladding Inner Surface	495	555	C
Fuel Surface	646	705	C
Fuel Centerline	667	730	C
Average Cladding	493		C
Average Fuel	656		C

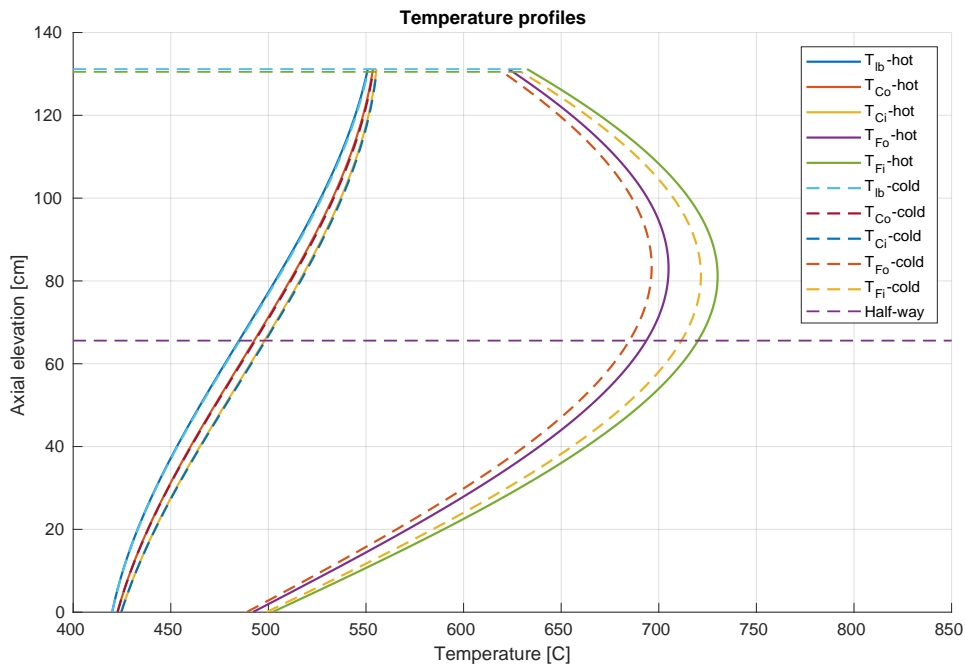
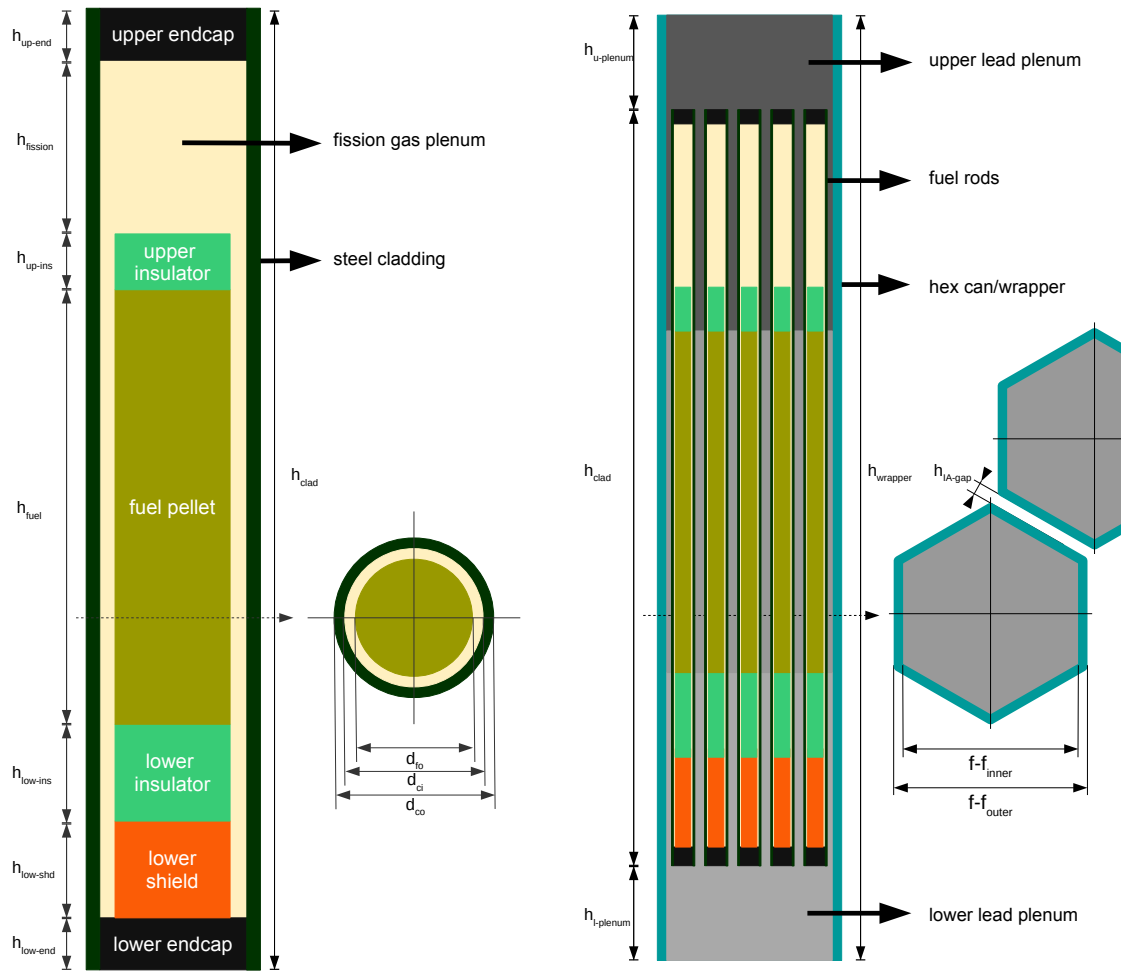


Figure 5.4: Temperature profiles at steady state

The profile for coolant and the clad are as predicted. The fuel temperature also follows the prediction, with the peak occurring at a height 15.5cm above the midplane. This shift upwards is attributed to the coolant flow which carries the heat upwards along the flow. Though the results might not very accurate, due to inherent drawbacks, it provides a first order approximation of the temperature fields in the fuel rod components.

5.2 Hot Core Geometry Model

During operation, the core constantly generates power as heat which is eventually transferred to the coolant, as was modelled in the previous section. The individual components of the core, the fuel pellet, the insulator pellets, shield pellets, end caps of the fuel rod, steel clad of the fuel rod and the hex can wrapper are at their steady state temperatures due to constant heat generation and removal, representative images of the fuel rod and the wrapper are shown in Figure 5.5a and 5.5b. Core startup from cold state to hot full power state results in thermal expansions of these components. In this section the expansions for these components are computed.



(a) Fuel rod

(b) Assembly wrapper

Figure 5.5: Representative graphics of fuel rod and assembly wrapper

The thermal expansion in the fuel rod between two temperatures can be expressed as shown in Equation 5.10.

$$\delta L = L_{cold} \int_{T_{cold}}^{T_{hot}} \alpha_{material} dT \quad (5.10)$$

$\alpha_{material}$ is the thermal expansion coefficient (*coefficient of thermal expansion* CTE) ($1/K$) of the material, which is a function of temperature, and thus the integral. The same equation is used to calculate the axial expansion, by replacing L_{cold} with h_{fuel} , the cold height of the fuel, and the radial expansion, by replacing L_{cold} with d_{cold} , the cold outer diameter of the fuel. The change in dimensions entail change in volume and hence the density, while conserving the mass of material as shown in Equation 5.11. The cold temperature of the fuel is $20^\circ C$ while the hot temperature considered for the fuel pellet is the mean centerline temperature, calculated from the cosine temperature profile.

$$\rho_{cold} V_{cold} = m = \rho_{hot} V_{hot} \quad (5.11)$$

V_{cold} and V_{hot} are the cold and hot volumes (m^3) of the material respectively, ρ_{cold} and ρ_{hot} are the cold and hot densities (kg/m^3) of the material respectively and m is the mass (kg) of the material. Table 5.2 provides the CTE for the different materials in the core, that is used in this study for determining the hot core geometry.

Material	Notation	Material	Notation
Fuel Pellet (UN)	α_{UN}	Fuel Clad ($1515Ti$)	ζ_{1515Ti}
Insulator (ZRN)	α_{ZRN}	Shield & CR Pellet (B_4C)	α_{B_4C}
SD Pellet ($WReB_2$)	α_{WReB_2}	SD Clad & Wrapper ($FeCrAl$)	α_{FeCrAl}
RF Pellet (YSZ)	α_{YSZ}		

Table 5.2: Coefficient of thermal expansion correlations

Notation	Correlation [1/K]	Range [K]
α_{UN}	$7.096 * 10^{-6} + 1.409 * 10^{-9}T$ [53]	298-2523
ζ_{1515Ti}	$-3.101 * 10^{-4} + 1.545 * 10^{-5}T(^{\circ}C) + 2.75 * 10^{-9}T(^{\circ}C)^2$ [54]	293-1273
α_{ZRN}	$6.572 * 10^{-6} + 1.825 * 10^{-9}T - 1.203 * 10^{-1}T^{-2}$ [55]	293-2400
α_{B_4C}	$3.78 * 10^{-6} + 1.657 * 10^{-9}T + 1.726 * 10^{-13}T^2$ [56]	-
α_{WReB_2}	$4.1 * 10^{-6}$ [57]	@ 100
α_{FeCrAl}	$10.3 + 4.694 * 10^{-3}T - 21.36 * 10^{-7}T^2 + 1.074 * 10^{-9}T^3$ [58]	300-1500
α_{YSZ}	$1.05 * 10^{-5}$ [59]	298-1273

The CTE for fuel steel clad from the available literature was found to be a function of strain parameter (ζ). The CTE for shutdown absorber is assumed to be a constant in our study, mainly because the thermal expansion of the shutdown assembly and control assembly are neglected, as they affect very little to the neutronics.

Axial expansion of control drive lines will, in reality, affect the reactivity that will be handled by the control systems, by extracting the rods. Radial expansion of the control rods and shutdown elements are assumed to not effect neutronics. Further, the shutdown assembly is, during normal operation, parked above the core.

Using Equation 5.10, the expansions in height and diameter of the insulators, shield, end caps are determined. The cold temperature considered is $20^{\circ}C$ while the hot temperature considered for the sub-components below the fuel pellet is the coolant inlet temperature and above the fuel pellet is the coolant outlet temperature. It can be argued that Equation 5.10 assumes a linear heating from T_{cold} to T_{hot} uniformly throughout the material. But this is not the case, especially in fuel pellet and clad, where the temperature has a profile with non uniform heating. The middle regions have high temperature and thus expand more than the peripheral regions. The developed code, from previous section, has a weakly implemented coupling with thermal mechanics where for each discretised element the expansion is also computed starting from cold dimensions, so that it accounts for differential temperatures. Such calculations are repeated, where after one run the total height of the fuel pellet is computed by adding the expanded heights of the discretised elements, and the calculation is run again using the new height. This accounts for second order effects. The iterations are repeated for a few times until the calculations converge, when the difference extended height and previous height is within 0.1%.

Figure 5.4 shows this effect. The cold run temperature profiles are calculated with a initial cold geometry. For the second run the dimensions are expanded and the calculations are run again. The final profile that has deviation of less than 0.1% is presented as hot run profile. It was, however, realised that by taking the mean temperature and integrating to compute the new dimension, the margin of error is very negligible, and for other smaller dimensions such as diameters of the pellets and clad and also heights of the fuel rod components, the second order effects are very negligible and thus we proceed with using Equation 5.10 with mean steady state temperatures.

The clad is assumed to be differentially expanded by considering mean clad temperature in the AZ as computed from the previous section and below and above the AZ is assumed to be the coolant inlet and outlet temperatures. Similarly the wrapper is expanded, both axially and radially. The inner and outer *face to face* dimension expansion results in the reduction of inter assembly gap, the *diagrid* is extended to coolant inlet temperature which compensates inter assembly gap reduction, ultimately increasing the assembly pitch. The axial expansion of the wrapper in the fuel rod region is expanded corresponding to the clad expansion, while the *lower plenum* and *upper plenum* regions are expanded to inlet and outlet temperatures respectively. Table 5.3 gives the thermal expansion calculated for the more important components as percentage.

These expansion results in decrease in material density which are necessarily computed to conserve isotopic composition of the elements in the core. With the hot core geometry and material density results the core static neutronics can be characterised as explained in the next section.

Table 5.3: Thermal expansion in materials expressed as percentages

Material	Temperature [C]	Expansion [%]	Density [g/cm^3]
			Cold/Hot
<i>UN</i>	656	0.506	12.901/12.707
<i>1515Ti</i>	493	0.798	8.129/8.079
<i>ZRN</i>	420/550	0.275/0.376	6.498/6.445/6.425
<i>B₄C</i>	420	0.166	2.250/2.239
<i>FeCrAl</i>	420/493/550	0.478/0.571/0.645	7.170/7.023/7.051/7.012

5.3 Neutronics Model

Reactors are conventionally categorised as burner, iso-breeder or breeder according to the *conversion ratio* (CR) of the reactor configuration. LWRs fall into the category of burners, where the initial fissile fuel is continuously fissioned thereby forming fission products. These reactors operating in thermal spectrum are net consumers of fissile materials, producing minor quantities of new fissile material and are characterised by $CR < 1$. The reactivity of such systems decrease over time, which is compensated by the extraction of control rod assembly. The iso-breeder reactors are a class of reactors, characterised by unity CR, that is they produce the same amount of fissile material as they consume during burnup. Breeder reactors, as the name suggests, produce or breed more fissile material than they consume and are characterised by $CR > 1$. A reactor might also be a mixed breeder-burner type, where in the first part of its cycle fuel is bred and in the latter part fuel is burnt. Typically the reactivity evolution of such systems with burnup, follow approximately a parabolic profile, shown in Figure 5.6.

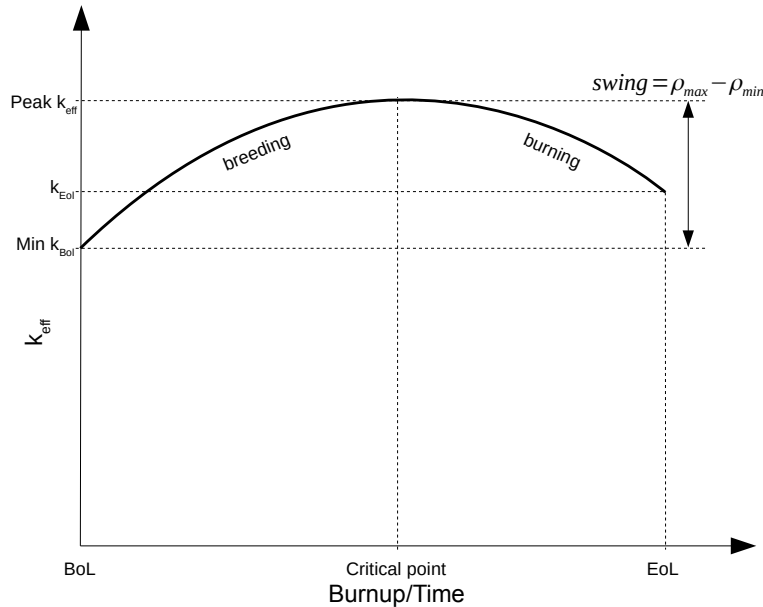


Figure 5.6: Parabolic excess reactivity profile

The reactivity swing during the operational cycle (or operational life, if reactor is not refuelled) is the difference between the maximum and the minimum reactivity in the cycle (or life). Control rods compensate for the reactivity excess by being

inserted into the core and for reactivity deficit by being extracted from the core. The uncontrolled reactivity is highest at the maxima of the parabola, and in order to maintain criticality control rods are inserted the furthest. An inadvertent extraction of control rods when the potential reactivity of the core is the highest would be a dangerous overpower transient. It is the objective of some modern reactors to reduce the reactivity swing to reduce the worth of the control rods necessary to prevent such overpower transient [60].

In the current work, the reactivity evolution is determined for the operational life of the reactor as a function of burnup and subsequently a critical point, where the potentiality is the maximum is determined. The Monte Carlo code OpenMC and the more popular code Serpent were used for the characterisation.

Having determined the dimensions of the core at full power steady state the core geometry is modelled in the OpenMC and Serpent Monte Carlo codes. OpenMC has several approaches to perform *eigenvalue* calculations. One of the more effective way is to separately define `xml` files for materials, geometry and calculations settings as `materials.xml`, `geometry.xml` and `settings.xml`. OpenMC supports Python API using which these input files are exported.

- `materials.xml` - Describes the materials in the core, with concentration of nuclides and the density of the materials
- `geometry.xml` - Constructive solid geometry can model complex geometry of the core. It defines all the surfaces and regions/cells formed by intersecting surfaces.
- `settings.xml` - The execution settings, to instruct OpenMC how to calculate, is specified. Currently, OpenMC supports a limited number of execution settings, fixed source or eigenvalue.
- `tallies.xml` - In order to get useful data from the calculation tallies file is optionally used. It is similar to the detector card used in other popular Monte Carlo codes. Tallies file specifies the filters or region where the tallies or score need to be calculated. It is to be pointed out here that OpenMC results are normalised to source particle, and requires to be multiplied with normalising factor to obtain exact value. For example the kappa-fission score calculates the recoverable fission energy production rate in the units of $eV/source$. The normalisation factor in such cases is determined as shown in Equation 5.12.

$$f_{norm}[source/s] = \frac{P\nu}{Qk} \left[\frac{[J/s][neutron/fission]}{[J/fission][neutron/source]} \right] \quad (5.12)$$

P is the power in J/s , Q is the energy per fission event in $J/fission$, ν is the neutron production rate in $neutron/fission$ and k is the neutron multiplication factor in $neutron/source$. Multiplying the tallies score with the normalisation factor will give absolute value of the tally, in this case eV/s . Other codes do this automatically in the output, however OpenMC does not. This is useful for generating power distribution profiles.

- `plots.xml` - To create slice and 3D plots, this file is additionally created, to easily visualise and validate the model.

Figure 5.7 shows the universe map modelled in OpenMC. Axially the core is divided into regions. Each region has lattice of assemblies. Each of these assemblies is itself a lattice of rods (fuel rods, control rods, shutdown rods, reflector rods) or simply empty hex can filled with lead. What is also modelled is portions of the cold leg and hot leg. Figure 5.8 shows the axial and radial slices of the fuel assembly. The regions LOW and LOW-MID are filled with lead at inlet temperature, the regions MID and MID-U are filled with lead at mean temperature and regions MID-UP and UP are filled lead at outlet temperature.

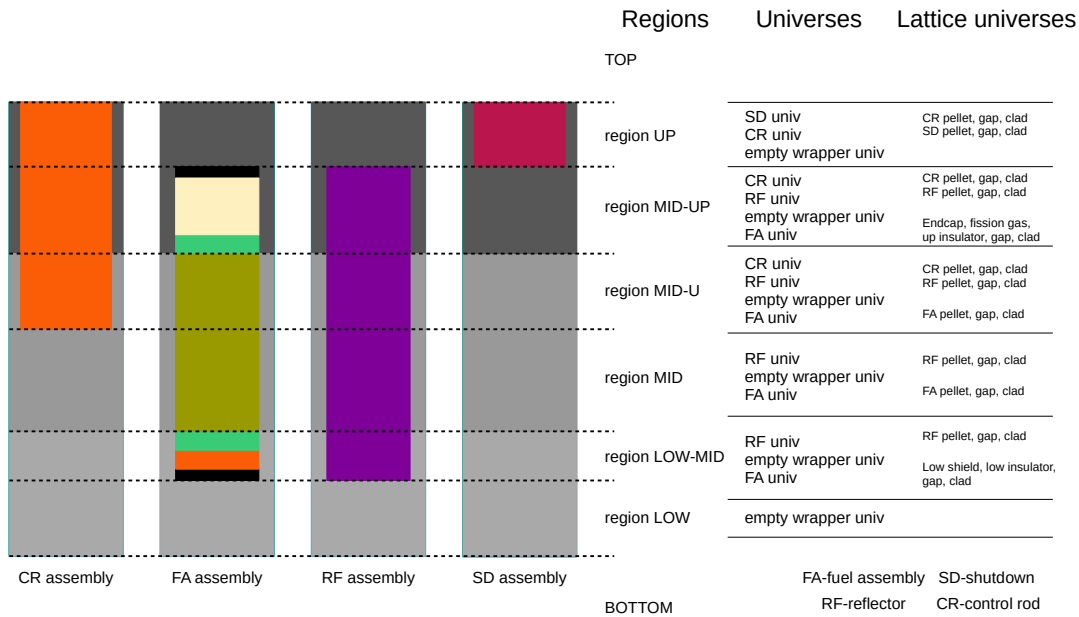


Figure 5.7: Core assembly multi-universe mapping

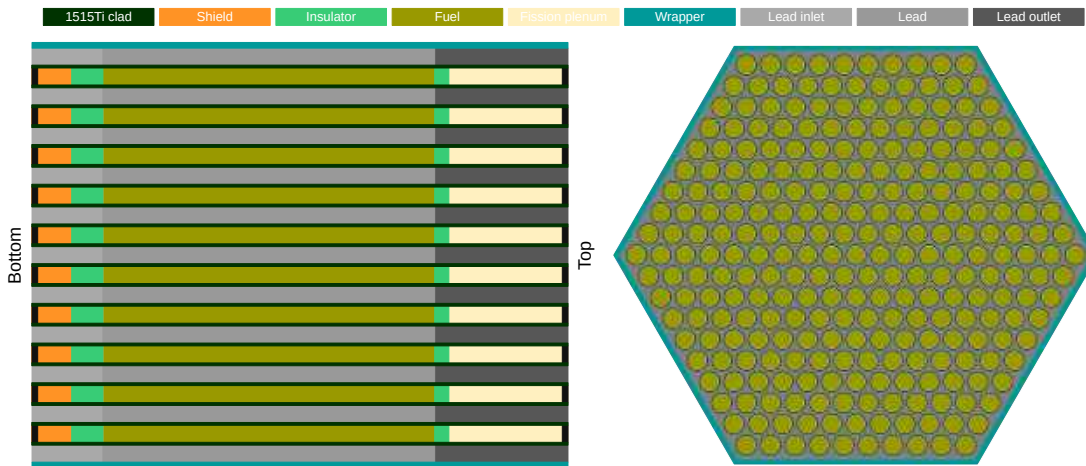


Figure 5.8: Axial slice (left) and radial slice (right) of the SEALER-UK FA assembly

Figure 5.9 shows the radial slice of the control assembly, shutdown assembly and the reflector assembly and Figure 5.10 and 5.11 shows the plots of axial slice of the core for both shutdown and control assemblies fully inserted. Figure 5.12 shows the radial slice of the core as modelled in OpenMC.

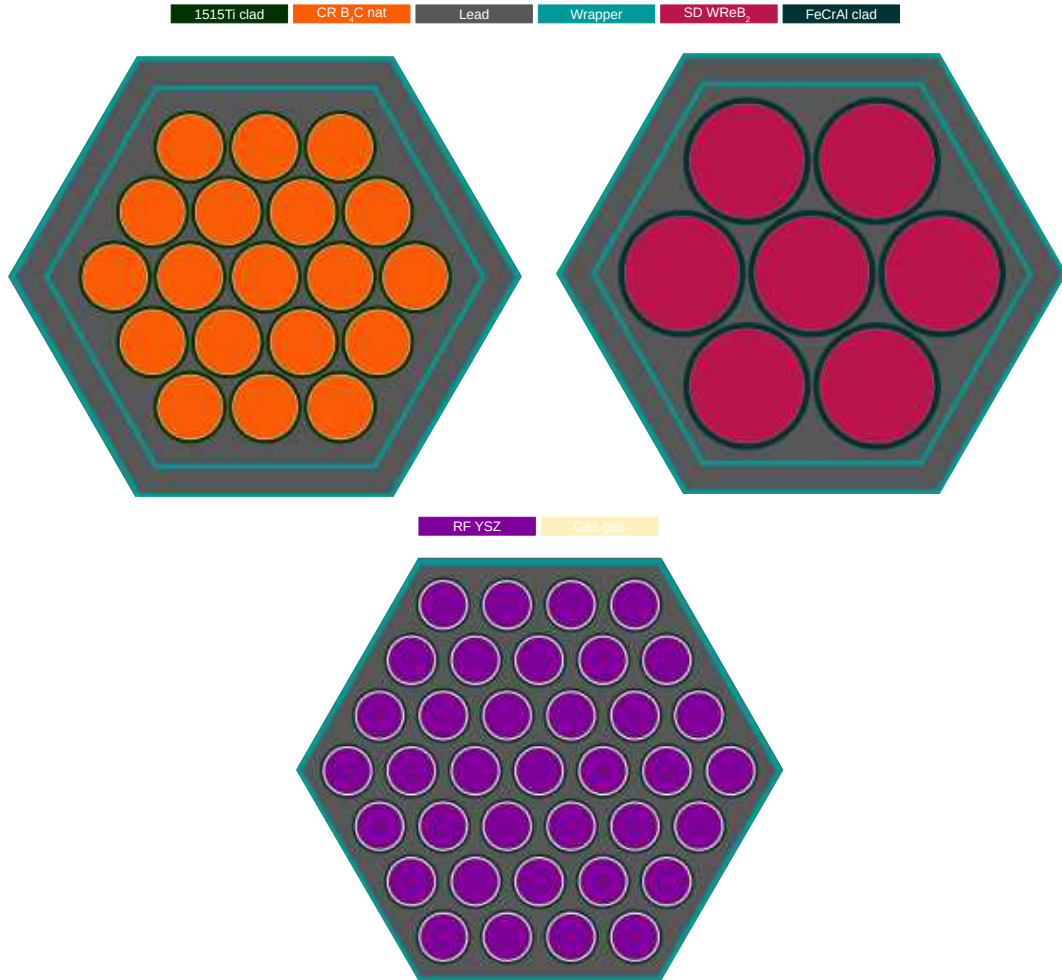


Figure 5.9: Radial slice of the SEALER-UK CR assembly (top left), SD assembly (top right) and RF assembly (bottom)

While OpenMC is a capable tool for eigenvalue calculations, it unfortunately has some rather important shortcomings. One, it has currently no support for burnup calculations. Two, it is unable to provide kinetic parameters, such as prompt neutron reproduction time (Λ_{eff}), effective delayed fractions (β_{eff}) and their decay constants (λ) which are solved using adjoint weighted calculations. To overcome these shortcomings, the other Monte Carlo code Serpent is used which can effectively calculate adjoint weighted point kinetics parameters [61]. For this reason, the same geometry is modelled in Serpent and burnup calculation is run to determine the isotopic composition of the fuel throughout the operational life.

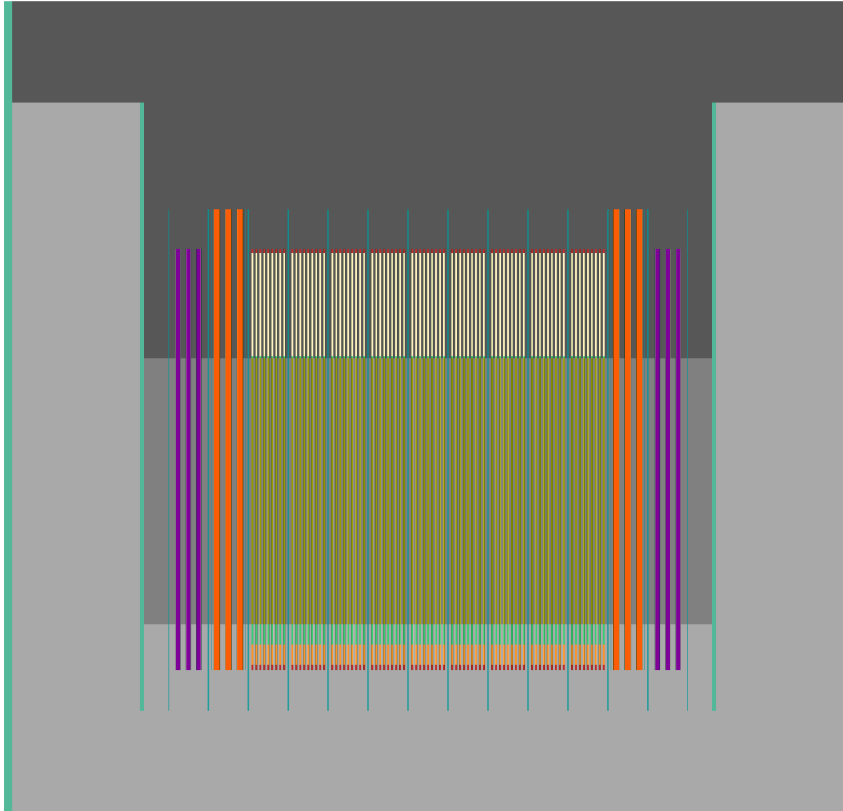


Figure 5.10: Axial slice of the core in YZ plane as modelled in OpenMC

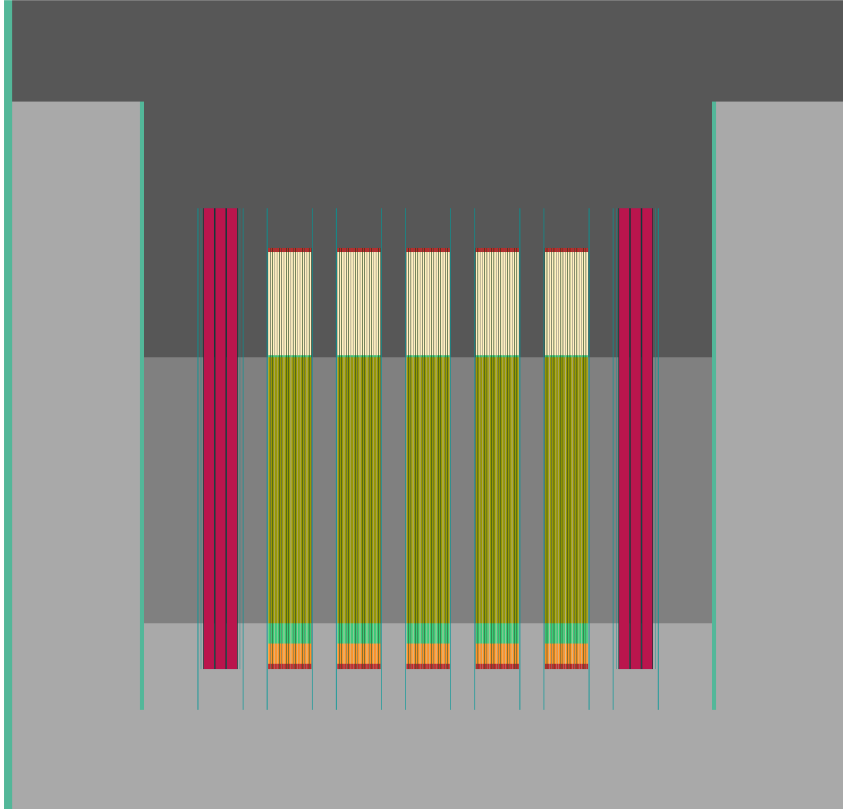


Figure 5.11: Axial slice of the core in XZ plane as modelled in OpenMC

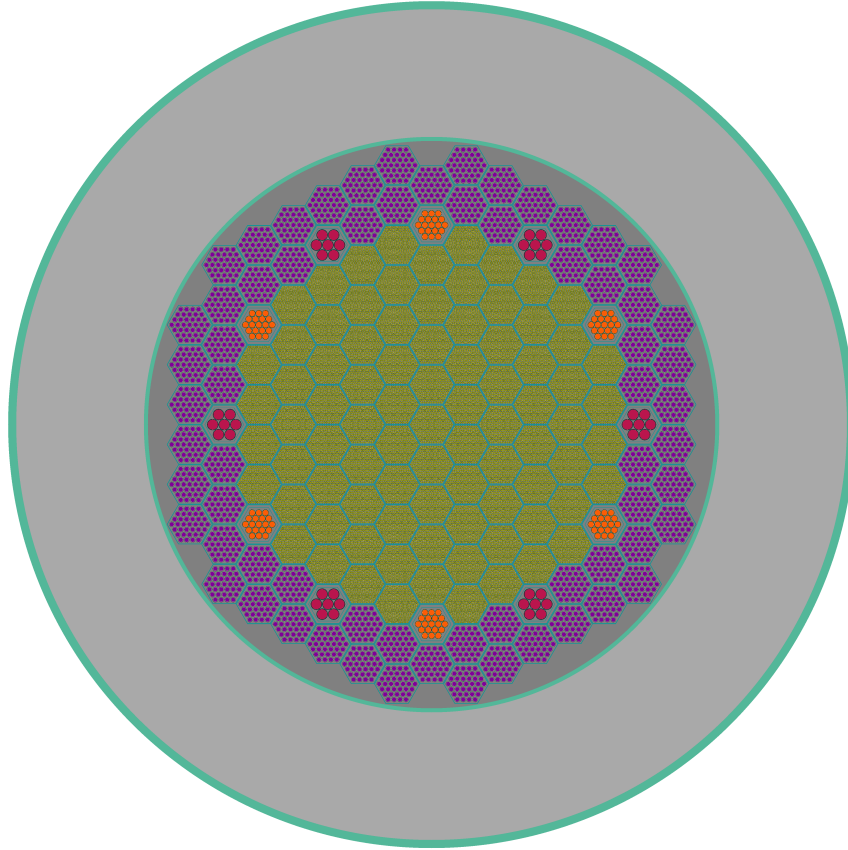


Figure 5.12: Radial slice of the SEALER-UK core showing the fuel assemblies, CR assemblies, SD assemblies and RF assemblies

Serpent has two methods of burnup calculations to solve for the *Bateman equations*. The *Transmutation Trajectory Analysis* (TTA) and the *Chebyshev Rational Approximation Method* (CRAM). The first method is based on analytical solution of linearised transmutation chains and the latter is an advanced matrix exponential solution [62], implemented by default. The default method is suggested for more accurate estimation of composition of the fuel for each burnup step, and this is used for the calculation together with the constant extrapolation with *linear interpolation predictor corrector* algorithm which determines flux and cross section at the end of step assuming a constant flux and cross section at start of each step, and repeats the calculation with the mean of the two values. While this repetition step increases the time for simulation it accounts for more accurate isotopic change. Serpent 2 supports even higher order algorithms depending on users preference.

SEALER-UK is designed to operate for 25 years or 22.5 equivalent full power years. The 18.6tons of 11.8% enriched *UN* fuel is burnt in the core for 22.5 years at a power density of 73W/g, for the following steps from *beginning of life* (BoL) to *end of life* (EoL).

	BoL								EoL
Time [years]	0	2.5	5	7.5	10	11.25	12.5	17.5	22.5
Time step [days]		912	913	912	913	456	456	1825	1825

The steps were chosen so as to have a better resolution of reactivity at the *middle of life* (MoL) where the reactivity is expected to reach a maxima, seen in Figure 5.6. It is to be pointed her that the burnup calculation is performed with both control assembly and shutdown assembly extracted and in parking position above the core. The eigenvalue k_{eff} for the hot state core at BoL is found to be as follows.

BoL k_{eff}	OpenMC
Both CR/SD extracted	1.00708 ± 0.00012
Only CR inserted	0.99705 ± 0.00012
Only SD inserted	0.99681 ± 0.00014
Both CR/SD inserted	0.98986 ± 0.00015

5.3.1 Results

5.3.1.1 Burnup

The evolution of k_{eff} as computed by Serpent is shown in Figure 5.13 [63].

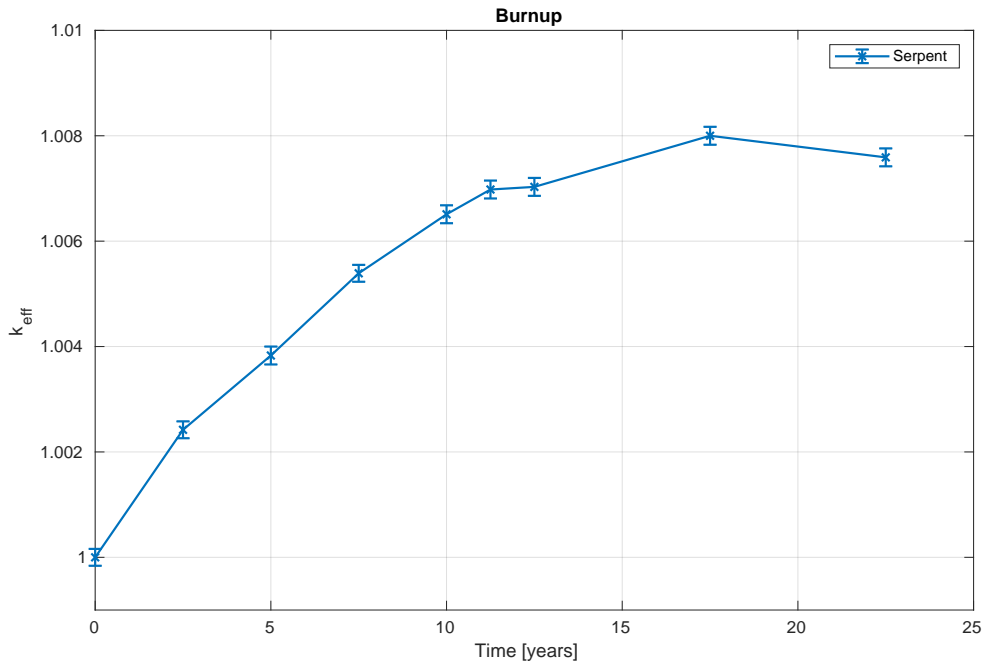


Figure 5.13: k_{eff} evolution as a function time

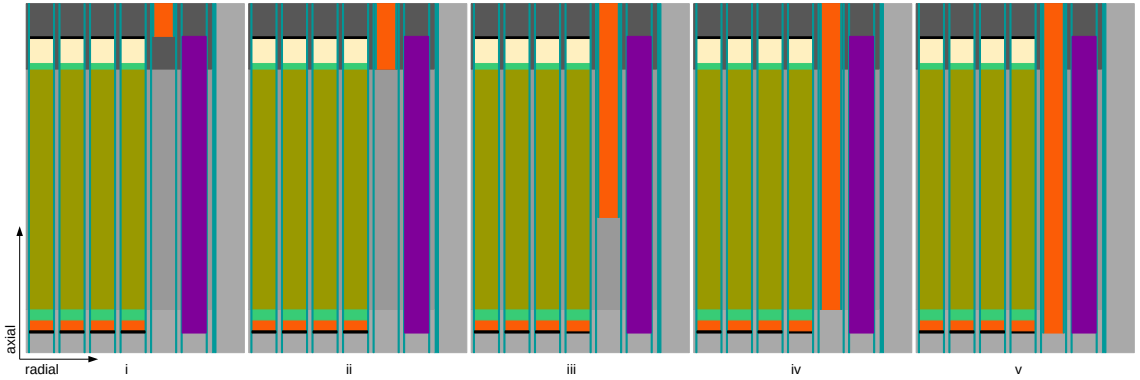
The burnup has, as expected, a parabolic profile. The maximum uncontrolled reactivity is attained at 17.5 years. The burnup at the EoL reaches $60.68 MWd/tU$. The results have a minor limitation that the changes in fuel density due to swelling is not attributed during burnup [14]. With burnup, volatile fission products are produced. The fuel pellet due to accumulation of these gases swells, thereby reducing the density. This reduction in density will cause reduction in k_{eff} . The relation between burnup and the volume change in fuel is given in Equation 5.13.

$$\frac{\Delta V}{V}(\%) = 4.7 * 10^{-11} T_{fuel-mean}^{3.12} Bu^{0.83} \rho_{UN}^{0.5} \quad (5.13)$$

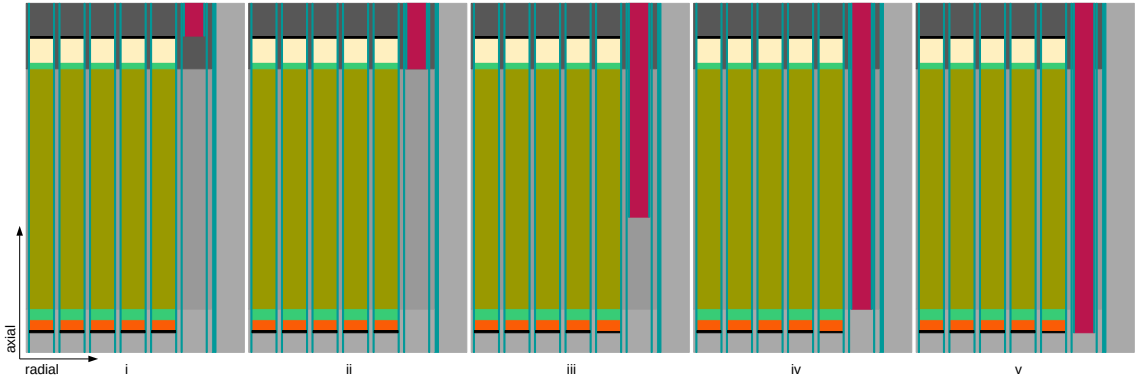
$T_{fuel-mean}$ is the mean fuel temperature (K), Bu is the fuel burnup ($at\%$) and ρ_{UN} is the porous density of fuel pellet. A more appropriate burnup calculation would account for this swelling, consequently lowering the parabolic profile. The peak would however not vary appreciably in time. Therefore in the current work 17.5 years is considered to be the *critical point* for further analysis. The fuel vector is obtained from the Serpent burnup calculation, that had predefined material inventory card. The original input files are then revised with this fuel isotopic composition, that earlier had 11.8% U^{235} mononitride.

5.3.1.2 Control Bank and Shutdown Bank Reactivity Worth

Following the burnup calculation the characterisation of the control assemblies and shutdown assemblies is performed. This is done by perturbing the height of control rods and shutdown rods inserted into the core as shown in Figure 5.14a and 5.14b



(a) Axial positions of CR bank in the core



(b) Axial positions of SD bank in the core

Figure 5.14: Representative graphics for position of CR and SD assemblies

The CR/SD worth is computed by positioning the assembly just above and below AZ, shown in 5.14a (ii) and (iv). Additionally, the CR/SD were extended between fuel rod endcaps, 5.14a (i) and (v), to see if that had any effect of increasing the worth. Simulations are run at the critical point for the four cases, the results are shown in Table 5.4. It is worth knowing that the effective multiplication factor k_{eff} , provided by the Monte Carlo codes is converted to reactivity with units of *percent mille* (pcm) using Equation 3.1.

OpenMC, with this setup, requires approximately 300 minutes of wall time to run while Serpent requires approximately 90 minutes. The simulations are run on an Intel® Core(TM) i5-6600K 4 core CPU running at 3.50GHz. Both OpenMC and Serpent support shared memory parallelisation with OpenMP. This feature is used to run the simulations in parallel on 4 cores.

Table 5.4: CR bank and SD bank reactivity worth

(a) CR bank k_{eff}

Type	OpenMC
Case (ii)	1.01390±0.00013
Case (iv)	1.00624±0.00015
Reactivity worth [pcm]	750±28
Case (i)	1.01468±0.00014
Case (v)	1.00599±0.00014
Reactivity worth [pcm]	851±28

(b) SD bank k_{eff}

Type	OpenMC
Case (ii)	1.01381±0.00014
Case (iv)	1.00591±0.00014
Reactivity worth [pcm]	774±28
Case (i)	1.01468±0.00014
Case (v)	1.00582±0.00014
Reactivity worth [pcm]	868±28

It should be remembered that the total worth of a single CR assembly has to be limited to $0.5\beta_{eff}$ in order to not have a disastrous accident if there is an inadvertent withdrawal of CR during normal operation at peak reactivity potential of the core. The worth of the single CR assembly is therefore $141\pm 5pcm$. Table 5.5 presents some results for cases where both CR and SD are inserted and when only 1 CR assembly is inserted. The worth of the single CR assembly in this case is $137\pm 14pcm$.

Table 5.5: Results for different insertion cases

Type	OpenMC
Both CR/SD inserted	0.99938±0.00014
1 CR inserted	1.01327±0.00014

5.3.1.3 Control Bank and Shutdown Bank S-Curve

Given that the control rods are inserted in the core sequentially during operation, the reactivity worth as a function of height in the core is of particular interest. Consider a case where the CR is positioned just above the AZ and is slightly inserted. The neutron flux at the axial periphery of the cylindrical core is minimum, as a result of minimal diffusion and increased leakage. Perturbing CR here will result in fewer absorption of neutrons, that is the reactivity worth of the absorber at the edges of the core is minimal. However for the same CR assembly placed in the central

regions, that have high neutron density, small perturbations of the CR will result in more neutrons being absorbed. Consequently the reactivity worth in the center of the core is the highest. These effects can be mapped as a function of reactivity worth against height, which is generally called the *S-curve*. The S-curves for both CR and SD absorber assembly is determined by running a series of Monte Carlo simulations for different heights to which the banks are inserted in the active region, as is shown in Figure 5.14a (iii) and 5.14b (iii) respectively. The S-curves determined for CR bank and SD bank are shown in Figure 5.15 and 5.16 respectively.

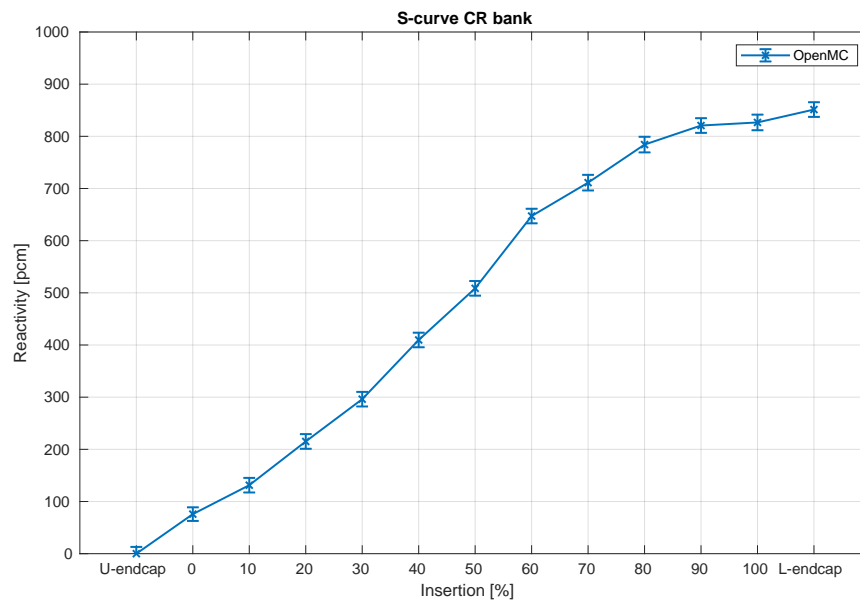


Figure 5.15: *S-curve for CR bank*

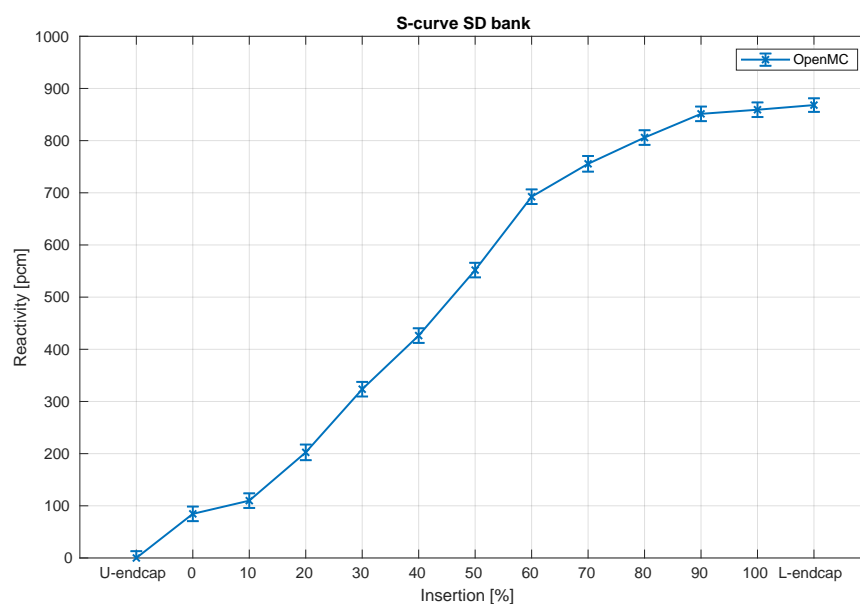


Figure 5.16: *S-curve for SD bank*

5.3.1.4 Power Distribution

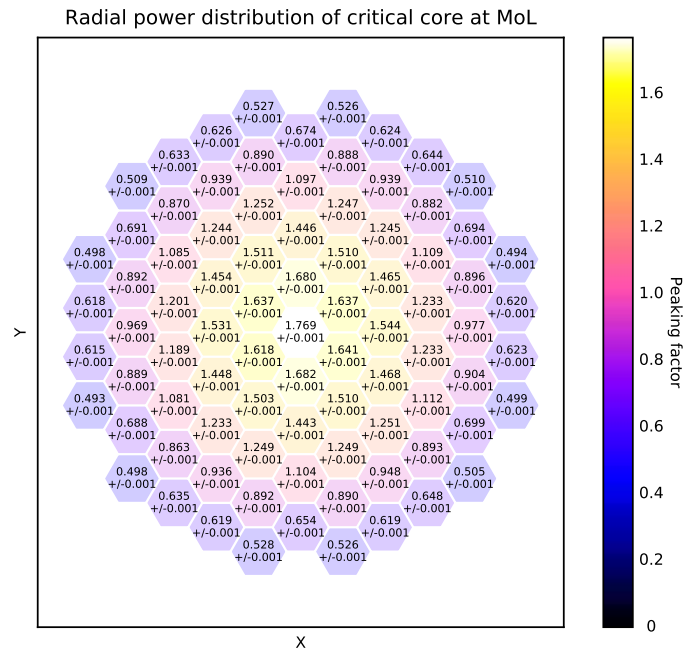


Figure 5.17: Assembly wise power distribution

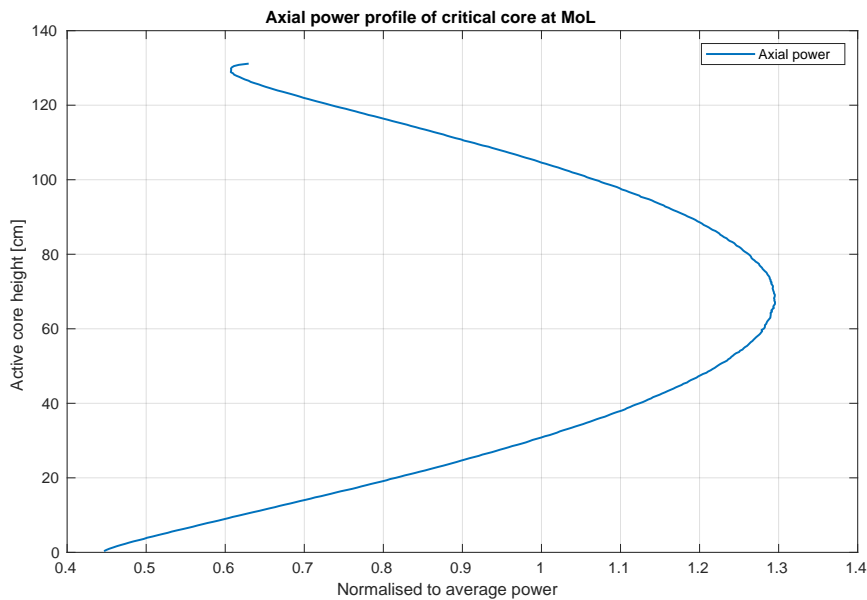


Figure 5.18: Core averaged axial power distribution

Using the S-curve for CR bank the position that brings the core critical can be determined. This position is determined to be 45cm above the bottom of AZ. The power distribution in the core at this state is characterised. Figure 5.17 presents the assembly wise radial power distribution of the core while Figure 5.18 shows the core

averaged axial peaking factor as determined by OpenMC. As seen, the maximum power is produced by the central assembly that is 1.769 times the core average. The axial peaking factor is approximately 1.29 at MoL. The axial profile, as mentioned in previous section, follows cosinus pattern.

5.3.1.5 Safety Parameters

This model of the core at MoL with CR at critical position and SD fully extracted is the reference position for determining the safety parameters of the core. As was mentioned earlier, OpenMC currently has no support to calculate kinetic parameters. Serpent, having the same core model, is run for this reason. A total of 640 million neutron histories is simulated to determine the kinetic parameters, shown in Table 5.6 [63].

Table 5.6: Kinetic parameters at MoL

Parameter	Value	Unit
Λ_{eff}	390.9 ± 0.2	<i>ns</i>
β_{eff}	576.6 ± 0.3	<i>pcm</i>

Having determined the point kinetic parameters, the reactivity coefficients are calculated by the procedure described here. The reactivity coefficients are determined using OpenMC code. The way to determine these coefficients is by perturbing the core from the reference/nominal case X_0 . The perturbation Y , is assumed to linearly affect the reactivity ρ , as given by the Equation 5.14, that is similar to basically a difference quotient used as first order numerical approximation.

$$\left[\frac{\partial \rho}{\partial X} \right]_{X_0} \approx \frac{\rho_{X_0+Y} - \rho_{X_0}}{Y} \quad (5.14)$$

Nominal Case

This is the nominal case where all the materials are in their hot state, the CR is at the critical position, SD is extracted completely. The effective neutron multiplication factor in the nominal case is

$$k_{eff-nom} = 1.00745 \pm 0.00013$$

Doppler Constant

It was explained earlier that *Doppler coefficient* (α_D) is driven by changes in fuel temperature affecting the absorption cross section of some fertile isotope. The coefficient is a function of temperature, however this becomes quite difficult to comprehend, and another term *Doppler constant* (K_D) is defined $[\partial \rho / \partial \ln T_f]_{T_{f_0}}$, which assumes logarithmic dependence of the coefficient, which is defined by Equation 3.3. Expanding this equation along with Equation 3.1 gives Equation 5.15.

$$\alpha_D = \frac{d\rho}{dT_f} = \frac{1}{k^2} \frac{dk}{dT_f} \quad (5.15)$$

K_D is related to α_D as

$$\alpha_D = \frac{K_D}{T_f} \quad (5.16)$$

K_D is related to ρ as

$$K_D = \frac{d\rho}{d\ln T_f} \quad (5.17)$$

By fitting a logarithmic equation we can determine the constant.

$$k(T) = k(0) - K_D \ln(T_f) \quad (5.18)$$

Procedure

The JEFF-3.1.1 cross section temperatures of the fuel material are changed to the following temperatures.

Temperature [K] 300 600 900 1200 1500 1800

Table 5.7 provides the k_{eff} values for the different temperatures of the fuel cross section. Figure 5.19 graphically presents the variation of reactivity with temperature.

Table 5.7: k_{eff} at different cross section temperatures

Temperature [K]	k_{eff}
300	1.01336 ± 0.00015
600	1.01012 ± 0.00014
900	1.00745 ± 0.00013
1200	1.00621 ± 0.00014
1500	1.00483 ± 0.00014
1800	1.00398 ± 0.00014
ρ [pcm]	$(4304 \pm 268) - (521 \pm 39) \ln T_f$
α_D [pcm/K]	$(-521 \pm 39)/T_f$
K_D [pcm]	-521 ± 39

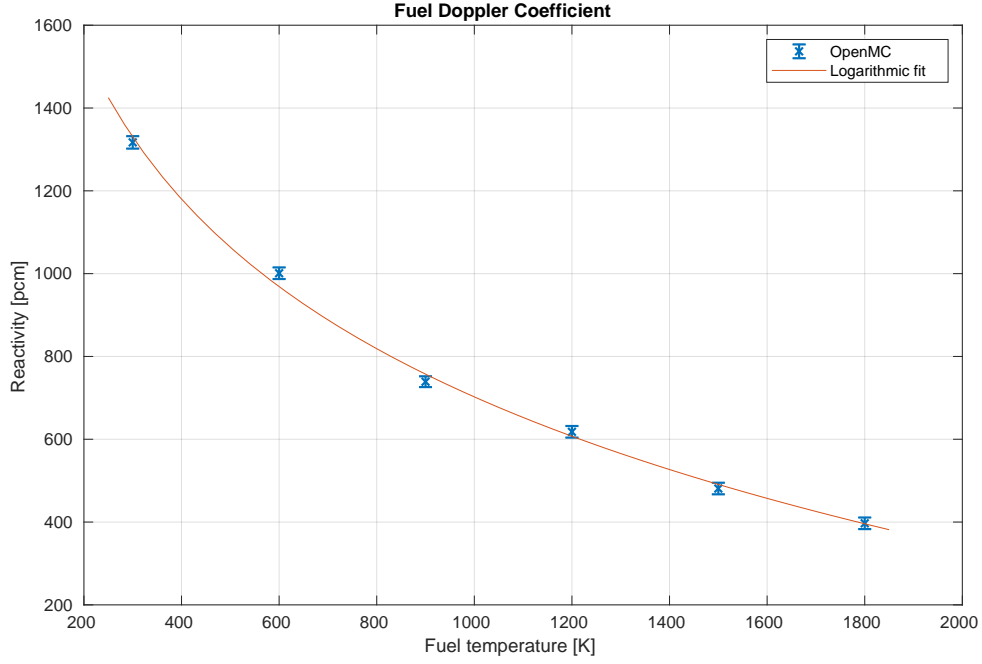


Figure 5.19: Variation of reactivity with fuel temperature

Fuel Axial Coefficient

Fuel axial coefficient is driven by changes in fuel temperature $[\partial\rho/\partial h_f]_{h_{f_0}}$, and can be expressed as

$$\alpha_{fuel-axial} = \frac{d\rho}{dT_f} \quad (5.19)$$

Procedure

The procedure to determine the coefficient is by perturbing the axial height of the fuel column h_{f_0} which is at temperature T_0 . This perturbation is assumed to be caused by thermal expansion, Equation 5.20. Any change in dimension by thermal expansion causes corresponding change in density, Equation 5.21. Consequently the procedure entails making changes to fuel height and fuel density in the input file. The coefficient is determined by finding a linear fit to the data of reactivity as a function of fuel temperature. It is to be noted here that temperature of fuel is not changed in the input file, nominal temperature is retained, as otherwise it would result in simultaneous monitoring of Doppler and fuel expansion effects without separating the two, which is our objective.

$$h_Y(T_Y) = h_{f_0}(T_0)[1 + \alpha_{UN}(T_0 - T_Y)] \quad (5.20)$$

$$\rho_{UN_Y}(T_Y) = \frac{\rho_{UN_0}(T_0)}{1 + \alpha_{UN}(T_0 - T_Y)} \quad (5.21)$$

The height is perturbed as shown in Figure 5.20, corresponding to thermal expansion until melting limit of UN fuel, as follows.

Temperature [K]	429.15	929.15	1429.15	1929.15	2429.15
Height expansion [%]	-0.4	0	+0.44	+0.91	+1.42
Density expansion [%]	+0.4	0	-0.44	-0.91	-1.42

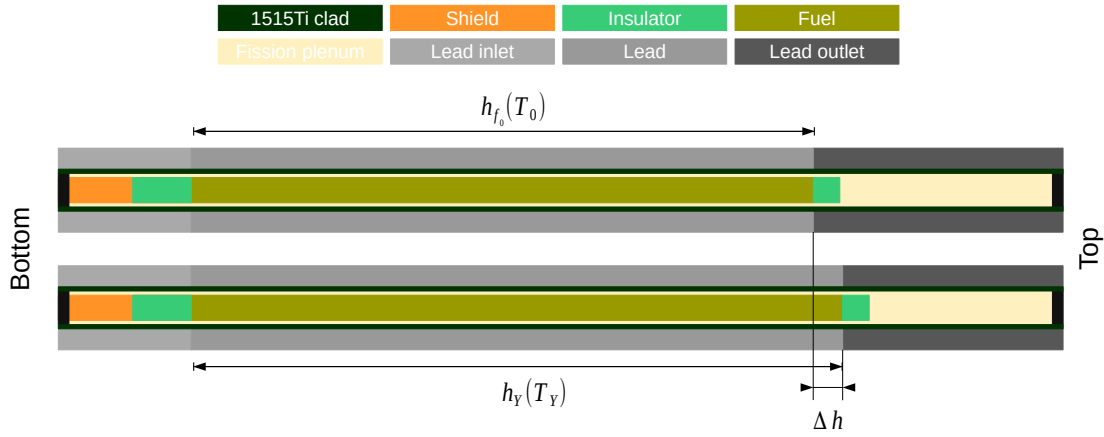


Figure 5.20: Height of fuel pellet perturbed in fuel rod

Figure 5.21 graphically presents the variation of reactivity with temperature while Table 5.8 provides the k_{eff} values for the different axial expansions.

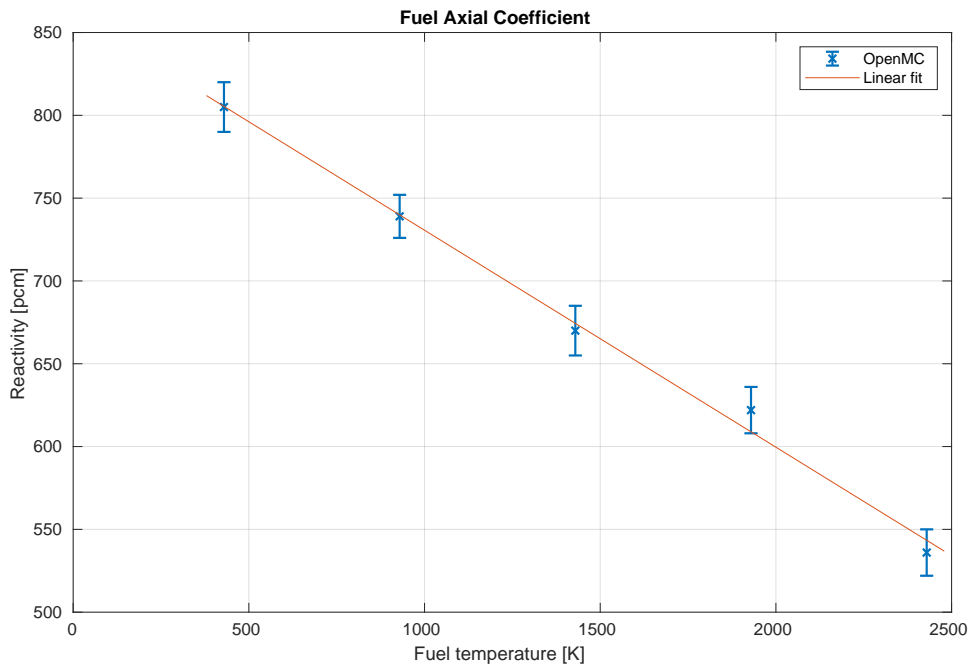


Figure 5.21: Variation of reactivity with fuel temperature

Table 5.8: k_{eff} at different fuel axial expansions

Temperature [K]	k_{eff}
429.15	1.00812±0.00015
929.15	1.00745±0.00013
1429.15	1.00647±0.00015
1929.15	1.00626±0.00014
2429.15	1.00539±0.00014
ρ [pcm]	$-(0.131 \pm 0.018)T_f + (861.6 \pm 29.1)$
$\alpha_{fuel-axial}$ [pcm/K]	-0.131 ± 0.018

Fuel Radial Coefficient

Fuel radial coefficient is driven by changes in fuel temperature $[\partial\rho/\partial d_f]_{d_{f_0}}$, and can be expressed as

$$\alpha_{fuel-radial} = \frac{d\rho}{dT_f} \quad (5.22)$$

Procedure

The procedure to determine the coefficient is similar to earlier case, by perturbing the diameter of the fuel column d_{f_0} which is at temperature T_0 . This perturbation is assumed to be caused by thermal expansion, Equation 5.23. Any change in dimension by thermal expansion causes corresponding change in density, Equation 5.21.

$$d_Y(T_Y) = d_{f_0}(T_0)[1 + \alpha_{UN}(T_0 - T_Y)] \quad (5.23)$$

The diameter is perturbed as shown in Figure 5.22, corresponding to thermal expansion until melting limit of UN fuel, as follows.

Temperature [K]	429.15	929.15	1429.15	1929.15	2429.15
Diameter expansion [%]	-0.4	0	+0.44	+0.91	+1.42
Density expansion [%]	+0.4	0	-0.44	-0.91	-1.42

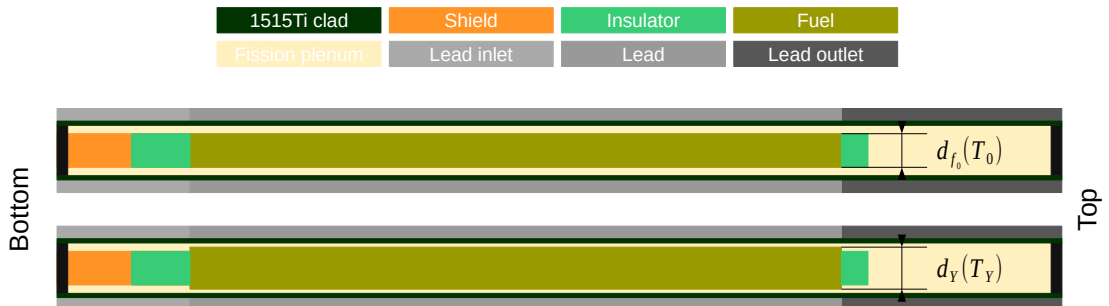


Figure 5.22: Diameter of fuel pellet perturbed in fuel rod

Table 5.9 provides the k_{eff} values for the different radial expansions. Figure 5.23 graphically presents the variation of reactivity with temperature.

Table 5.9: k_{eff} at different fuel radial expansions

Temperature [K]	k_{eff}
429.15	1.00758 ± 0.00015
929.15	1.00745 ± 0.00013
1429.15	1.00741 ± 0.00015
1929.15	1.00750 ± 0.00014
2429.15	1.00740 ± 0.00018
ρ [pcm]	$-(0.008 \pm 0.014)T_f + (751.8 \pm 23.4)$
$\alpha_{fuel-radial}$ [pcm/K]	-0.008 ± 0.014

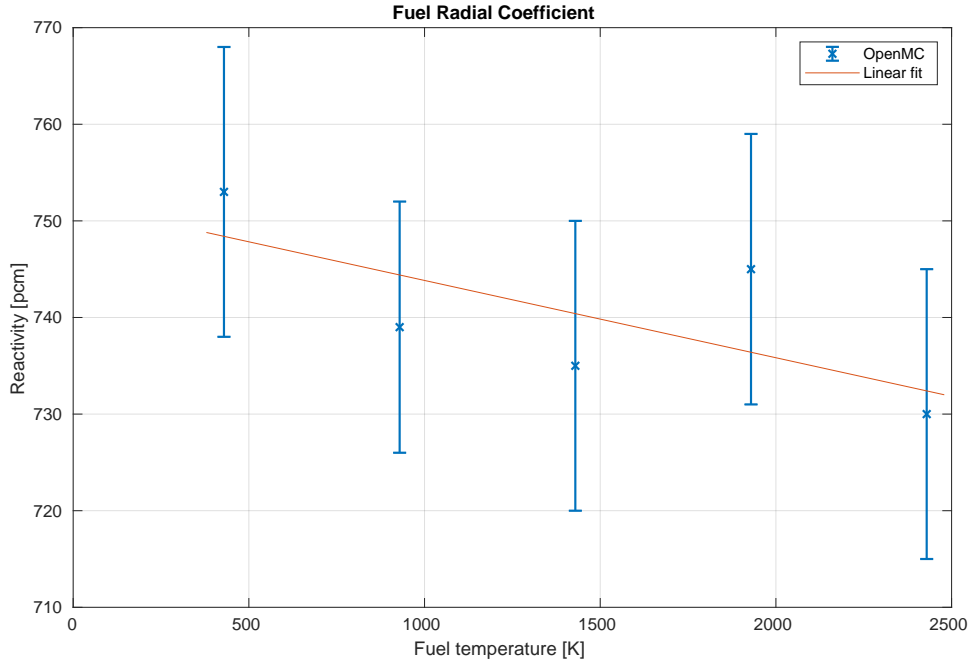


Figure 5.23: Variation of reactivity with fuel temperature

Coolant Density Coefficient

Coolant density coefficient $[\partial\rho/\partial\rho_{pb}]_{\rho_{pb_0}}$ is driven by changes in moderator temperature, and can be expressed as

$$\alpha_{coolant} = \frac{d\rho}{dT_{pb}} \quad (5.24)$$

Procedure

The procedure to determine the coefficient is by perturbing the density of the coolant ρ_{pb_0} which is at temperature T_0 . The procedure entails changing coolant density on the AZ corresponding to changes in temperature, retaining the cross section temperature in the input file. The density is perturbed until boiling limit of lead coolant, as follows.

Temperature [K]	623.15	758.15	1061.9	1365.65	1669.4	1973.15
Density expansion [%]	+1.7	0	-3.45	-7.64	-11.47	-15.3

Table 5.10 provides the k_{eff} values for the different density temperatures. Figure 5.24 graphically presents the variation of reactivity with temperature.

Table 5.10: k_{eff} at different coolant temperatures

Temperature [K]	k_{eff}
623.15	1.00761 ± 0.00014
758.15	1.00745 ± 0.00013
1061.9	1.00784 ± 0.00014
1365.65	1.00819 ± 0.00015
1669.4	1.00849 ± 0.00014
1973.15	1.00863 ± 0.00015
ρ [pcm]	$+(0.089 \pm 0.032)T_{pb} + (685.5 \pm 43.4)$
$\alpha_{coolant}$ [pcm/K]	$+0.089 \pm 0.032$

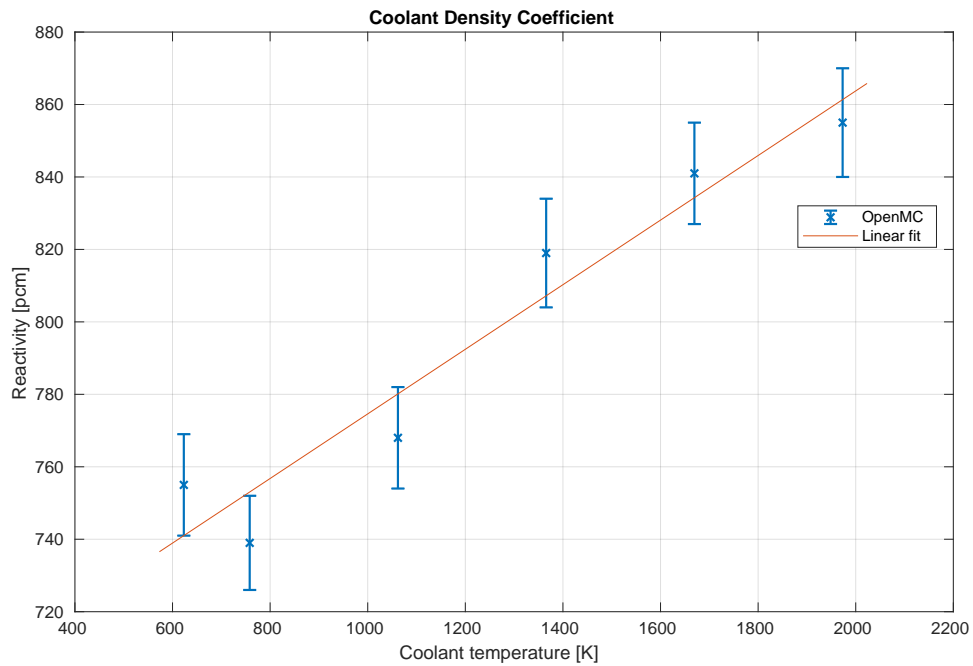


Figure 5.24: Variation of reactivity with coolant temperature

Core Radial Coefficient

Core radial coefficient is driven by changes in diagrid temperatures $[\partial\rho/\partial p_w]_{w_{w_0}}$, and can be expressed as

$$\alpha_{core-radial} = \frac{d\rho}{dT_w} \quad (5.25)$$

Procedure

The procedure to determine the coefficient is by perturbing the temperature of the diagrid T_{w0} . Diagrid temperature is changed which causes expansion of the assembly pitch. The wrapper face to face dimension is maintained while only the pitch is varied in the input file. Figure 5.25 shows the assembly pitch expansion. The temperature of the diagrid is increased until melting point of the steel.

Temperature [K]	443.15	693.15	943.15	1193.15	1443.15
Pitch expansion [%]	-0.31	0	+0.33	+0.67	+1.05

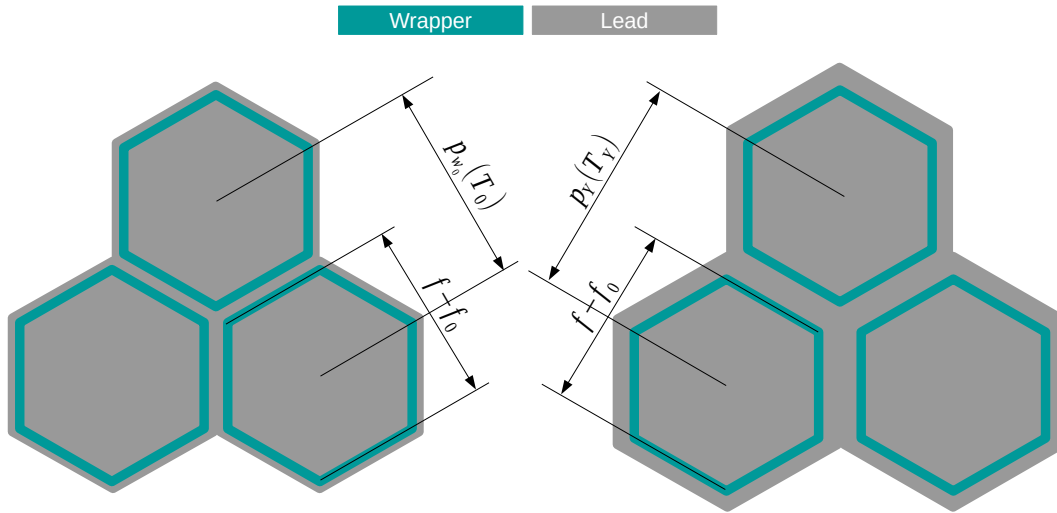


Figure 5.25: Assembly wrapper pitch perturbed in the core

Table 5.11 provides the k_{eff} values for the different pitch expansions. Figure 5.26 graphically presents the variation of reactivity with temperature.

Table 5.11: k_{eff} at different diagrid temperatures

Temperature [K]	k_{eff}
443.15	1.00852 ± 0.00015
693.15	1.00745 ± 0.00013
943.15	1.00668 ± 0.00014
1193.15	1.00580 ± 0.00015
1443.15	1.00461 ± 0.00014
ρ [pcm]	$-(0.371 \pm 0.050)T_w + (1006 \pm 51)$
$\alpha_{core-radial}$ [pcm/K]	-0.371 ± 0.050

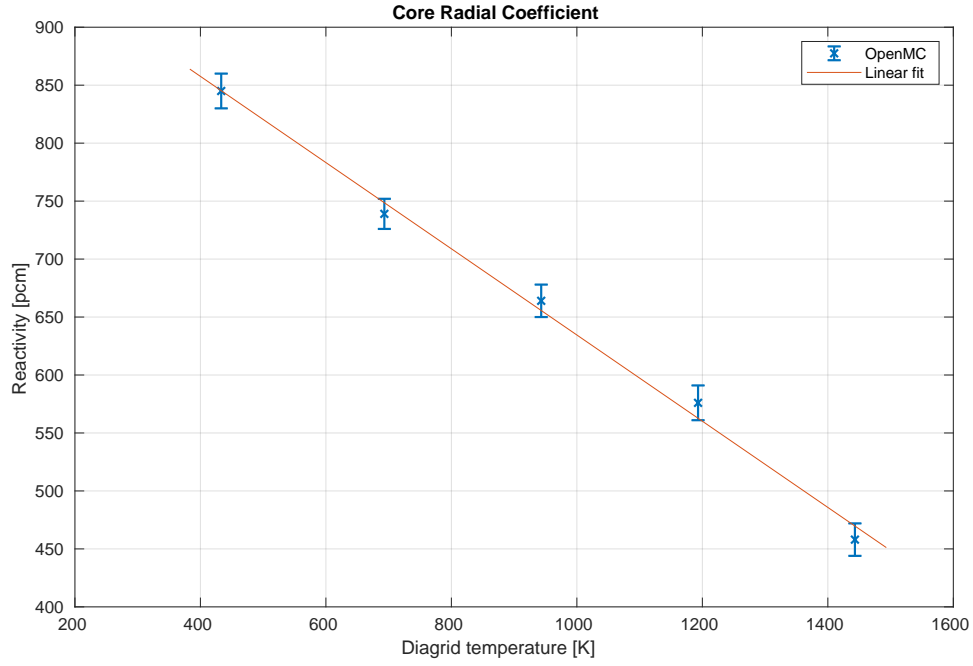


Figure 5.26: Variation of reactivity with diagrid temperature

Void Effect

Coolant voiding in LFRs is not probable, owing to high boiling point of lead (2022K). The void effect is studied to be coherent with studies conducted in SFRs.

Procedure

The procedure to determine the coolant void worth is by voiding the coolant in different zones as shown in Figure 5.27.

Table 5.12 provides the k_{eff} values for the different void zones.

Table 5.12: k_{eff} at different void zones

Zone	k_{eff}	Worth [pcm]
Zone 1	1.01348 ± 0.00014	+608
Zone 2	1.00311 ± 0.00014	-412
Zone 3	1.00577 ± 0.00015	-149
Zone 4	1.00445 ± 0.00014	-279

The total reactivity due to any perturbation in the temperature (ΔT) can then be written in a form as shown in Equation 5.26

$$\alpha_{tot} = (\alpha_{Doppler} + \alpha_{fuel-axial} + \alpha_{fuel-radial}) * \Delta T_f + \alpha_{coolant} * \Delta T_{pb} + \alpha_{core-radial} * \Delta T_w \quad (5.26)$$

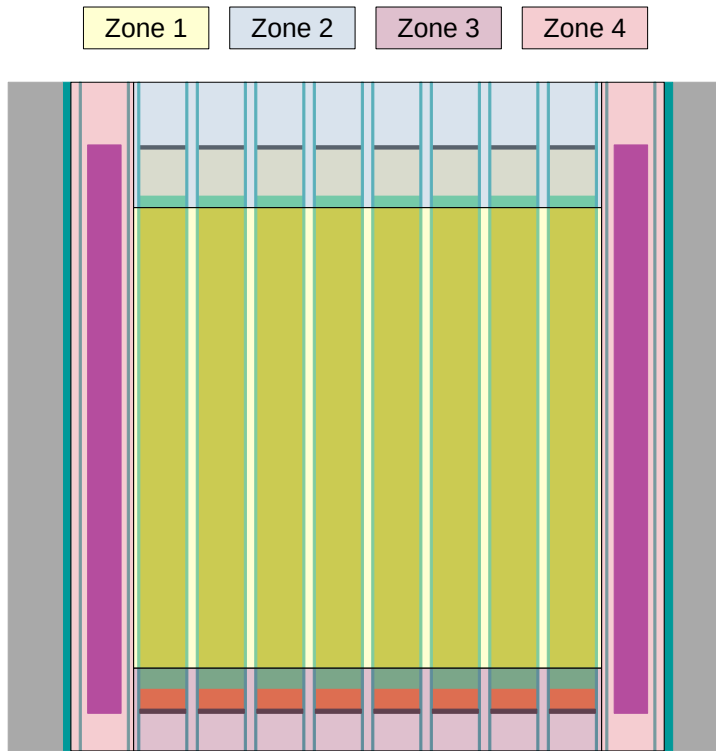


Figure 5.27: Coolant void zones

Remarks

It should be mentioned here that some additional coefficients were studied, namely the *clad coefficient*, *wrapper coefficient*⁴, *coolant density coefficients* for different zones. These coefficients, however, had no appreciable trend to be fitted with a linear curve, and the uncertainties overshadowed any trend that could be found. Therefore these coefficients are neglected in Equation 5.26.

⁴See Appendix A for the plots

The main objective of the thesis is the study of the passive shutdown system. In this regard the gravity driven insertion of the shutdown assemblies is analysed, starting with the general description of the intended system and the modelling of the gravity driven insertion. During the preliminary calculations it was realised that gravity insertion may not be feasible, and as an alternative the buoyancy driven insertion was also studied. From the initial literature survey it was discovered that a typical limit for insertion time expected for a motor driven control assembly is 6s [42]. As the current study is on LFRs with sufficient negative reactivity coefficients, an objective limit for insertion of gravity-assisted shutdown assembly is chosen at 10s.

6.1 Overview

In order to achieve gravity driven insertion in LFRs, having molten lead as the coolant, will require a dense material to *sink* in the coolant. The material should possess good compatibility in the corrosive lead environment. It should be able to bear high fluence in the reactor for a long time, given that SEALER-UK is a battery type reactor. More importantly the material must have good neutron absorption cross section in the fast spectrum region, to regulate neutron flux in the core under abnormal conditions. In order to satisfy the Gen. IV goals, such a system must be economically feasible.

The probable materials that are applicable in fast spectrum reactors is different from those applicable in thermal spectrum reactors. The so called *conventional absorbers* are enriched boron carbide, cadmium and alloys of hafnium or silver-indium-cadmium. However in fast spectrum the latter absorbers have smaller absorption cross sections, effectively lowering the reactivity worth [64]. In fast spectrum applications the leading contenders include compounds such as boron carbide, europium hexaboride and sesquioxide. These compounds have densities in the range much less than that of lead, at $2.5g/cm^3$, $4.9g/cm^3$ $6-7g/cm^3$ respectively, necessitating insertion by buoyancy. This requires designing longer reactors, because buoyancy assisted insertion is initiated from the bottom of the core.

Absorber elements with even higher densities are necessary for gravity assisted shutdown, ideally greater than $10.7g/cm^3$ (at melting point of lead). Ceramic borides are some of the preferred materials, because they are dense, tend to have

desirable neutronic properties and physical properties and can be fabricated with conventional methods. Borides of zirconium, tantalum, vanadium and hafnium, ceramic of hafnium diboride and hafnium dioxide (HfB_2, HfO_2), rhenium diboride (ReB_2), osmium diboride (OsB_2) and tungsten-rhenium diboride (WB_2, ReB_2) are such materials that have sufficiently high density, given in Table 6.1.

Table 6.1: Absorber theoretical density [18],[65],[66]

Material	Density g/cm^3
$HfB_2 + HfO_2$	11.1
ReB_2	12.7
OsB_2	12.9
$WB_2 + ReB_2$	12.3

Of these absorbers, hafnium diboride and dioxide compound, while having theoretically higher density than lead, has as-fabricated density with porosity, that results in unfeasible lower density. The rest of the contenders have sufficient density on fabrication, but economic feasibility is the concern, as the rare metals are very expensive in the market. Pure rhenium diboride and osmium diboride though highly dense are expensive. A solid solution tungsten-rhenium diboride, least dense of the three latter ceramic absorbers, is the proposed absorber for shutdown application. The other options could be selected if it is determined that tungsten-rhenium diboride is not feasible. Table 6.2 presents the total neutron induced cross sections for the elements in the material. In the fast spectrum it is seen, both tungsten and rhenium have similar cross sections, followed by boron. The high cross sections in the fast energy range provides $WReB_2$ with sufficient reactivity worth [65].

Table 6.2: $(n, total)$ cross section [barn][67]

Material	W^{182}	W^{184}	W^{186}	Re^{185}	Re^{187}	B^{10}	B^{11}
Abundance %	26.5	30.64	28.43	37.4	62.6	19.9	80.1
Thermal [0.025eV]	26.4	9	38.6	120	89.4	3870	5.08
Fast [0.1MeV]	9	9.5	9.5	9.25	9.25	4.85	4.4

6.1.1 Tungsten-Rhenium Diboride

A super-hard ceramic boride, tungsten-rhenium diboride ($WReB_2$), is a solid solution of two metal diborides, rhenium diboride (ReB_2) and tungsten diboride (WB_2). Pure ReB_2 is a very dense, hexagonal close packed crystallographic structure. In fact, it is one of the hardest known substance [18]. Being an expensive element, it is mixed with WB_2 , which is miscible in the solid solution, for applications requiring better economics. Pure WB_2 has a slightly less packed hexagonal AlB_2 structure, shown in Figure 6.1. The pure WB_2 has layers of tungsten and boron elements in alternate planes. Pure ReB_2 has a more densely packed, with a zig-zag pattern. WB_2 also occupies a native W_2B_4 type structure. While WB_2 is not found to have the ReB_2 phase in any condition, the W_2B_4 is partially similar to the ReB_2 . It is this property which makes possible the dissolution of WB_2 in ReB_2 . The limit of

dissolution of WB_2 in ReB_2 is determined to be 48% atomic, $(W_{0.48}Re_{0.52})B_2$ [18]. Figure 6.2 shows the density variation of the ceramic with changing atomic fraction of tungsten. For the study the material which reduces rhenium fraction is adopted¹. The theoretical density is $12.316g/cm^3$, and with a maximum fabrication porosity of 5% yields an equivalent $11.7g/cm^3$.

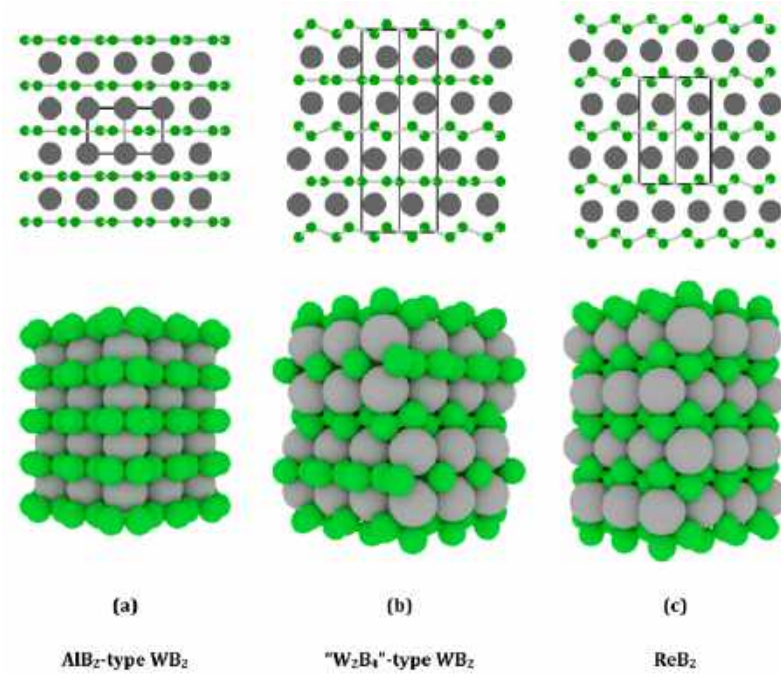


Figure 6.1: Comparison of crystallographic structures for WB_2 and ReB_2 [18]

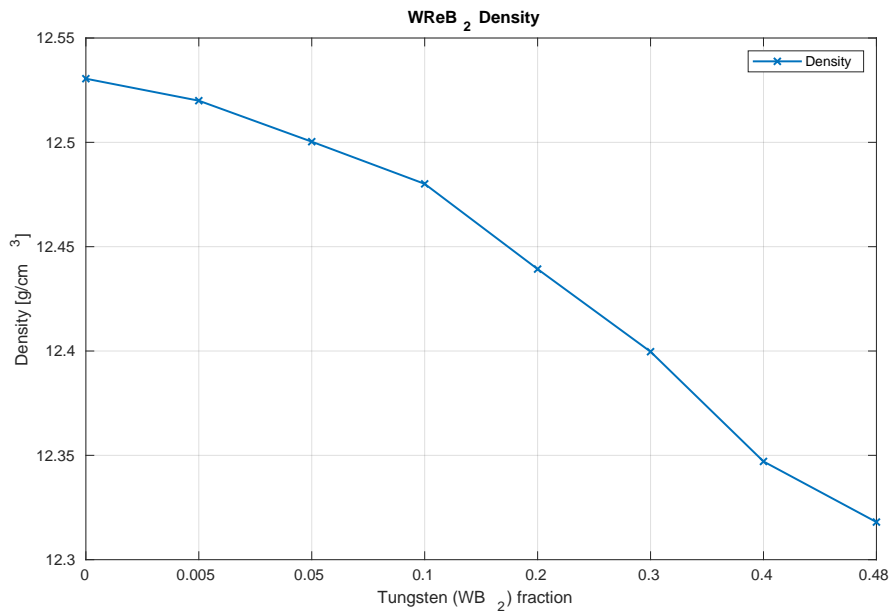
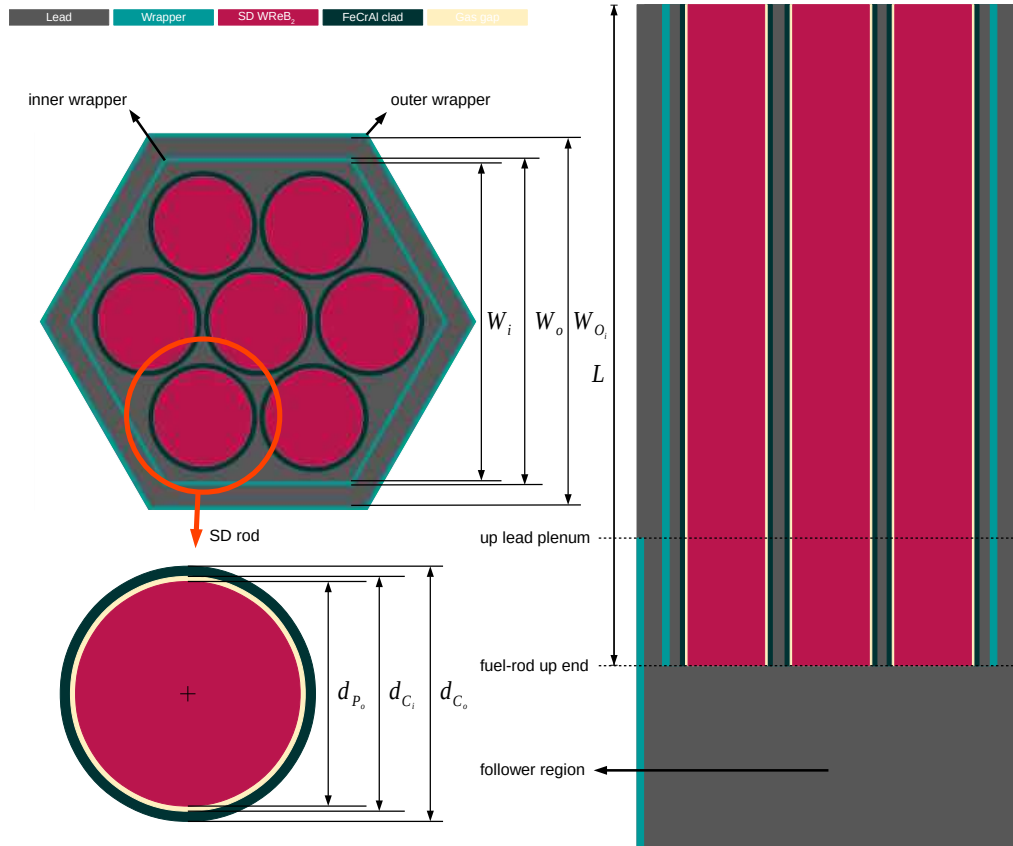


Figure 6.2: Density for $WReB_2$ at different tungsten fractions [Data extracted from [18]]

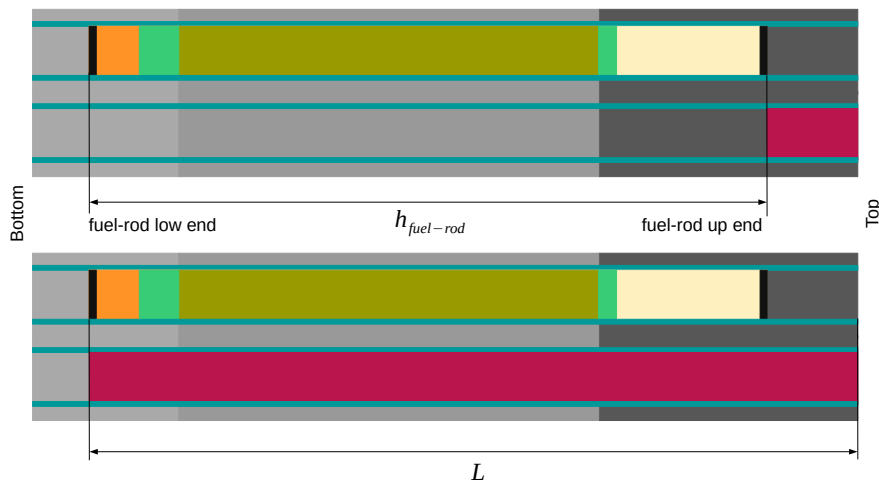
¹The same is also used in previous chapter for neutronic characterisation

6.2 Gravity Driven Insertion Model

The shutdown assembly consists of a hex can *FeCrAl* wrapper and 7 rods of absorber in a triangular lattice, shown in Figure 6.3a. These are the cold dimensions, in the previous chapter it was mentioned that the two absorber systems are in their cold state. The total effective length of the assembly is considered to cover fuel rod height when fully inserted, shown in Figure 6.3b.



(a) The shutdown assembly radial slice (upper left), axial slice (right) and the radial slice of the shutdown rod (bottom left)



(b) Representative image of shutdown assembly length

Figure 6.3: Representative graphics of the shutdown assembly and the channel

The absorber rod is provided with a small gas gap to allow for possible swelling in the rods due to irradiation. The assembly itself is housed in an empty outer hex can which extends until the height of the core. The assembly in normal conditions is raised to a parking position, with coolant filling the *follower region* below the assembly. The coolant in the follower region is assumed to be in forced convection, due to bypass flow from the core fuel assemblies. The dimensions of the parameters are given in Table 6.3. These dimensions are used to determine the volume, mass and weight required for the modelling. The objective of the modelling is to determine the insertion characteristics such as the forces acting on the assembly, the instantaneous velocity and acceleration of the assembly and the total time to reach intended position in the channel. The approach to determine these characteristics is from first principle mechanics of a freely falling body.

Table 6.3: Dimensions of the assembly parameters

Property	Value	Unit
Absorber rod	7 $WR\epsilon B_2$	
Pellet diameter d_{P_o}	0.04996	m
Clad inner diameter d_{C_i}	0.05022	m
Clad outer diameter d_{C_o}	0.05580	m
Inner wrapper		
Inner face to face W_i	0.16320	m
Outer face to face W_o	0.16700	m
Outer wrapper		
Inner face to face W_{O_i}	0.189557	m
Length L	2.26	m

6.2.1 Underlying Physics

One of the crude but effective way to describe the motion of the passive shutdown system driven by gravity is by describing the inherent forces acting on the body. From the information gathered in the literature review, it is known that the motion can be described by a simple balance of forces, Equation 6.1.

$$M \frac{dv}{dt} = F_{net} \quad (6.1)$$

M is the total mass (kg) of the system, v is the instantaneous velocity (m/s) of the system, t is the time (s) and F_{net} is the net force (N) acting on the body. The net force requires the knowledge of forces acting on the body. The following are assumed to influence the passively inserted body.

- Gravity - The forces of gravity is omnipresent, which is the main driving force.
- Buoyancy - Buoyancy forces arise from bodies submerged in a fluid, acting against the driving force.
- Drag - Drag forces are prevalent in fluid motion.

The net force F_{net} can then be expressed, incorporating these forces and attributing the correct sign to them, as in Equation 6.2.

$$F_{net} \downarrow = F_{gravity} \downarrow - F_{buoyancy} \uparrow - F_{drag} \uparrow \quad (6.2)$$

A representation of the forces acting on the body is presented in Figure 6.4. As it is presented, the coolant in the follower region is forced through the channel and the annular region between the inner and outer wrappers. A detailed description of how the forces are calculated is provided below.

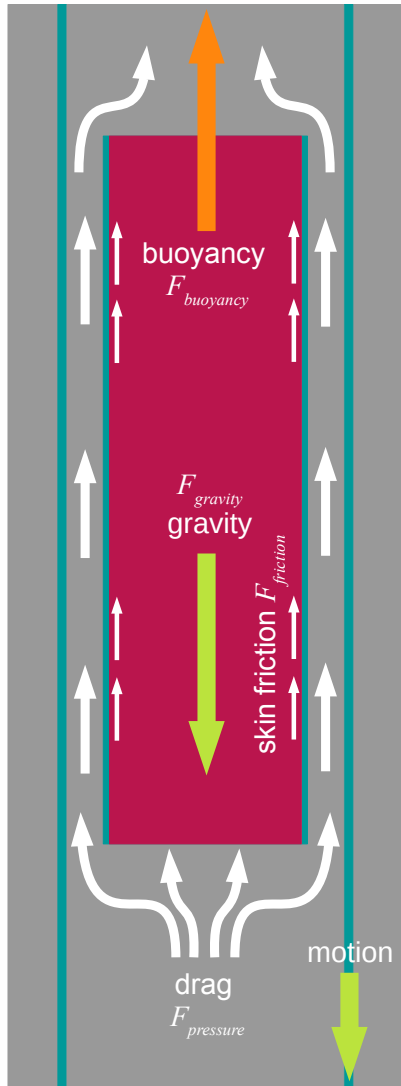


Figure 6.4: Various forces acting on the body

6.2.1.1 Gravity Force

Weight of the system determined by finding the volume of the respective materials, using the cold densities ($20^{\circ}C$) shown herein.

- $WReB_2$ pellet volume - 7 cylindrical rod

$$m_{pellet} = V_{pellet} * \rho_{WReB_2} \quad (6.3)$$

Material	Density	Units
<i>WReB₂</i> pellet	11,700	<i>kg/m³</i>
<i>FeCrAl</i> steel	7,170 [68]	<i>kg/m³</i>

V_{pellet} is

$$V_{pellet} = 7 * \frac{\pi d_{P_o}^2}{4} * L$$

- *FeCrAl* clad volume - 7 cylindrical tubes

$$m_{clad} = V_{clad} * \rho_{FeCrAl} \quad (6.4)$$

V_{clad} is

$$V_{clad} = 7 * \frac{\pi(d_{C_o}^2 - d_{C_i}^2)}{4} * L$$

- *FeCrAl* wrapper volume - 1 hex can

$$m_{wrapper} = V_{wrapper} * \rho_{FeCrAl} \quad (6.5)$$

$V_{wrapper}$ is

$$V_{wrapper} = \frac{\sqrt{3}(W_o^2 - W_i^2)}{2} * L$$

Total mass and volume is then

$$M_{tot} = m_{pellet} + m_{clad} + m_{wrapper} \quad (6.6)$$

$$V_{tot} = V_{pellet} + V_{clad} + V_{wrapper} \quad (6.7)$$

Pen and Paper Calculation

It is to be remembered that in order to simplify the study, the densities are assumed to be constant throughout the temperature ranges encountered in the core. The net mass calculated is $M_{tot} = 433kg$ and the net volume is $V_{tot} = 0.04081916m^3$. At an acceleration due to gravity of $9.816m/s^2$ in London [69] the total gravity force (weight) is

$$F_{gravity} = M_{tot} * 9.816 = 4252N$$

6.2.1.2 Buoyancy Force

Buoyancy forces are a result of differential pressure acting on the top and bottom surfaces of a submerged or partially submerged bodies. The pressure difference arise because a the pressure at the bottom surface is greater, because of the fluid column above, than the pressure at the top surface. If a bare cylinder with sufficient density is considered to be submerged in water, on can identify three surfaces, the top and bottom and the curved surface. The pressure acting on the curved surface cancels out as a consequence of *Pascals law*, which states pressure at a point in an

incompressible fluid acts in all directions equally and the pressure difference ΔP between two points at a distance h vertically is given as

$$\Delta P = \rho_{fl}gh$$

ρ_{fl} is the fluid density and g is acceleration due to gravity. Therefore, for the cylinder the pressure difference between the top and bottom faces is ΔP which gives the buoyancy force when it is multiplied with cross sectional area.

$$F_{buoyancy} = \Delta P * A = \rho_{fl}ghA = \rho_{fl}gV$$

V is the volume of body. The same holds true for oddly shaped bodies, where pressure forces in radial direction cancel out resulting in net pressure imbalance in vertical direction. A consequence of this is the *Archimedes principle*, which states that for bodies partially or fully immersed in a fluid, the buoyancy force is equal to the weight of the fluid displaced. Mathematically the buoyancy force can be expressed by Equation 6.8. A distinction needs to be made between volume of solid and displaced volume. A hollow sphere of diameters d_i and d_o has a body volume of

$$V_{hollow} = \pi \frac{(d_o^3 - d_i^3)}{6}$$

This volume exerts weight by gravity while the displaced volume contributing to buoyancy, is much larger

$$V_{disp} = \pi \frac{d_o^3}{6}$$

This distinction is also the case in the shutdown assembly. The total body volume is $V_{tot} = 0.04081916m^3$, while the displaced volume is slightly higher at $V_{disp} = 0.04114279m^3$. The extra value is because the volume occupied by the gas gap does not add to weight, but that volume adds to displaced volume and which adds to buoyancy. The buoyancy force for lead as the fluid can be expressed more clearly as shown in Equation 6.8.

$$F_{buoyancy} = \rho_{pb}gV_{disp} \quad (6.8)$$

The density of liquid lead ρ_{pb} is not a constant but varies with temperature. In fact, the density variation is high that it is envisaged for natural convection during *loss of flow accidents*, when pumping action is stopped. The density of lead in kg/m^3 [70] is given by Equation 6.9 for lead in temperature [in K] range 633-1973 K .

$$\rho_{pb} = 11470 - 1.3174 * T \quad (6.9)$$

The coolant conditions in the core is, however not constant, especially the temperature. The axial region corresponding to the AZ has a smooth profile starting from 420°C to 550°C as was determined in the T/H evaluation in the previous chapter, namely Figure 5.4. The axial variation of the density starting from the top of fuel rod to the bottom of fuel rod is shown in Figure 6.5. It is assumed in the study that the coolant channel in the SD assembly region is heated in a similar fashion as the coolant in the fuel assemblies. It is an approximation based on a presumption that heating of the lead in the inter-assembly gap heats the SD follower region.

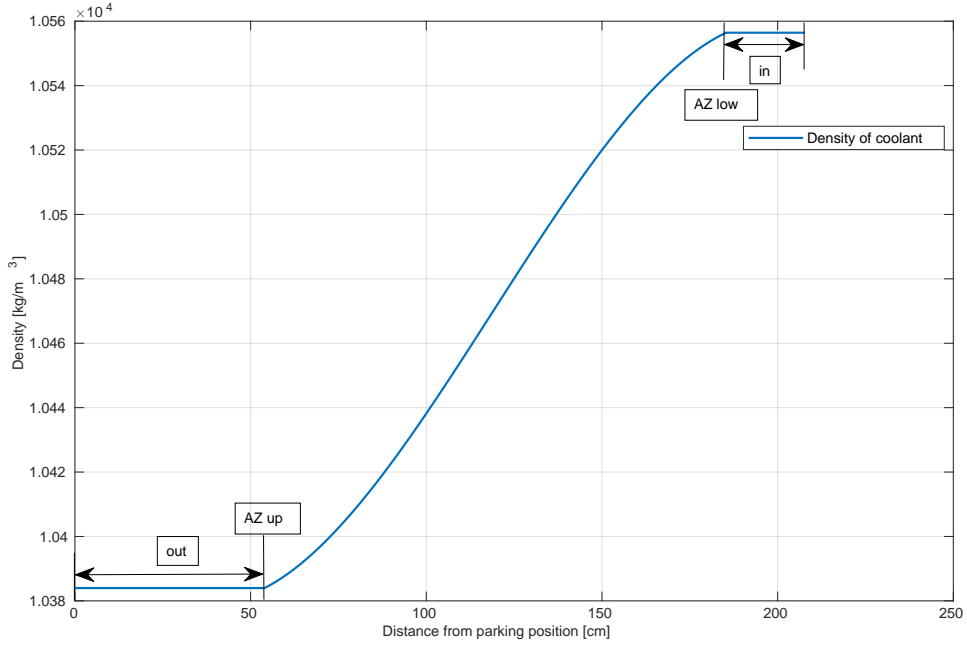


Figure 6.5: Coolant density variation along the core height

For the subsequent study the temperature variation is considered as follows, a pictorial representation is shown in Figure 6.6. When the SD assembly is inserted, it experiences a constant buoyancy force corresponding to constant density of coolant at outlet. Once it starts entering middle zone, the density of lead starts increasing which increases the buoyancy forces, and keeps increasing until it reaches the final position.

- Coolant above AZ is considered to be at a constant core outlet temperature 550°C , height of which is h_{up}
- Coolant in AZ is considered to smoothly transition from inlet to outlet, height of which is equal to that of fuel pellet, here noted as h_{mid}
- Coolant below AZ is considered to be at a constant core inlet temperature 420°C , height of which is h_{low}

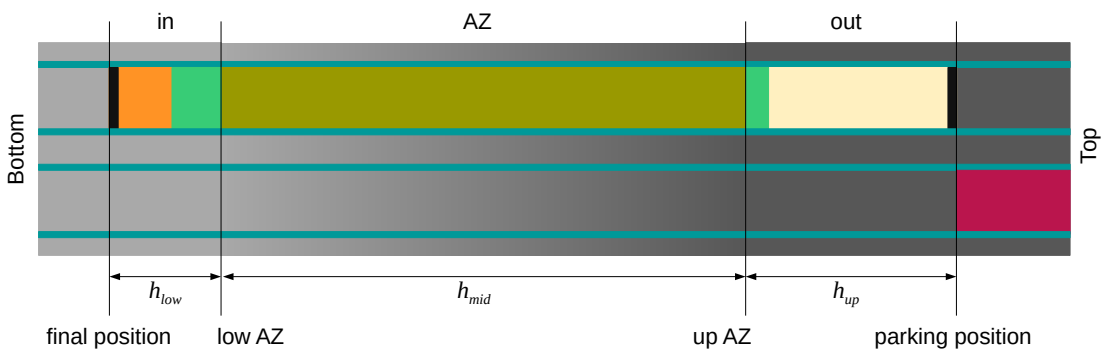


Figure 6.6: Representative graphics showing different coolant zones

Approximating the density, within the limits of temperature in the AZ, as a polynomial of distance from the top of AZ, x in m , the density in the three regions are given in Table 6.4.

Table 6.4: Characteristics of the three coolant zones

Region	Density [kg/m^3]	Height [m]
Low	10,556	0.225560
Mid	$(68.47 \pm 0.06)x^3 - (133.5 \pm 0.15)x^2 - (42.39 \pm 0.07)x + (823.15 \pm 0.05)$	1.311604
Up	10,384	0.539523

Pen and Paper Calculation

The value of buoyancy force considering a conservative value of density at outlet coolant temperature of $550^\circ C$ is

$$F_{buoyancy} = 10384 * V_{disp} * g = 4194N$$

6.2.1.3 Drag Force

A body in motion in a fluid experiences resistance due to two phenomena, *pressure* normal to the body surface and *shear* parallel to the body surface. The two components that effectively exerts force in the direction of fluid flow is called drag. Drag associated with pressure forces is *pressure drag* (PdA) while that associated with shear forces is *friction drag* or skin friction drag ($\tau_w dA$). Figure 6.7 shows the pressure and shear forces acting on a body.

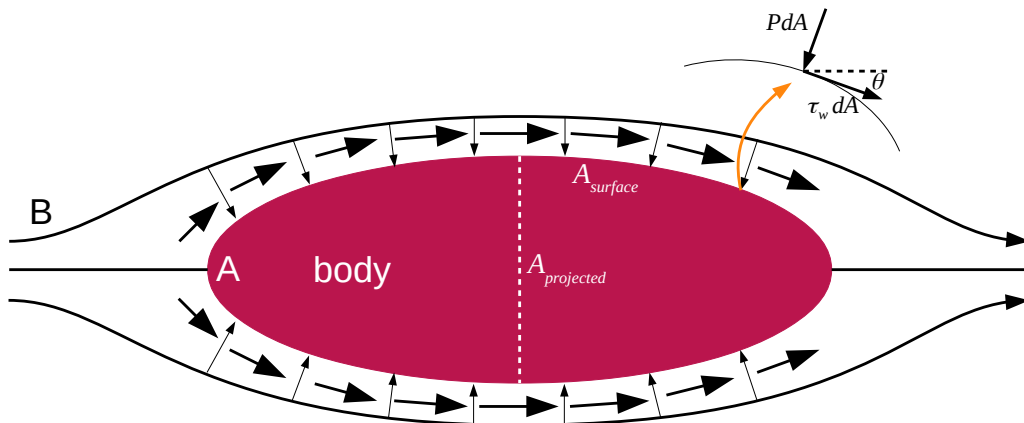


Figure 6.7: Representative graphics showing pressure and shear forces acting on a body in a flowing fluid

Pressure forces arise because of pressure difference between the front and back surfaces. The free stream fluid at B is essentially brought to a rest at point A , called a *stagnation point* that has a high *stagnation pressure* which is given by *Bernoulli equation* as

$$P_A = P_B + \frac{1}{2}\rho_{fl}v_B^2$$

In the direction of flow, the projected area of the body, is the maximum cross sectional area $A_{projected}$, and thus the pressure force is exerted on this area. This pressure component is dependent on the shape of the body and hence also commonly called *form drag*. Shear forces arise because of velocity gradient (du/dy) along the surface of the body. The shear stresses along the wall can be expressed as

$$\tau_w = \mu_{fl} \frac{du}{dy}$$

μ_{fl} is the dynamic viscosity (*Pas*) of the fluid, the velocity gradient du/dy depends on the *boundary layer* thickness (δ) of the flow. The shear force, which thus depends on the boundary layer thickness, and the pressure drag exerted over the entire surface can be given in a mathematical form as

$$D_{pressure} = \int_A P dA \cos\theta \quad , \quad D_{friction} = \int_A \tau_w dA \sin\theta$$

As it can be seen from the expression for the two drag forces, the total drag force depends on the shape of the body, which for complex bodies, is hard to compute theoretically and experimental observations or numerical solutions are necessary. These observations predict a general behaviour of the forces as a function of the *dynamic pressure* ($\frac{1}{2}\rho_{fl}v_\infty^2$), where v_{inf} is the free stream velocity, as given in Equation 6.10 and 6.11.

$$F_{pressure} = \frac{1}{2}\rho_{fl}v_\infty^2 A_{projected} C_D \quad (6.10)$$

$$F_{friction} = \frac{1}{2}\rho_{fl}v_\infty^2 A_{surface} C_F \quad (6.11)$$

C_D and C_F are dimensionless numbers called *drag coefficient* and *friction coefficient* respectively. Experimental observations have proven that these coefficients are a function of Reynolds number. C_D for different shapes is generally computed by experimental methods in wind tunnels or by employing CFD simulations. C_D varies according to flow regimes. For a sphere in laminar conditions C_D is given in terms of Reynolds number is given by Blasius as

$$C_D = \frac{24}{Re}$$

The variation of C_D at higher Re is given by various correlations [71], however a typical plot of C_D versus Re for the solid sphere and flow against a cylinder is given in Figure 6.8. This implies a thorough computation of the C_D is necessary for the shutdown assembly, for different flow conditions, which is explained in the next section.

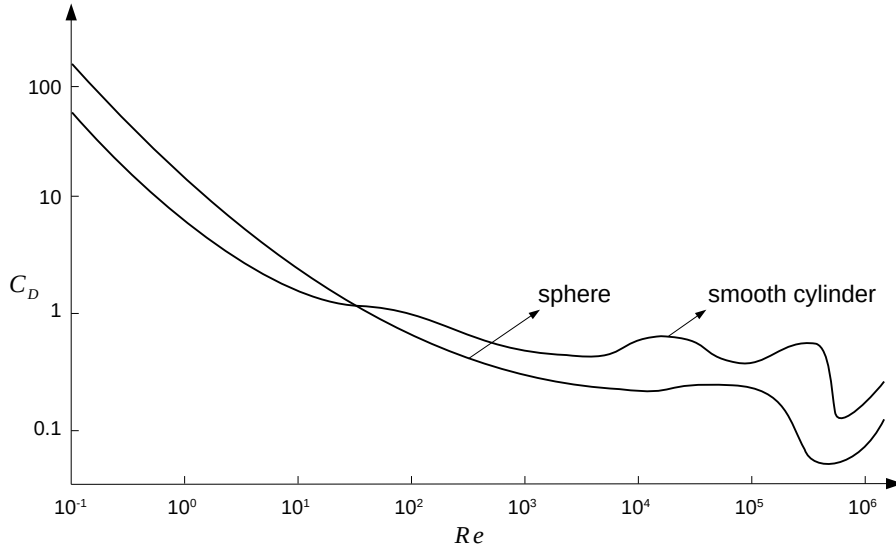


Figure 6.8: Average drag coefficient for cross flow over a smooth circular cylinder and a smooth sphere [72]

Skin friction coefficient C_F similarly is very dependent on the flow regime. It is relatively small for bodies perpendicular to the flow, but is predominant for parallel flow, such as flow over a flat plate. The coefficient is a function of local Reynolds number (Re_x), which is given mathematically by integrating local coefficient (C_{Fx}) throughout the length (L) as

$$C_F = \frac{1}{L} \int_0^L C_{Fx} dx \quad (6.12)$$

Re_x along the plate from the leading edge, is given in Equation 6.13.

$$Re_x = \frac{\rho_{fl} v_{\infty} x}{\mu_{fl}} \quad (6.13)$$

The coefficient is dependent on the boundary thickness which varies with Re_x as shown in Figure 6.9. As the flow transitions from laminar to turbulent, the boundary layer increases. The skin friction coefficient thus varies along the length of the plate.

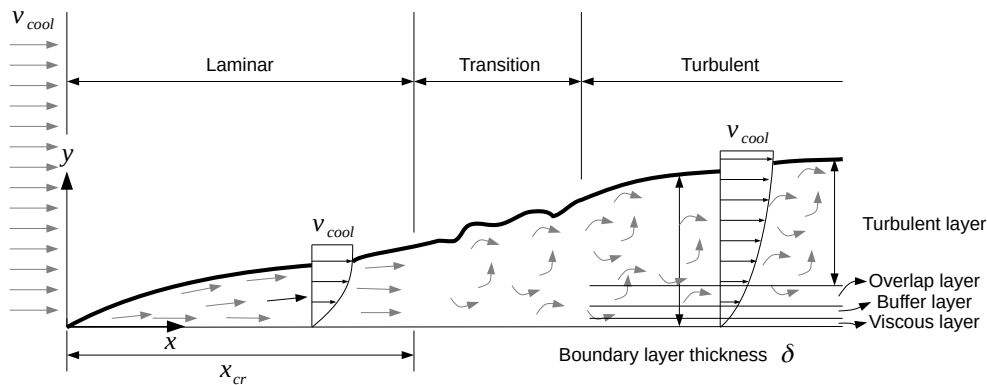


Figure 6.9: The development of the boundary layer for flow over a flat plate and the different flow regimes

A critical Reynolds number (Re_{cr} at x_{cr}) for the transition is generally assumed to occur at $5 * 10^5$. Laminar region is considered to be until $5 * 10^5$, while regions above this critical number is turbulent, including the intermediate transition region. The expressions used to calculate skin friction coefficient is given here [72]. The total $C_F x$ is also integrated assuming that the entire plate is in the laminar or turbulent regimes using Equation 6.12.

- Only laminar - $Re_L < 5 * 10^5$

$$C_{Fx} = \frac{0.664}{Re_x^{1/2}} \quad , \quad C_F = \frac{1.33}{Re_L^{1/2}} \quad (6.14)$$

- Only turbulent - $5 * 10^5 < Re_L < 10^7$

$$C_{Fx} = \frac{0.059}{Re_x^{1/5}} \quad , \quad C_F = \frac{0.074}{Re_L^{1/5}} \quad (6.15)$$

For conditions where the flow along the plate is partly laminar and partly turbulent Equation 6.12 can be use by splitting between laminar and turbulent flows as

$$C_F = \frac{1}{L} \left[\int_0^{x_{cr}} C_{Fx} + \int_{x_{cr}}^L C_{Fx} \right]$$

The total average skin coefficient for smooth and rough plates, with surface roughness δ is given in Equation 6.16 and 6.17 is graphically shown in Figure 6.10 for different surface roughness.

$$C_F = \frac{0.074}{Re_L^{1/5}} - \frac{1742}{Re_L} \quad (6.16)$$

$$C_F = \left(1.89 - 1.62 \log \frac{\epsilon}{L} \right)^{-2.5} \quad (6.17)$$

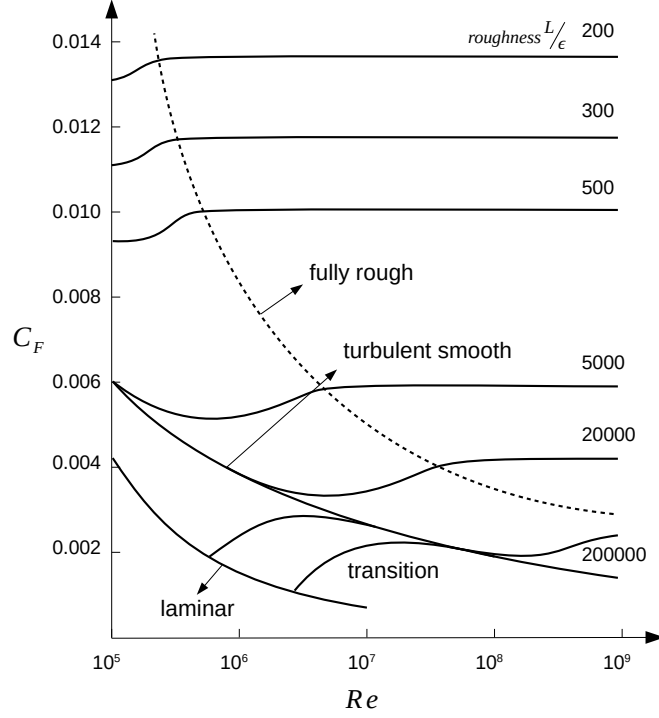


Figure 6.10: Plots of skin friction coefficient for smooth and rough flat plate at laminar, transition and turbulent flow regimes [72]

Depending on the flow velocity both the coefficients can be determined. The total drag force would then be a sum of pressure drag (6.10) and friction drag (6.11) as given in Equation 6.18

$$F_{drag} = \frac{1}{2} \rho_{fl} v_{\infty}^2 A_{projected} C_D + \frac{1}{2} \rho_{fl} v_{\infty}^2 A_{surface} C_F \quad (6.18)$$

For the models of the shutdown assembly considered in this study it is assumed that the cross sectional area is the hexagonal area ($A_{projected}$) of the inner wrapper, because from the coolants perspective it *sees* only the hexagonal area, as the assembly is axisymmetric and also because we assume that the coolant does not flow through the rods in the assembly. As a consequence of this assumption, the coolant flows outside the hex can of the assembly, which is the wetted surface area ($A_{surface}$ for 6 flat surfaces) contributing to the skin friction. The cross sectional area of the assembly consisting of only inner wrapper and rods is denoted as $A_{hex+rods}$, the free stream area inside the outer wrapper is denoted as A_{free} and the annular area between the inner and outer wrapper is denoted as $A_{annulus}$. The values are summarised in Table 6.5.

Table 6.5: Areas of interest

Parameter	Area [m^2]
$A_{projected}$	0.0241525
$A_{surface}$	1.3074212
$A_{hex+rods}$	0.0182047
A_{free}	0.0312493
$A_{annulus}$	0.0069653

Pen and Paper Calculation

We have calculated the total gravity force to be $4252N$ and total buoyancy force to be $4194N$. So in order for the shutdown assembly to be inserted downwards the net force downwards must be positive, that is the drag force must be at most $58N$. For the sake of simplicity if we only pressure drag to be relevant then the possible maximum value for the drag coefficient can be calculated. For average lead density of $10470kg/m^3$ and assumed arbitrary velocity of the coolant² $1m/s$, C_D is

$$58 = \frac{1}{2} * 10470 * 1^2 * 0.0241525 * C_D$$
$$\implies C_D = 0.458$$

This gives an idea of the possible limitations on our design that needs to be addressed. What can be said is that careful design of the assembly in order to reduce the magnitude of the drag coefficients is necessary. As the drag coefficient of the assembly is dependent on the profile, the foot of the assembly needs to be streamlined to reduce fluid resistance and consequently the drag coefficient.

6.2.2 Assembly Foot Design

A simple pen and paper calculation showed how the drag coefficient plays an important role in the passive insertion. The *foot* of the assembly in this context is the bottom part of the assembly that is typically fitted with tungsten ballast, or any other latching mechanism. This is the case for fuel assemblies, which needs to be weighed down to prevent them from floating to the top of the lead pool from buoyancy. Feet in shutdown assemblies is envisaged not to include a tungsten ballast, in order to minimise cost of expensive tungsten metal [8].

In order to proceed with numerical modelling of the insertion, a suitable feet profile would be necessary to incorporate in the model. On discovering that no previous drawings or sketches of the shutdown assembly was readily available, it was decided to design several feet profiles and study their behaviour in the fluid. 7 profiles, shown in Figure 6.11, were selected for a comparative study. The upper assembly portion is considered to be a hexagonal prism, while the bottom feet portions have the following profiles.

- Flat - A flat profile is the first case - denoted as *case_{flat}*. This would serve as a benchmark against other profiles. The average drag coefficient C_D of the closest resembling body, a cube, is 1.05 [72].
- Cone90 - Cone at 90° apex angle is the second case - denoted as *case_{cone90}*. Cones are some of the profiles that have very low drag coefficients. This profile has an approximate C_D of 0.66 [73].
- Cone60 - Cone at 60° apex angle is the third case - denoted as *case_{cone60}*. This profile has an average C_D of 0.5 [72].
- Cone45 - Cone at 45° apex angle is the fourth case - denoted as *case_{cone45}*. An approximate value for drag coefficient is 0.41 [73].

²The lead coolant velocity is limited by the technological constraints of erosion

- Hemisphere - A hemispherical profile - denoted as $case_{hemi}$ is the fifth profile. This profile has an average C_D of 0.4 [72].
- Ogive1 - Ogive is a pointed curve formed by intersecting circular arcs from the ends of a line. The ratio of the radii of the arc and the length of the line, is called the fineness number (f) or sharpness number. A semicircle is an ogive with f of 0.5. These profiles are generally incorporated in ballistic projectiles, for they have low drag, but higher lift [74]. The first of the cases has a fineness number of 1, denoted as $case_{ogive1}$.
- Ogive2 - The fineness number of the seventh profile considered is 1.2, denoted as $case_{ogive2}$.

Having identified the candidate profiles, the drag coefficients that were found in the literature were not exhaustive, particularly since the geometry of our shutdown model is not solely these profiles, but also an extended hexagonal prism. Another point of concern is that, the drag coefficient values that the literature provides for some of the profiles, is not specifically as a function of Reynolds number, in fact the range of Reynolds number that the values are provided at is not known.

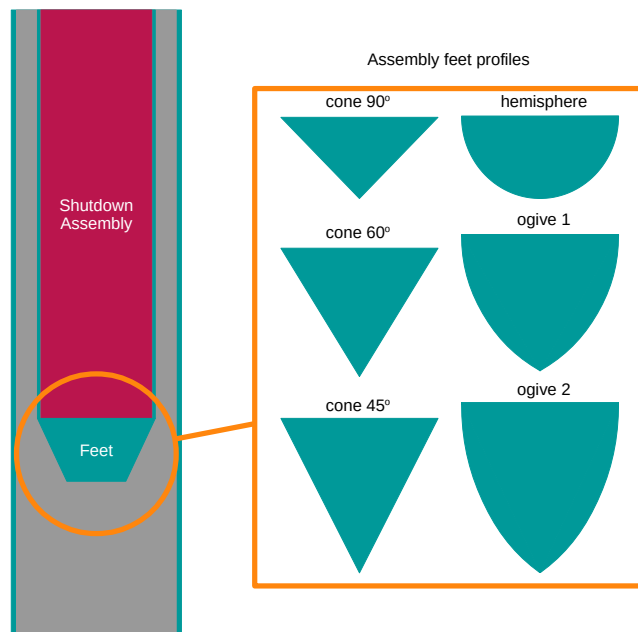


Figure 6.11: Representative images of the considered profiles

Having realised that it is important for us to know the specifics of the variation of the coefficient with Reynolds number, it was decided to perform *computational fluid dynamics* (CFD) simulations to determine the drag coefficients for different cases of Reynolds number. Preliminary calculations show that expected Reynolds number in the assembly channel is high, on account of high density of lead. Also from Figure 6.8 and 6.10, show that C_D variation is drastic for low Reynolds number, and saturates at high Reynolds number. The velocities of coolant flow considered for the CFD simulations are given in Table 6.6

Table 6.6: Velocity considered for CFD simulations

Velocity [m/s]	0.25	0.5	0.75	1.0
Reynolds number	2.5×10^5	5.0×10^5	7.5×10^5	1.0×10^6

6.2.2.1 Computational Fluid Dynamics

3D Model

Modelling of the profiles is done in ANSYS Workbench SpaceClaim Modelling Software [51], a general multi purpose tool for preparing 3D models. CFD simulations can mimic wind tunnel testing, that is, the model created has a computational domain, which is filled with fluid flowing around the body of interest. In SpaceClaim, the domain is a larger hexagonal prism, encompassing a hollow space shaped in the form of our body, in short a negative of our profile. Figure 6.12 shows the created models.

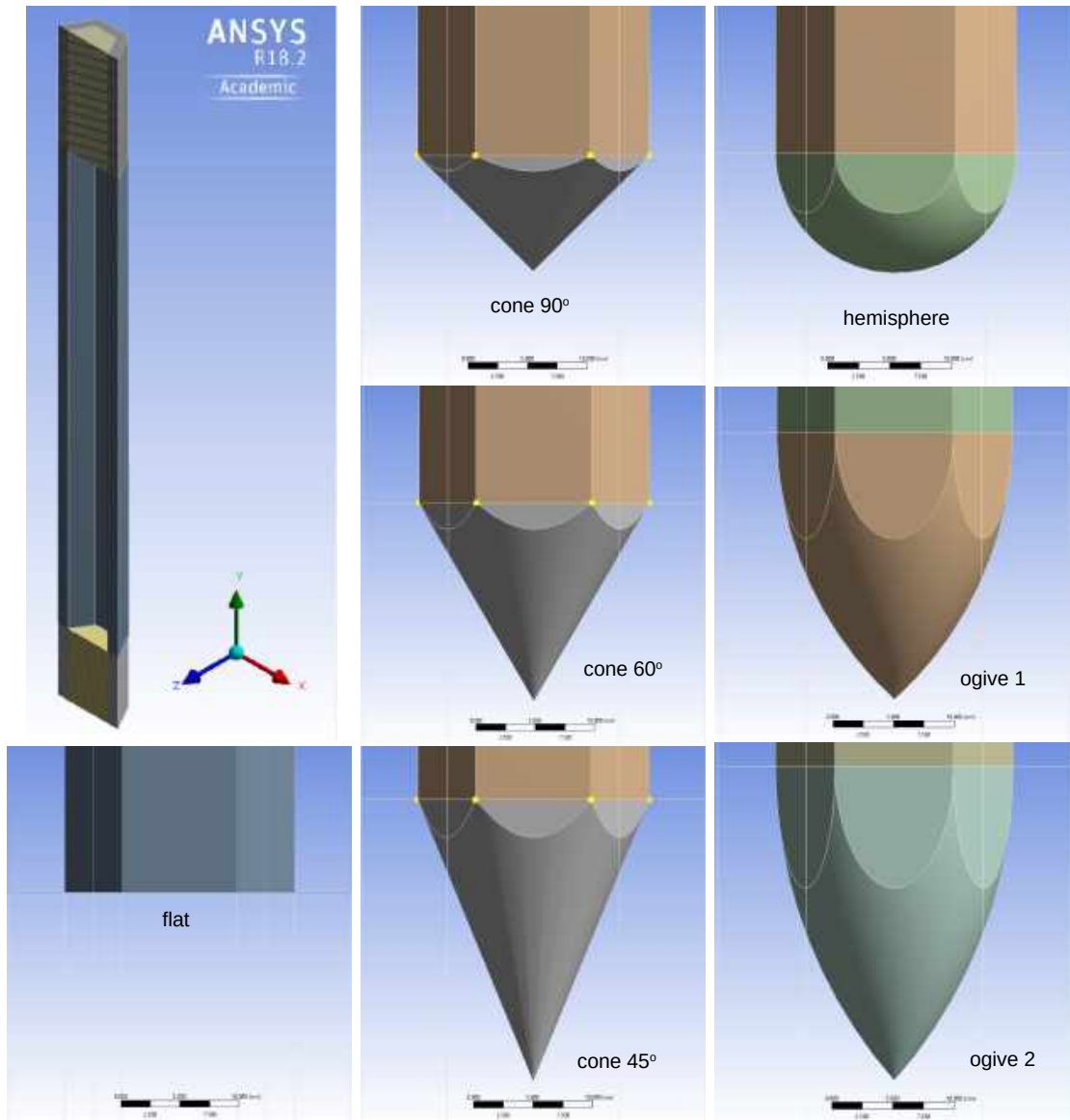


Figure 6.12: Geometry images for different profiles

3D Meshing

The geometry thus created is imported into the ANSYS Mesher, a highly capable meshing software. The tool is capable of meshing complex geometries with the Mosaic Meshing Technology, creating both structured and unstructured meshes. The software also has support for parallel processing that can efficiently build meshes with millions of cells. Our geometry is axisymmetric and not very complicated, and the Academic version is limited to 512,000 elements. As for the first profile it is easy to create a structured mesh with hexahedral prism cells. Other profiles however have curved surfaces, and hence an unstructured mesh was created. The cross section of the meshes are shown in Figure 6.13.

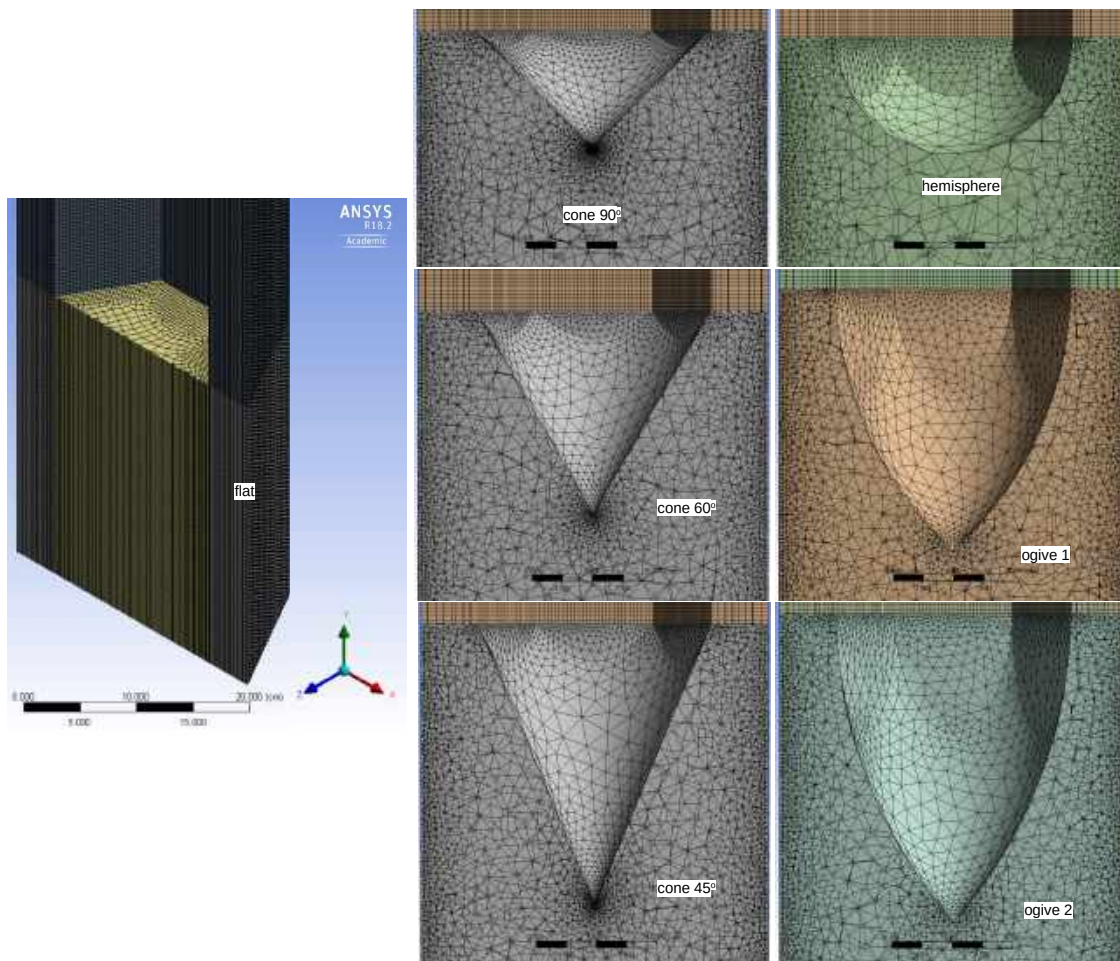


Figure 6.13: Mesh cross section for different profiles

Care was taken to keep the quality of the cells at an appreciable level (>0.1). The statistics of the mesh for different cases is given in Table 6.7. The various faces of the geometry were named accordingly. The entire foot profile was created as one surface and forces are calculated on this face to compute drag coefficient.

Table 6.7: Mesh statistics

Profile	Elements	Min. orthogonal quality	Min. element quality
<i>Case_{flat}</i>	234595	0.37	0.32
<i>Case_{cone90}</i>	213063	0.11	0.19
<i>Case_{cone60}</i>	191873	0.15	0.22
<i>Case_{cone45}</i>	205716	0.17	0.26
<i>Case_{hemi}</i>	192280	0.05	0.07
<i>Case_{ogive1}</i>	198522	0.17	0.26
<i>Case_{ogive2}</i>	245784	0.15	0.21

FLUENT Solver

The mesh is imported to the FLUENT Software to perform actual numerical simulation. The general settings selected in FLUENT are provided in Table 6.8. Static calculations are performed to save time. As a trial, transient simulations were performed in a 2D model to see how the body would passively fall by gravity using the *dynamic meshing* feature in FLUENT. It was realised that transient simulations require large processing capability, and instead static simulations were run to calculate drag coefficients and use the results obtained in a mathematical model. The simulations were performed in a rather old Intel® Core(TM) i5-4210U 4 core CPU running at 1.70GHz. Considerable efforts were taken to optimise both the processes of meshing and simulation.

Table 6.8: FLUENT settings

Solver setting	
Pressure based	
Steady state	
Standard $k - \omega$ turbulence model	
Solution methods	Value
Scheme	SIMPLE
Gradient	Least squares cell based
Pressure	Second order
Momentum	Second order upwind

Appropriate reference values, force and coefficient reports are setup to calculate drag coefficient and drag force. The simulation for each profile is run for different inlet velocities corresponding to the values given in Table 6.6.

6.2.2.2 Results: Drag Coefficients

The drag coefficients obtained from simulations are summarised in Table 6.9 and the plotted results are presented in Figure 6.14. The data is plotted against velocity for simplicity and to extract direct linear relationship.

Table 6.9: Drag coefficients as computed by FLUENT

Reynolds number	$Case_{flat}$	$Case_{cone90}$	$Case_{cone60}$	$Case_{cone45}$
$2.5 * 10^5$	2.199	0.649	0.352	0.258
$5.0 * 10^5$	2.177	0.576	0.331	0.195
$7.5 * 10^5$	2.15	0.543	0.302	0.146
$1.0 * 10^6$	2.11	0.541	0.295	0.156

Reynolds number	$Case_{hemi}$	$Case_{ogive1}$	$Case_{ogive2}$
$2.5 * 10^5$	0.454	0.299	0.278
$5.0 * 10^5$	0.343	0.207	0.207
$7.5 * 10^5$	0.342	0.175	0.172
$1.0 * 10^6$	0.345	0.172	0.163

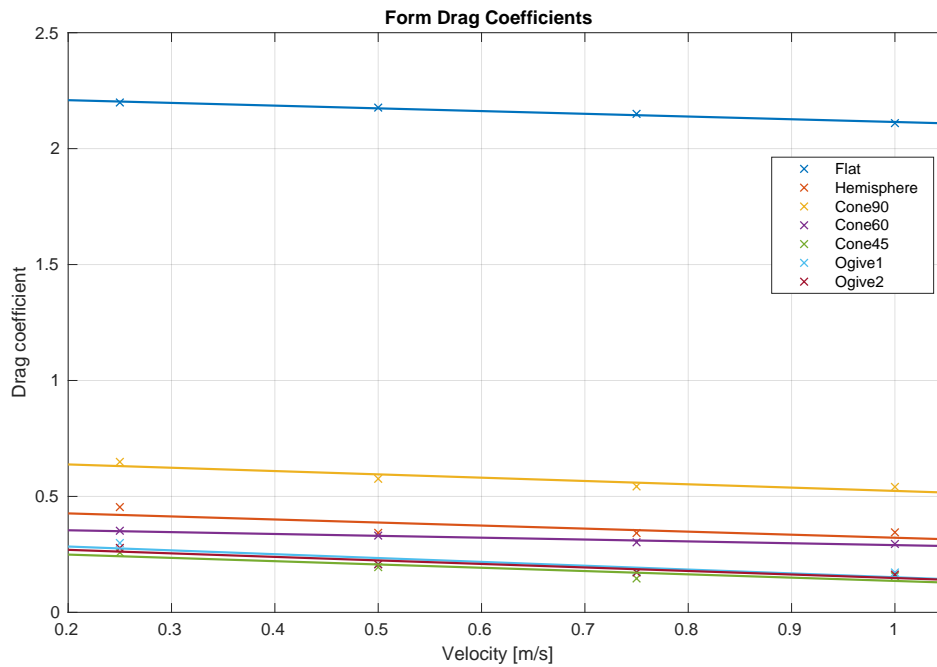


Figure 6.14: Drag coefficients for different profiles

Relying on the above data of the coefficients, one can infer that $case_{cone45}$ has the least drag coefficient among the cases considered followed closely by the two ogive profiles $case_{ogive2}$ and $case_{ogive1}$ while, as predicted, the $case_{flat}$ has the highest of magnitudes, much greater than the what was obtained from the pen and paper calculation. Therefore the profile with the least drag, $case_{cone45}$, is considered to be the final foot profile. Once this was decided, few extra simulations were performed for slightly higher and lower velocities, $0.05m/s$, $0.1m/s$, $0.15m/s$, $1.25m/s$, $1.5m/s$ and $2.0m/s$, and the data was fitted with an exponential function of velocity, shown in Equation 6.19, using the Curve Fitting Tool in MATLAB, the plot of which is shown in Figure 6.15. This equation is used for the C_D in the mathematical modelling of the gravity assisted insertion.

$$C_D = (1.629 \pm 0.399) * e^{(-18.81 \pm 5.14)*v} + (0.2412 \pm 0.0613) * e^{(-0.3825 \pm 0.2542)*v} \quad (6.19)$$

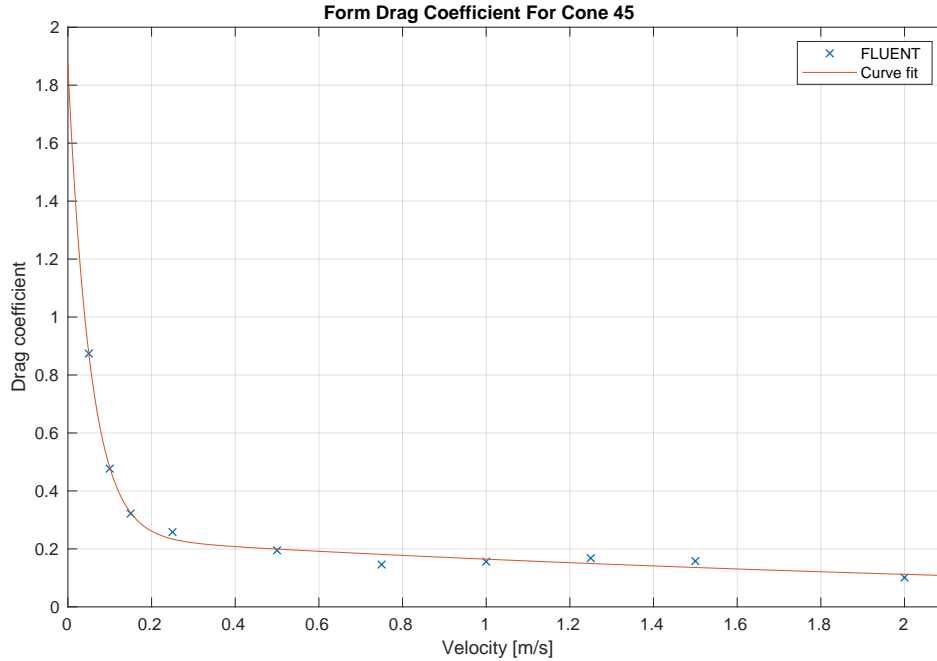


Figure 6.15: Drag coefficients for the 45° cone profile

6.2.3 Mathematical Model

Making use of the data collected and the models created so far, a MATLAB script was developed that can describe the mechanics of the assembly as it free falls. The script discretises time and solves iteratively the distance the assembly travels in each time step (Δt), the force it experiences at each time step and the acceleration at each position by solving the equations discussed here. A graphical representation of the falling body is shown in Figure 6.16. The model is as explained, a wrapper and the absorber rods, now including the assembly foot. The skin friction is assumed to act only on the outer faces of the wrapper, considering the faces as flat plates, while form drag acts on the foot profile. Inside the assembly the coolant is assumed to be stagnant with no flow, thereby simplifying the calculation. It was discussed previously that the coolant is differentiated into 3 regions

- UP - constant temperature/buoyancy
- MID - or the AZ section with varying temperature/buoyancy and
- LOW - constant temperature

The script is designed in a similar fashion, it solves first the set of equations until the assembly reaches the end of UP region, then the MID section and finally the LOW region. While the buoyancy is constant in UP section, once the assembly starts entering the MID region, corresponding to each step, the volume equivalent, $A_{hex+rods} * \Delta s$, is used to add to the buoyancy, while simultaneously subtracting the same volume equivalent of the buoyancy from the UP section.

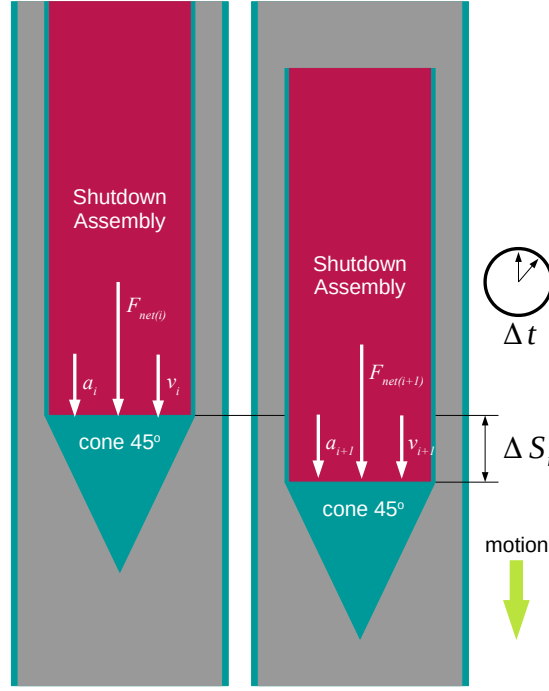


Figure 6.16: Graphical representation of the fall

Initial conditions are set, the initial forces acting are computed and consequently the initial acceleration of the assembly. It should be noted here that the volume of the foot V_{foot} adds to the displaced volume V_{disp} . The equivalent weight of the foot F_{foot} , considering that it is made of a particular *ferritic steel* such as *FeCrAl* with a density ρ_{foot} , is added to $F_{gravity}$ and the equivalent mass m_{foot} to total mass M_{tot} 6.6. The drag forces are calculated for the initial condition, considering a coolant velocity v_{cool} , and using the fitted equation for the form drag coefficient 6.19 and skin friction for the plate, 6.14 or 6.16. Using these initial forces of gravity, buoyancy and drag, the initial net force F_{net0} is computed using Equation 6.2. Once the net force is calculated, the initial acceleration is computed using Equation 6.20. This is obtained by linearising, for the time step, the differential expression for the force as given in Equation 6.1.

$$a_0 = \frac{F_{net0}}{M_{tot}} \quad , \quad a_i = \frac{F_{neti}}{M_{tot}} \quad (6.20)$$

The velocity at the end of time step is calculated using Equation 6.21

$$v_1 = v_0 + a_0 * \Delta t \quad , \quad v_i = v_{i-1} + a_{i-1} * \Delta t \quad (6.21)$$

Having calculated the velocity, the distance the assembly travels in the time step is given in Equation 6.22

$$\Delta S_1 = v_0 * \Delta t + \frac{a_0 * (\Delta t)^2}{2} \quad , \quad \Delta S_i = v_{i-1} * \Delta t + \frac{a_{i-1} * (\Delta t)^2}{2} \quad (6.22)$$

The total distance travelled after each step (S_i) is recorded and checked if the UP region is exceeded. Once it has exceeded and enters the MID region, a different set of equations solve for the buoyancy, while the other forces are calculated as previously

stated. In the MID section density of lead varies as given in Figure 6.5. So for each elemental volume increase in the MID section, the buoyancy starts increasing, correspondingly the buoyancy in the UP section reduces.

The calculations are repeated, constantly checking if the LOW section is reached, and once it has, the method to calculate buoyancy changes again. For elemental change in volume, buoyancy equivalent to the density of lead at inlet temperature is added, while the same at outlet temperature is removed. Subsequently the total distance of travel of the assembly attains designated value, equal to the length of the fuel rod. The flowchart of the above steps is presented in Figure 6.17.

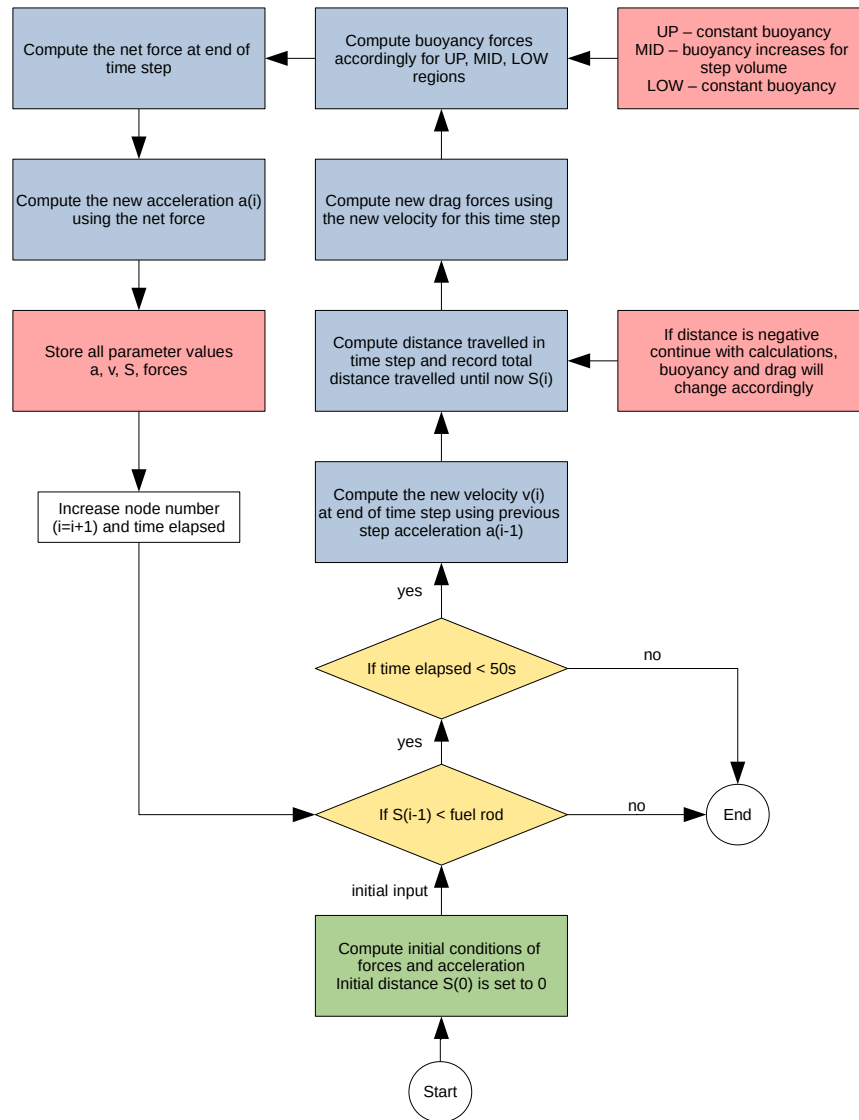


Figure 6.17: Calculation scheme for the 1D gravity driven insertion analysis

The above calculations, especially the force balance, is determined by an assumption that the assembly is inserted downwards, that is the velocity in downward direction is positive. However it may so happen that at some instant the upward forces overpower the downward forces, thus decelerating and subsequently exerting negative velocity. Under such conditions the script will account for negative velocities by being extracted rather than inserted in the channel.

6.2.4 Results

6.2.4.1 Gravity Insertion Mechanics

The results from the first set of calculations are presented here. The coolant velocity and the minimum density of the foot material considered to effectively shutdown is given as follows.

$$v_{cool} = 0.84m/s \quad , \quad \rho_{foot} = 8250kg/m^3$$

Figure 6.18 shows the variation of velocity and acceleration of the assembly. Figure 6.19a, 6.19b and 6.19c shows the forces exerted on the assembly along the path of insertion. The velocity reaches a maximum as it initially has higher acceleration, but then starts falling as the drag forces increases, 6.19c. The acceleration is positive over some distance but later starts decelerating as the total upward force due to drag and buoyancy 6.19b surpasses the downward gravity. The deceleration, subsequently slows the assembly to approximately $0.05m/s$ at the end of the insertion length. The buoyancy forces, as shown, is constant in the UP region, then starts increasing continuously in the MID and LOW sections. The total time of insertion of the shutdown assembly is

$$t_{insertion} = 17.297s$$

This is higher than our initial objective of limiting time of insertion under 10s. During trial calculations two major factors were discovered to impact time of insertion, namely the density of assembly foot material (signifying net downward force due to gravity) and the coolant velocity (signifying drag forces). In order to grasp their effect sensitivity analysis was performed.

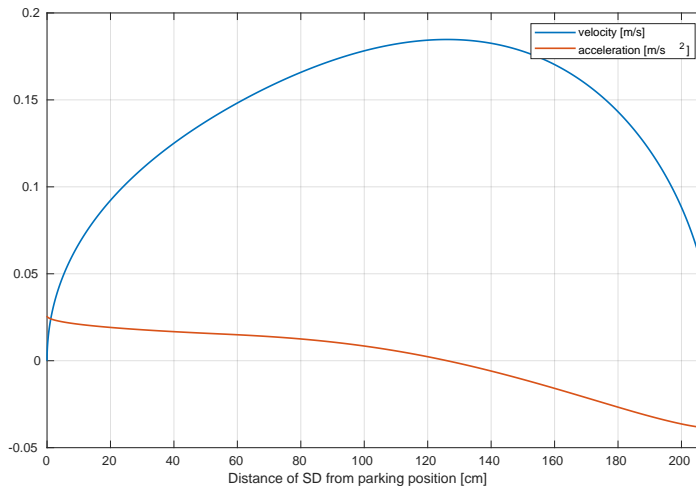
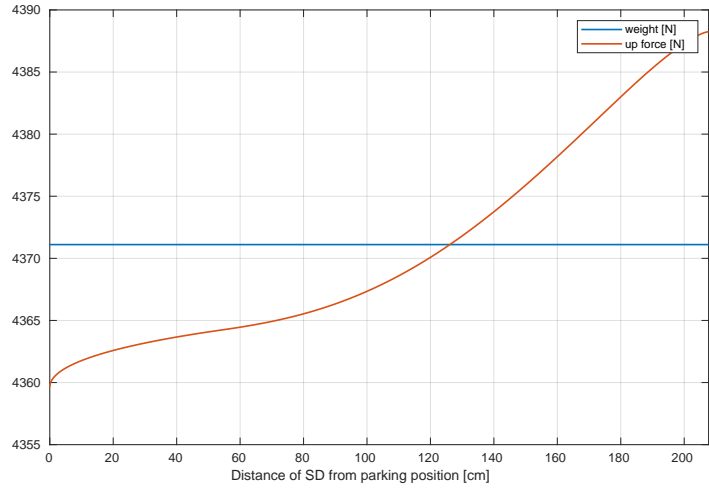
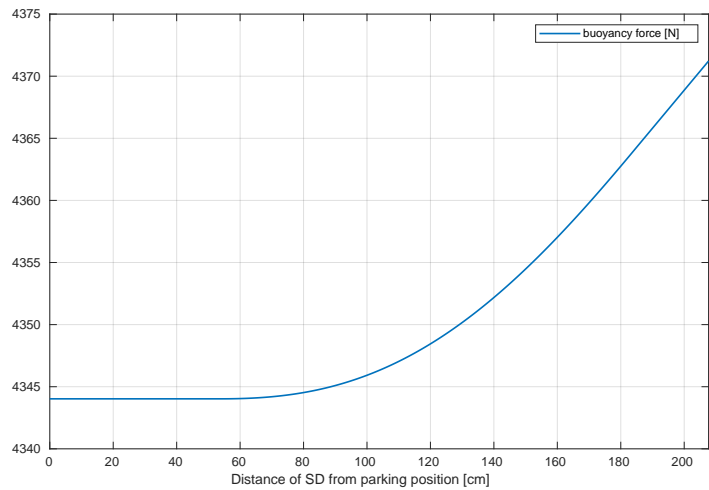


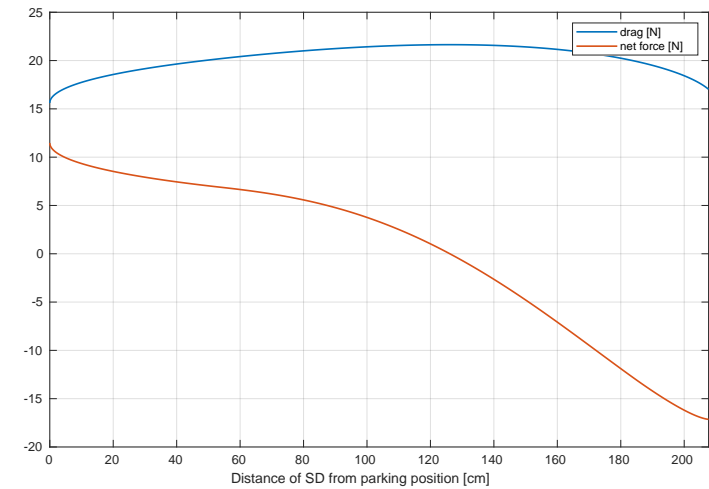
Figure 6.18: Variation of velocity and acceleration of the assembly



(a) Variation of net upward forces and the weight of the assembly



(b) Variation of net upward forces and the weight of the assembly



(c) Variation of drag and total force of the assembly

Figure 6.19: Variation of forces on the shutdown assembly

6.2.4.2 Sensitivity Analysis for Foot Density

As it was mentioned earlier, the net force acting on the assembly is driven by gravity. Increasing downward force will increase net force and thereby shorten insertion period. SEALER reactor is proposed to not include tungsten ballast to facilitate easy insertion. However, the calculations done here reveal that it might be necessary. To see how it affects, the following arbitrary densities were simulated in the code. The arbitrary densities can be effectively converted to weight equivalent of tungsten, by filing the *space* inside the foot with sets of weight. The distance against time plots for these densities is presented in Figure 6.20. Tungsten densities vary depending on the atomic fraction of additives such as copper or nickel. Pure tungsten has a density of 19300kg/m^3 at room temperature, with the ballast densities varying from 17100kg/m^3 - 18500kg/m^3 for tungsten fractions of 90-97% [75]. Here we consider the upper density limit at 19000kg/m^3

Density [kg/m^3]	8250	8300	8500	9500	10000	12500	15000	17500	19000
Mass [kg]	12.14	12.21	12.51	13.98	14.71	18.39	22.07	25.75	27.96

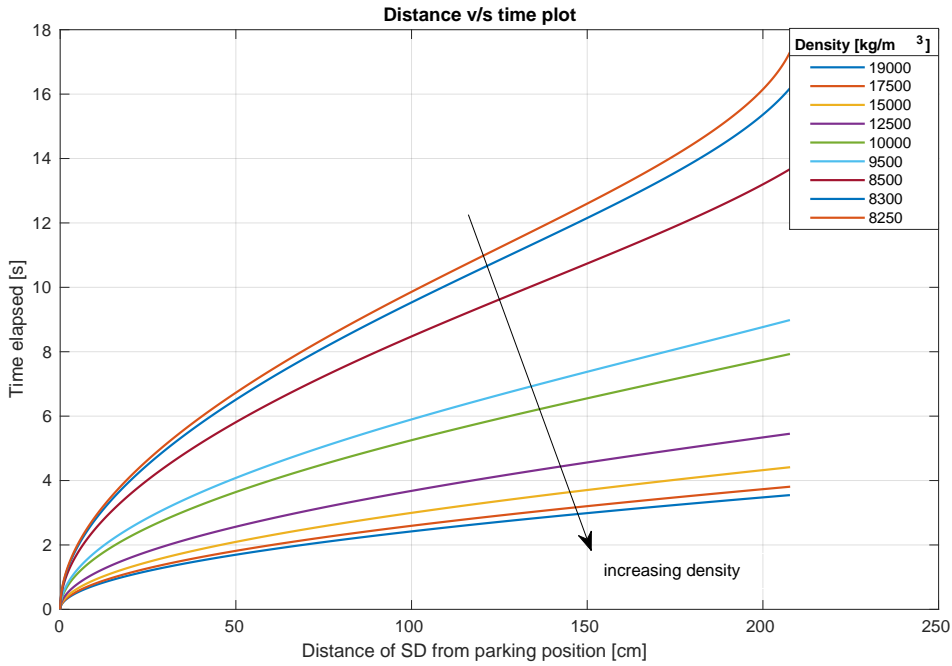


Figure 6.20: Variation of distance with time for different densities of assembly foot

The times of insertion for these densities is provided in Table 6.10. A remarkable reduction in insertion period is evident by increasing the density. Figure 6.21 graphically represents this variation and a two factor exponential trend was fit to the data as given in Equation 6.23.

$$t_{insertion} = (3.4 \pm 22.1) * 10^6 e^{(-15.62 \pm 8.04) * 10^{-4} * \rho_{foot}} + (17.13 \pm 8.18) * e^{(-8.69 \pm 3.28) * 10^{-5} * \rho_{foot}} \quad (6.23)$$

Table 6.10: Times of insertion for different densities of assembly foot

Density [g/cm ³]	8.25	8.30	8.50	9.50	10.00	12.50	15.00	17.50	19.00
Time [s]	17.297	16.179	13.669	8.984	7.929	5.454	4.413	3.808	3.548

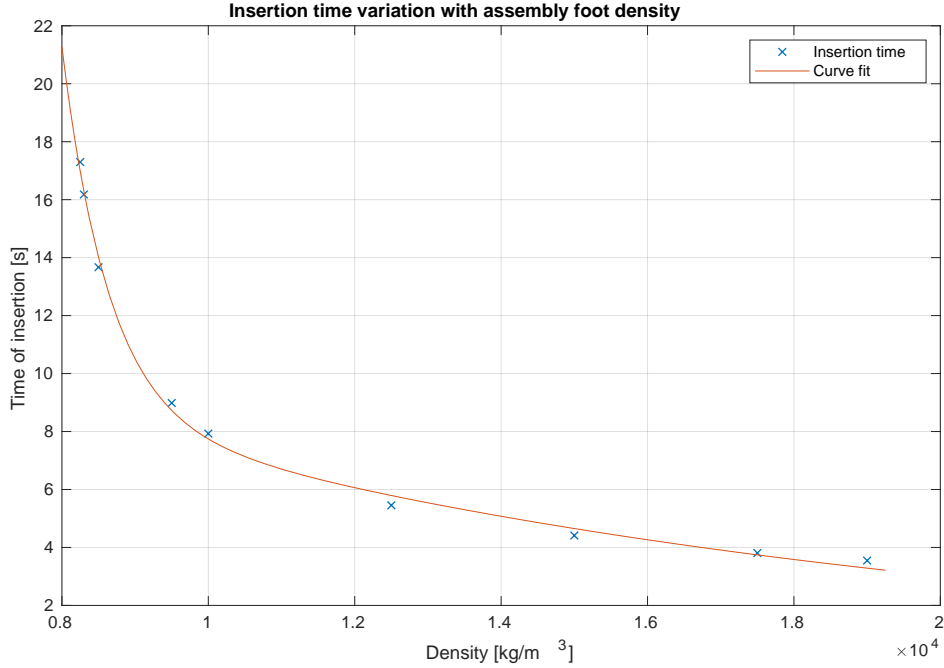


Figure 6.21: Variation of time of insertion with assembly foot density

To agree with our objective of keeping the time of insertion close to 10s, a density of $9000\text{kg}/\text{m}^3$ is selected that gives

$$t_{insertion} = 10.609\text{s}$$

6.2.4.3 Sensitivity Analysis for Coolant Velocity

The velocity of the impinging coolant is a sensitive parameter that affects drag contribution to the net force. The assembly velocity distribution in the core is given in Figure 6.22. The coolant velocity is derived from the assembly-wise power distribution determined during the neutronic analysis, shown in Figure 5.17. The differential coolant flow in assemblies is necessary to maintain a constant core outlet temperature. A simple heat balance to the heat generated by the assembly and the heat carried by the coolant can be given as in Equation 6.24. Here $\dot{m}_{assembly}$ is the mass flow rate (kg/s) of the coolant in the assembly and c_{ppb} is the specific heat capacity of the coolant ($\text{J}/\text{kg}/\text{K}$) which is a function of temperature³. The integral is a constant since we intend to keep constant temperatures at inlet $T_{in} = 420^\circ\text{C}$ and $T_{out} = 550^\circ\text{C}$. The velocity is calculated using the mass equation 6.25, where

³See Appendix A for the correlation

A_{free} is the channel area inside the outer wrapper and $\rho_{pb_{mean}}$ is the mean coolant density in the channel.

$$P_{assembly} = \dot{m}_{assembly} \int_{T_{in}}^{T_{out}} c_{p_{pb}} dT \quad (6.24)$$

$$\dot{m}_{assembly} = \rho_{pb_{mean}} * A_{free} * v_{assembly} \quad (6.25)$$

Coolant velocity distribution in assemblies of critical core at MoL

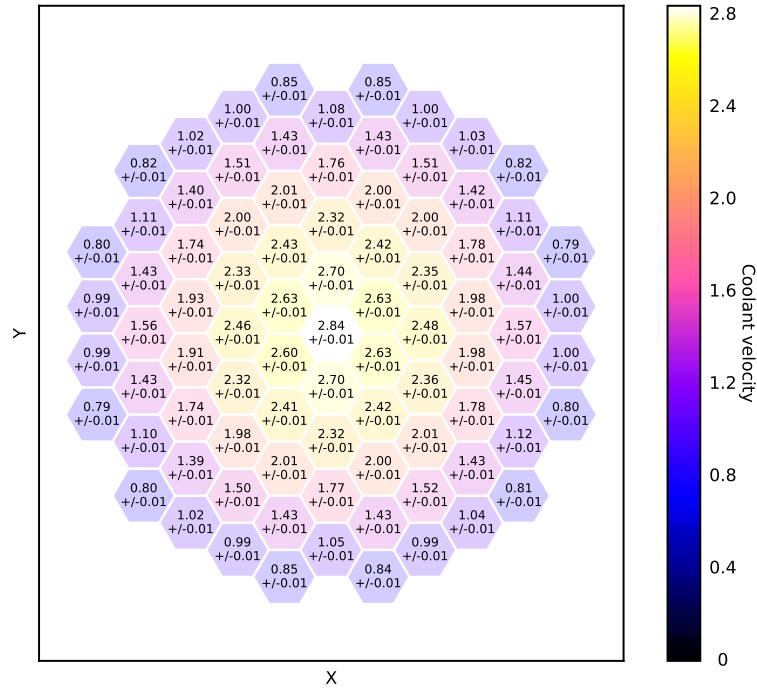


Figure 6.22: Assembly wise coolant velocity distribution

Consequently, the coolant velocities are highest in the central assemblies and fall towards the corners. It is considered that the flow is able to bypass through the orifices in the assembly foot in the lower plenum, however due to lack of exact information, the simulations were run considering that the nominal coolant velocity is similar to the overall average of the coolant velocities in the assemblies adjacent to the control assembly channels in the outermost ring

$$v_{cool} = 0.84m/s$$

In order to see how sensitive the coolant velocity is to the time of insertion, the following velocities were considered in the sensitivity analysis. Figure 6.23 presents the results obtained for the distance travelled versus time elapsed for these coolant velocities, while the times of insertion for these cases is provided in Table 6.11.

Flow [%]	100	75	50	25	10	5	1	0
Coolant velocity [m/s]	0.84	0.63	0.42	0.21	0.084	0.042	0.0084	0

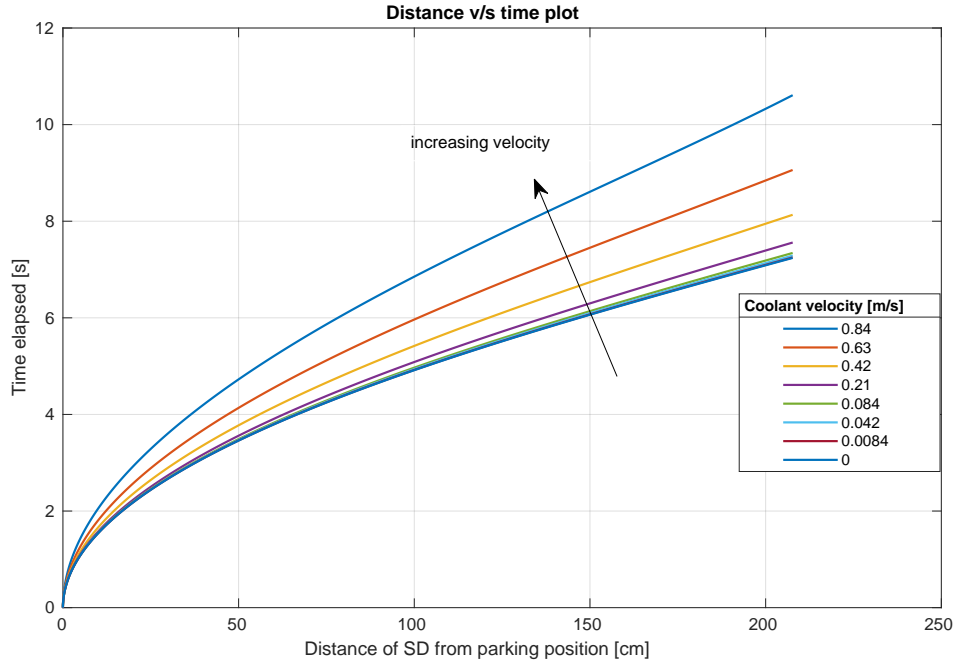


Figure 6.23: Variation of distance with time for different assembly coolant velocity

Table 6.11: Times of insertion for different assembly coolant velocity

Velocity [m/s]	0.84	0.63	0.42	0.21	0.084	0.042	0.0084	0
Time [s]	10.609	9.061	8.133	7.559	7.343	7.289	7.249	7.240

Figure 6.24 graphically represents this variation and a two factor exponential was fit to the data as given in Equation 6.26.

$$t_{insertion} = (6.581 \pm 0.238)e^{(-0.04925 \pm 0.07433)*v_{cool}} + (0.6565 \pm 0.2423) * e^{(2.236 \pm 0.269)*v_{cool}} \quad (6.26)$$

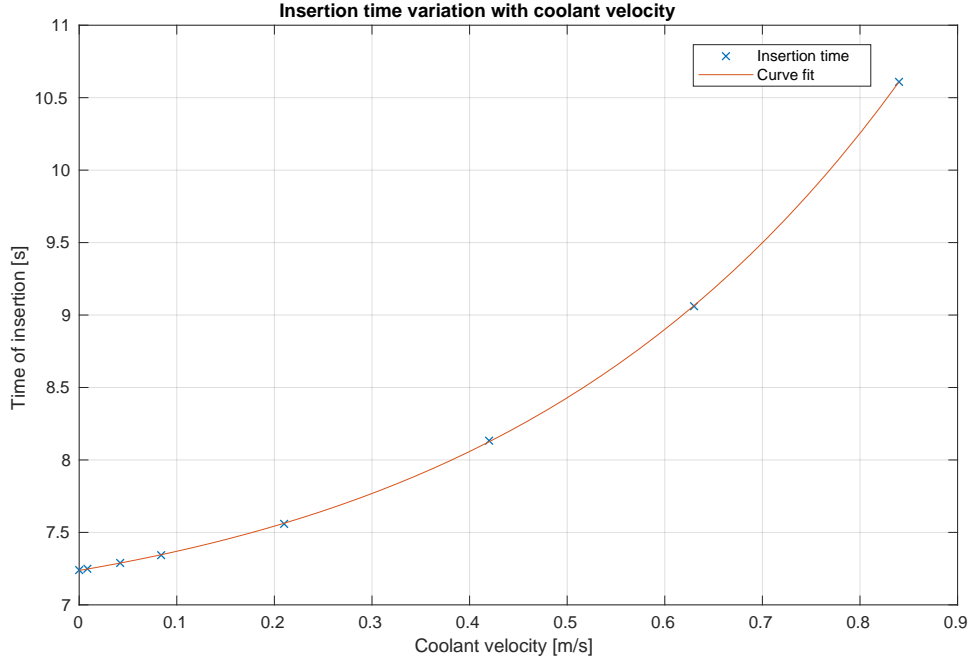


Figure 6.24: Variation of time of insertion with coolant velocity

6.2.4.4 Sensitivity Analysis for Average Form Drag Coefficient

It was mentioned that from the preliminary pen and paper calculations, that the limiting drag coefficient is about $C_D = 0.458$. Now, having developed the code to compute the mechanics of the passive insertion, one can find the drag coefficient of a foot profile that can successfully insert the gravity driven shutdown system. Now we have already discussed that the coefficient varies with Reynolds number, but for the sake of simplicity, averaged form drag coefficients are considered. The different cases that were initially designed, see Table 6.9, is considered in this sensitivity analysis, by taking their average C_D . Some additional arbitrary coefficients were also considered, that shows particularly interesting results, for a maximum coolant velocity of 0.84m/s . Figure 6.25 presents the distance covered against time plots for each of these cases, and Table 6.12 summarises the results. It is to be mentioned that the other case, namely *case_{flat}* is not included because the profile is not able to achieve shutdown.

Case	<i>case_{cone45}</i>	<i>case_{ogive2}</i>	<i>case_{ogive1}</i>	<i>case_{0.25}</i>	<i>case_{0.258}</i>
C_D	Eq. 6.19	0.205	0.211	0.25	0.258
Case	<i>case_{cone60}</i>	<i>case_{hemi}</i>	<i>case_{0.39}</i>	<i>case_{0.41}</i>	<i>case_{0.42}</i>
C_D	0.32	0.371	0.39	0.41	0.42

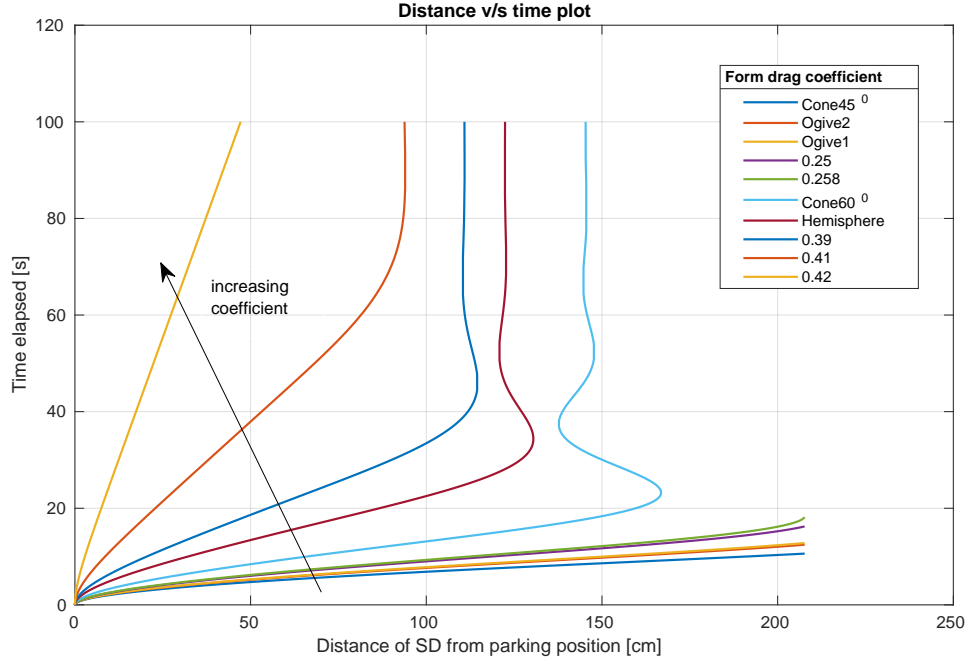
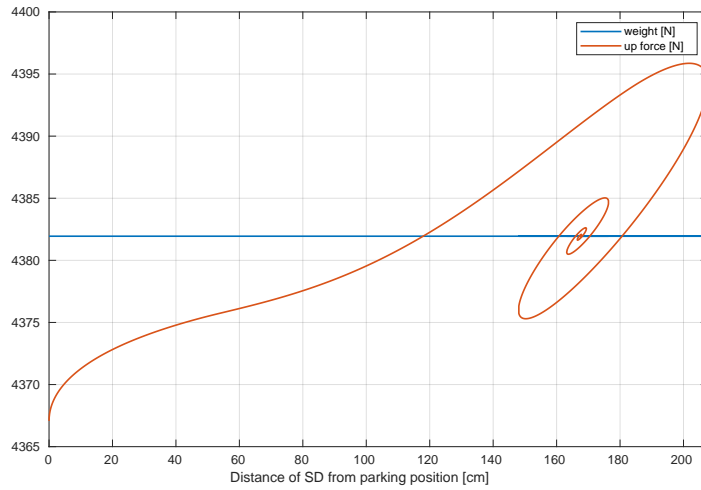


Figure 6.25: Variation of distance with time for different form drag coefficients

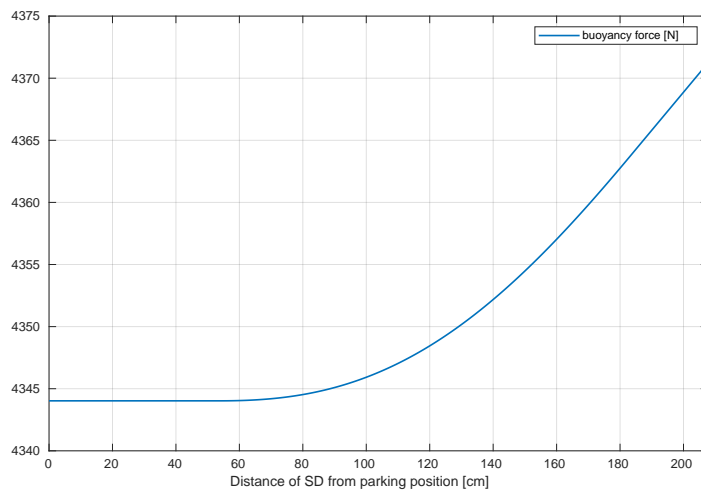
Table 6.12: Times of insertion for different drag coefficient cases

Case	Max. insertion[cm]	Final insertion[cm]	Time [s]
$case_{cone45}$	207.6687	207.6687	10.609
$case_{ogive2}$	207.6687	207.6687	12.451
$case_{ogive1}$	207.6687	207.6687	12.796
$case_{0.25}$	207.6687	207.6687	16.236
$case_{0.258}$	207.6687	207.6687	18.159
$case_{cone60}$	166.8359	145.3506	∞
$case_{hemi}$	130.4844	122.4181	∞
$case_{0.39}$	114.6213	110.8575	∞
$case_{0.41}$	94.0269	93.8094	∞
$case_{0.42}$	78.5757	78.5767	∞

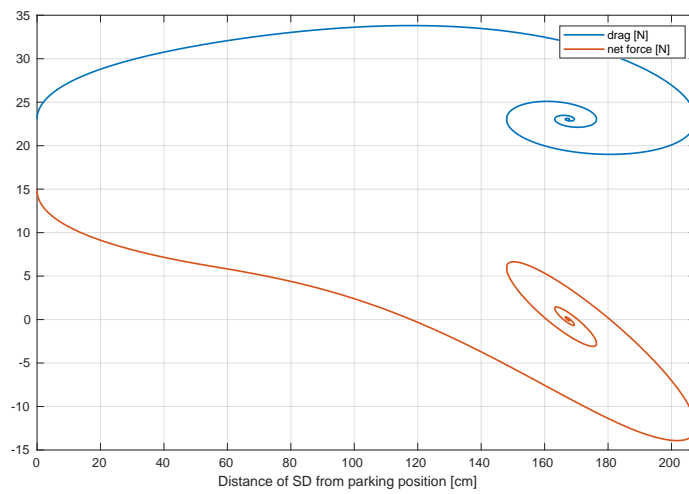
It is seen how increasing the drag increases times of insertion for low drag bodies. For profiles with C_D greater than, roughly 0.258, the assembly does not shutdown. Any profile with average form drag above this value fails to completely insert, but rather it is *hydrodynamically suspended* against the coolant flow. The wavy pattern is due to this exact phenomenon where the constantly decelerating assembly achieves negative velocities, thereby being extracted rather than inserted. Consequently the forces try to battle each other, resulting in the oscillations which eventually halts any motion and the assembly is suspended. To present the forces acting for such profiles, a profile with C_D slightly larger than 0.258 is considered, $case_{0.25825}$. At this coefficient the assembly barely manages to reach the bottom of the core. The maximum depth it reaches from the parking position is 207.6488cm where from it oscillates and finally reaches a stable position at a depth of 162.3918cm. Figures 6.26a, 6.26b and 6.26c shows how the forces behave as the assembly falls.



(a) Variation of net upward forces and the weight of the assembly



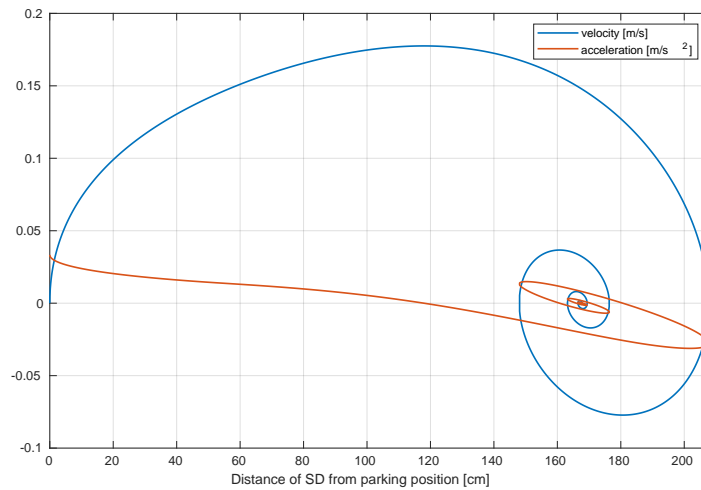
(b) Variation of net upward forces and the weight of the assembly



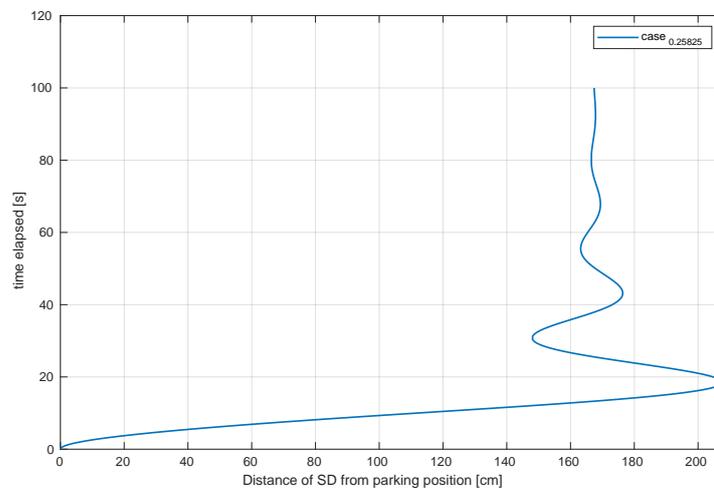
(c) Variation of drag and total force of the assembly

Figure 6.26: Variation of forces on the shutdown assembly

Figure 6.27a and 6.27b show how the velocity and acceleration evolve along the insertion path. As the assembly falls the drag force and buoyancy starts increasing, which consequently brings the acceleration to zero. Here the velocity and drag forces reach a maxima, whilst net force reaches a zero. But since the assembly has the momentum it collected from the fall, the inertia pushes against the coolant while the net force starts increasing in negative direction. This is where the velocity and drag force starts reducing, as the relative velocity between the coolant and the assembly starts reducing. The deceleration happens until the the assembly just reaches the bottom of the channel. At this position however, the buoyancy which has reached a maximum exerts the maximum net upward force, which starts retracting the assembly, whereby buoyancy starts reducing. Consequently, drag force reduces even further, because of reducing relative velocity between the coolant and the assembly. The tug of war between the forces of buoyancy and drag continue until they balance each other, at a depth of 162.3918cm . Hence, for the selected conditions the limiting drag coefficient C_D is 0.258.



(a) Variation of velocity and acceleration of the assembly



(b) Time elapsed against position in the channel

Figure 6.27: Variation of velocity and acceleration of the shutdown assembly

6.3 Buoyancy Driven Insertion Model

The buoyancy insertion system was considered as an alternative to the gravity driven insertion, in case it was found that the latter would not be able to achieve shutdown. It was shown that passive insertion by gravity is possible quite effectively in 10s. The following discussion is based solely keeping the consistency of study in focus. In a lead environment, it is effective to achieve buoyancy driven insertion, than gravity driven insertion. Conventional boron carbide is the preferred absorber in this case. One can see that, neutronicly the reactivity worth is similar between the B_4C absorber and $WReB_2$ absorber in CR and SD bank respectively, see Table 5.4. So it is considered in this study that a shutdown assembly driven by buoyancy is designed similar to the control assembly 5.9. The model has 19 absorber rods in place of 7 rods in the $WReB_2$ assembly, dimensions of which are provided in Table 6.13, while the other dimensions of the inner wrapper, the total length and the outer wrapper is the same as in Table 6.3.

Table 6.13: Dimensions of the assembly parameters

Property	Value	Unit
Absorber rod	19 B_4C	
Pellet diameter d_{p_o}	0.02797	m
Clad inner diameter d_{C_i}	0.02870	m
Clad outer diameter d_{C_o}	0.03189	m

The density of B_4C is $2250kg/m^3$. The relevant cross sectional area of the model is presented in Table 6.14. The displaced volume in the assembly is $V_{disp} = 0.03675322m^3$, excluding the foot (or in this case the head V_{head}) volume.

Table 6.14: Areas of interest

Parameter	Area [m^2]
$A_{projected}$	0.0241525
$A_{surface}$	1.3074212
$A_{hex+rods}$	0.0016262
A_{free}	0.0312493
$A_{annulus}$	0.0069653

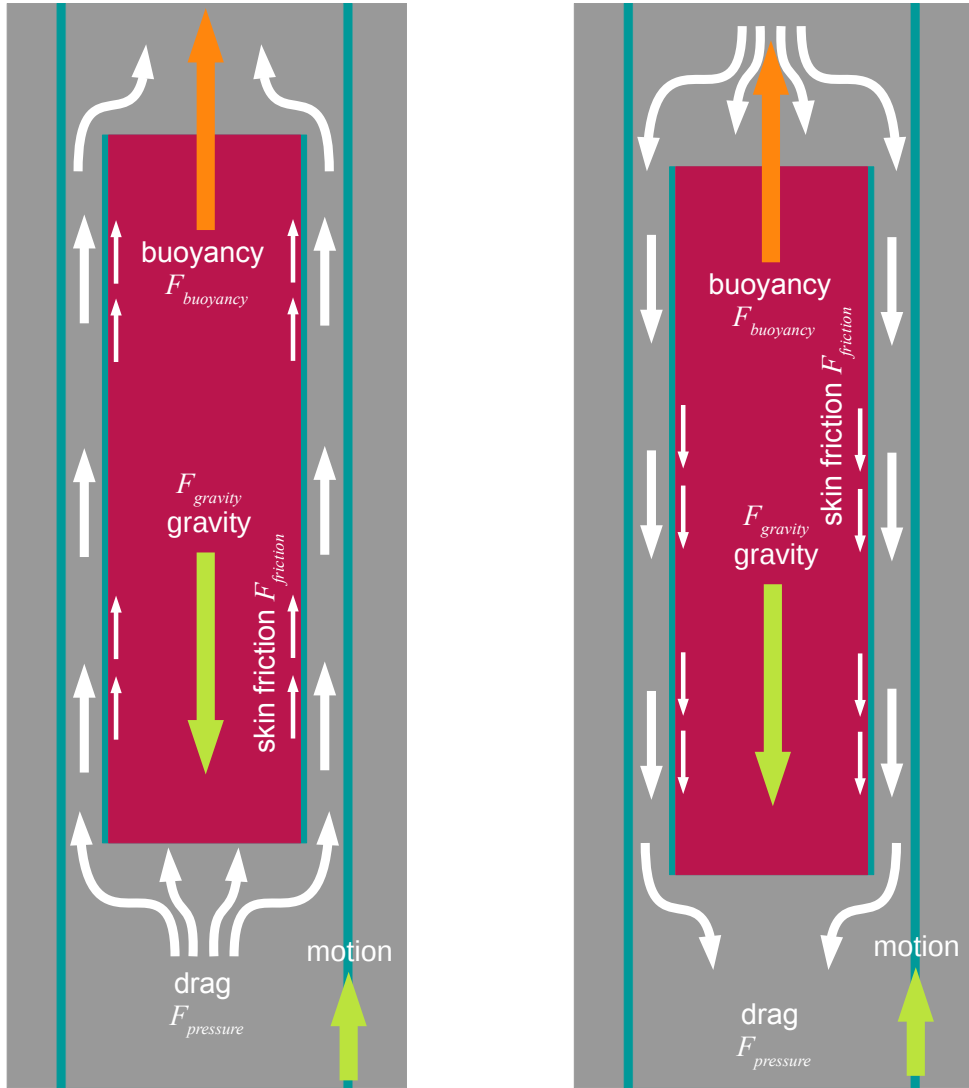
6.3.1 Underlying Physics

The physics of the model is very similar to the gravity driven case. The same three forces are considered, gravity, buoyancy and the drag forces. In this case buoyancy is the driving force, while gravity is the resisting force. The force balance in this case is given as Equation 6.27.

$$F_{net} \uparrow = F_{buoyancy} \uparrow - F_{gravity} \downarrow \pm F_{drag} \updownarrow \quad (6.27)$$

The drag in this case is peculiar. If the model considers a constant coolant flow then initially, when the assembly rise starts, the coolant velocity v_{cool} dominates.

The drag forces, both pressure drag and the skin friction drag, helps in accelerating the assembly. Thus in the case when v of assembly is $< v_{cool}$, the drag adds to buoyancy, that is to the upward forces. Once the assembly overtakes the coolant velocity, the drag acts as usual to oppose the movement of assembly. The two cases are graphically shown in Figure 6.28a and 6.28b.



(a) Various forces acting on the body when $v_{cool} > v$ (b) Various forces acting on the body when $v_{cool} < v$

Figure 6.28: Various forces acting on the body for the two cases

6.3.2 Results

6.3.2.1 Buoyancy Insertion Mechanics

The calculations are made in a similar fashion as gravity insertion model. For consistency the nominal case is considered to be

$$v_{cool} = 0.84m/s \quad , \quad \rho_{head} = 9000kg/m^3$$

This $case_{cone45}$ considered, is assumed to make profile both at the head of the

assembly and feet, because the pressure drag is assumed to act from the bottom and on the upper face. The nominal time of insertion as computed by the code is

$$t_{insertion} = 0.501s$$

This is a very fast insertion, where the proper variations of the forces cant be resolved when plotted. In order to better understand the mechanics, a bigger drag coefficient of 50 is considered to explain the forces. Figure 6.29 shows the variation of velocity and acceleration of the assembly. Figure 6.30a, 6.30b and 6.30c shows the forces exerted on the assembly along the path of insertion. The time of insertion for this case is

$$t_{insertion} = 1.4409s$$

The total upward force first sees a dip and then recovers, this is because of the drag force, which initially acting from below, increases the assembly velocity, which reduces the relative velocity between the coolant and the assembly, which in turn affects the drag. Once the velocity of the assembly overtakes the coolant flow, the drag force starts increasing. Correspondingly, the buoyancy forces continuously decreases, because the insertion starts from LOW section, a high density section, to MID section, a varying density section and finally into UP section a very low density section, results in buoyancy decrease. The drag forces are seen to saturate after some distance. This is attributed to the attainment of *terminal velocity* by the assembly, when the net force acting on the body reaches zero. Indeed, the total force, is seen to quickly dip to zero from a high of approximately $7000N$, implying the balance of forces takes place in small time. Correspondingly the acceleration, at a high of $50m/s^2$ quickly drops to a value close to zero, and the velocity is seen to stagnate at the terminal velocity. Indeed the buoyancy insertion is similar to free fall of a feather in atmosphere, only the directions are reversed. The same phenomenon was not visible in the gravity insertion, because the drag and buoyancy were neck to neck and the body could not attain a sufficient velocity to sustain a terminal velocity. Whilst in this case of buoyancy driven insertion, the buoyancy force single-handedly dominates the other forces.

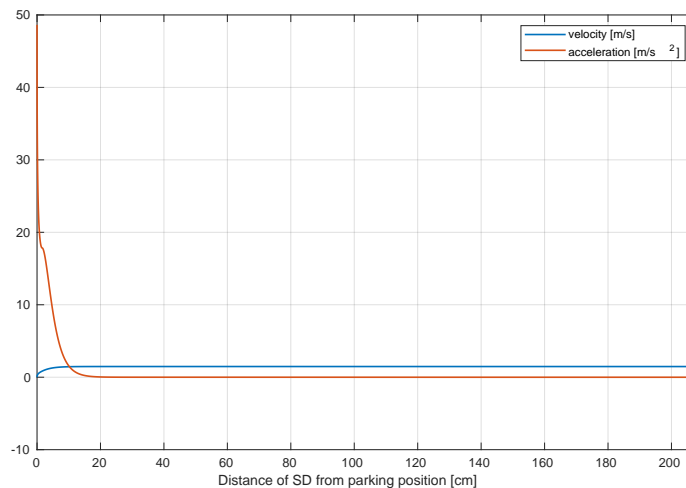
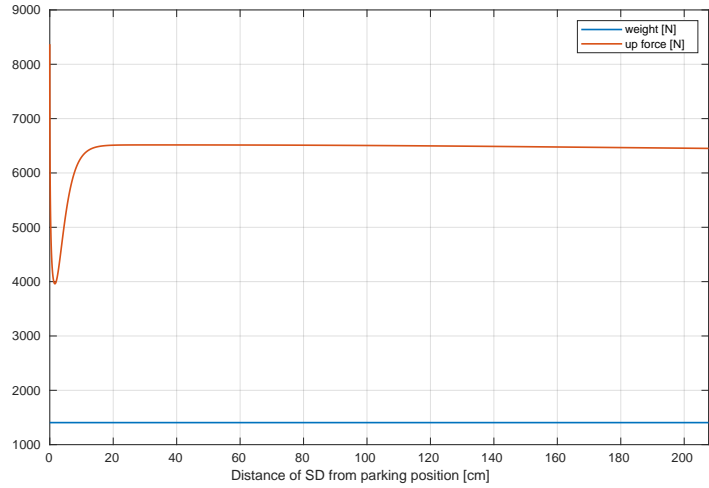
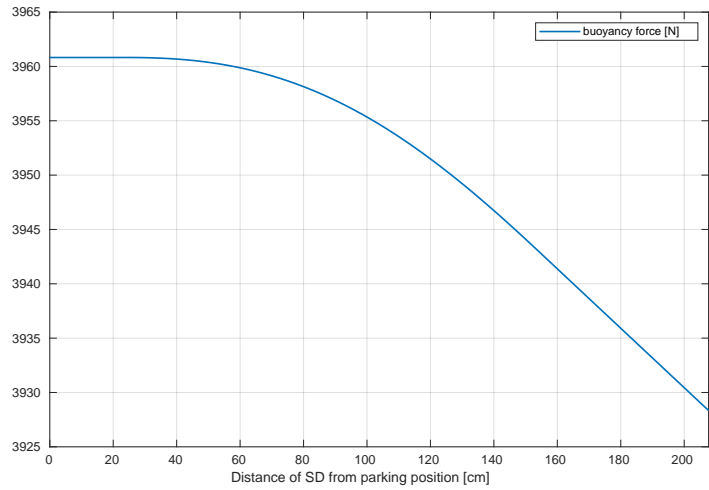


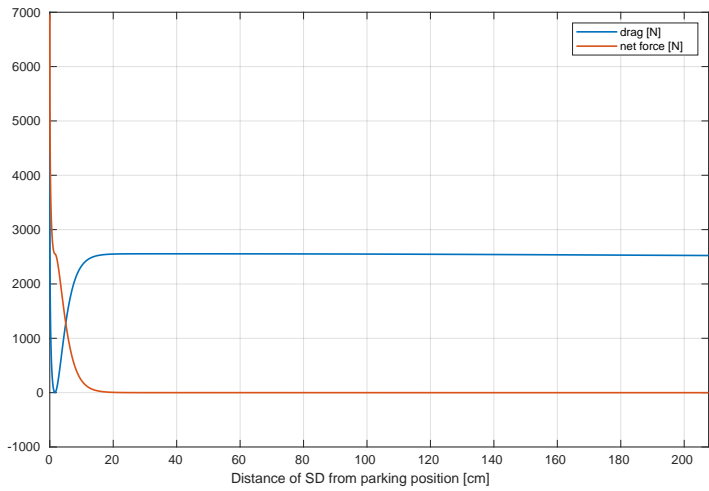
Figure 6.29: Variation of velocity and acceleration of the assembly



(a) Variation of net upward forces and the weight of the assembly



(b) Variation of buoyancy forces of the assembly



(c) Variation of drag and total force of the assembly

Figure 6.30: Variation of forces on the shutdown assembly

6.3.2.2 Sensitivity Analysis for Head/Foot Density

The sensitivity analysis here is done to see if addition of weight has any appreciable change to time of insertion. Unlike the previous insertion method, theoretically no ballast is required for buoyancy assisted insertion, in fact additional weight is detriment. Since the material of the foot and head considered to withstand the neutron flux in the core, it is assumed to be made of *ferritic steels*. So the following densities are arbitrarily considered, shown in Table 6.15, including the *FeCrAl* steel at 7170kg/m^3 . Figure 6.31 presents the results for distance versus time curves for the different cases.

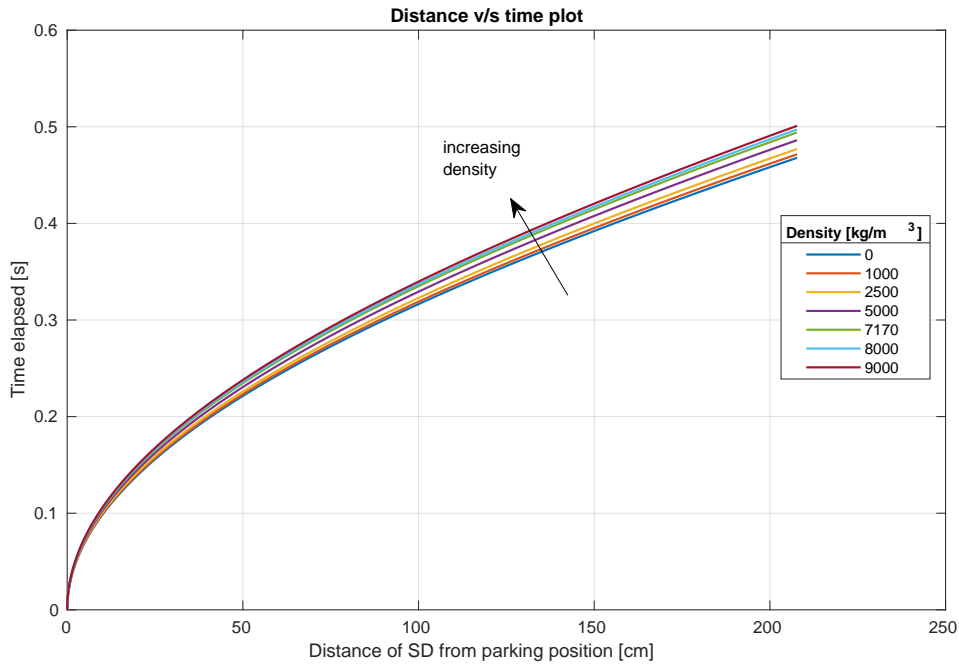


Figure 6.31: Variation of distance with time for different densities of assembly head/foot

The times of insertion for these densities is provided in Table 6.15. Unlike the same sensitivity analysis in the previous method, Not very appreciable change is seen, nevertheless, the increasing the density is seen to increase time of insertion.

Table 6.15: Times of insertion for different densities of assembly head/foot

Density [kg/m^3]	0	1000	2500	5000	7170	8000	9000
Time [s]	0.4679	0.4715	0.477	0.4861	0.4941	0.4972	0.501

Figure 6.32 graphically represents this variation and a linear trend was fit to the data as given in Equation 6.28.

$$t_{insertion} = (3.672 \pm 0.002) * 10^{-6} * \rho_{head} + (0.4678 \pm 0.0002) \quad (6.28)$$

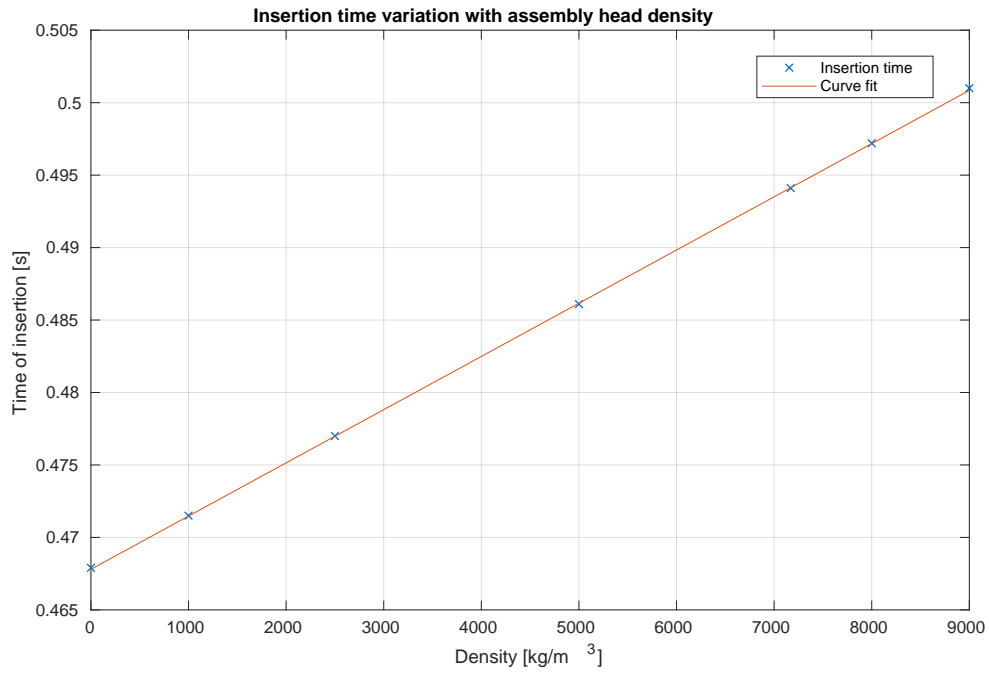


Figure 6.32: Variation of time of insertion with assembly head/foot density

6.3.2.3 Sensitivity Analysis for Coolant Velocity

In a way similar to the previous insertion method, a coolant sensitivity analysis is performed to determine the effect of coolant velocity on time of insertion.

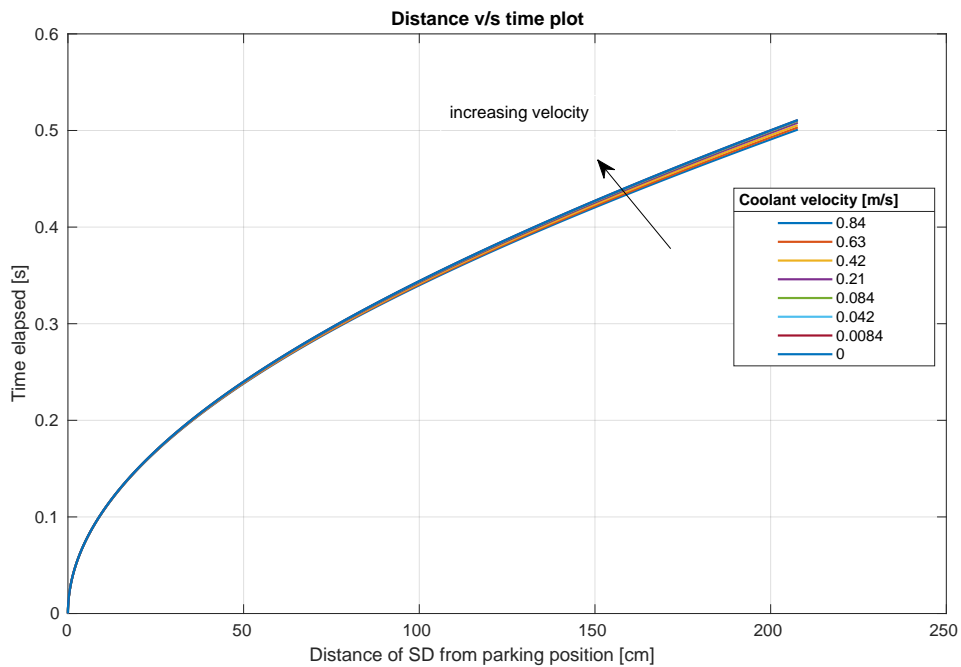


Figure 6.33: Variation of distance with time for different assembly coolant velocity

Figure 6.34 graphically represents this variation and a linear trend was fit to the data as given in Equation 6.29.

Table 6.16: Times of insertion for different assembly coolant velocity

Vel [m/s]	0.84	0.63	0.42	0.21	0.084	0.042	0.0084	0
Time [s]	0.5010	0.5032	0.5055	0.5081	0.5097	0.5103	0.5107	0.5109

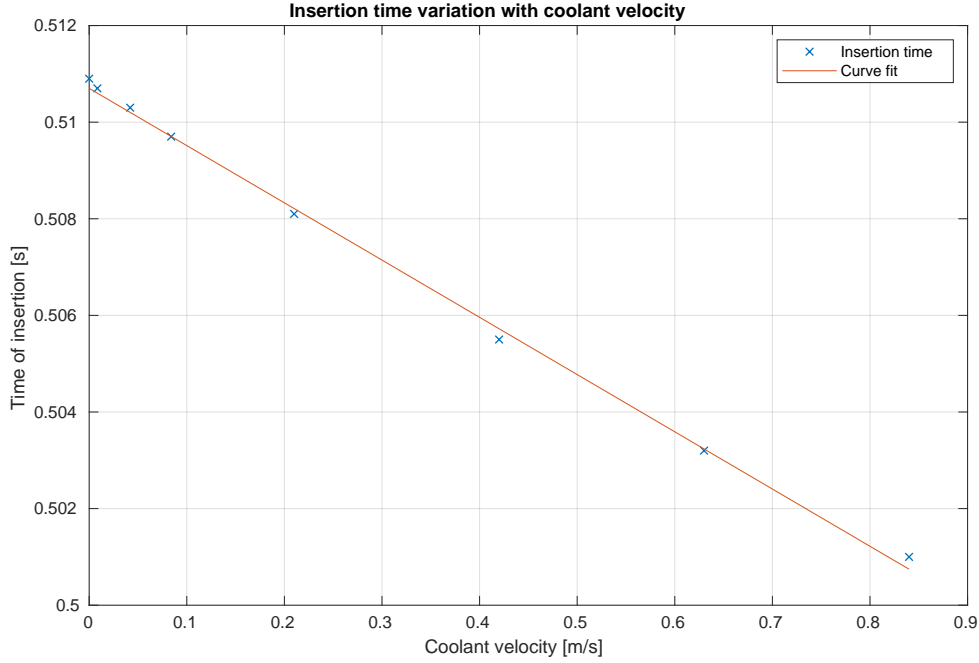


Figure 6.34: Variation of time of insertion with coolant velocity

$$t_{insertion} = (-0.01185 \pm 0.00053) * v_{cool} + (0.5107 \pm 0.0002) \quad (6.29)$$

6.3.2.4 Sensitivity Analysis for Average Form Drag Coefficient

We have already seen the results for the drag coefficient of 50. Here we determine the results for other profiles that were designed in FLUENT. Figure 6.35 presents the distance versus time plots for the considered profiles, while Table 6.17 summarises the total times of insertion.

Table 6.17: Times of insertion for different drag coefficient cases

Case	<i>case_cone45</i>	<i>case_ogive2</i>	<i>case_ogive1</i>	<i>case_cone60</i>	<i>case_hemi</i>
Time [s]	0.5010	0.5026	0.5032	0.5137	0.5186
Case	<i>case_cone90</i>	<i>case_flat</i>	<i>case_25</i>	<i>case_50</i>	
Time [s]	0.5381	0.6672	1.2411	1.4409	

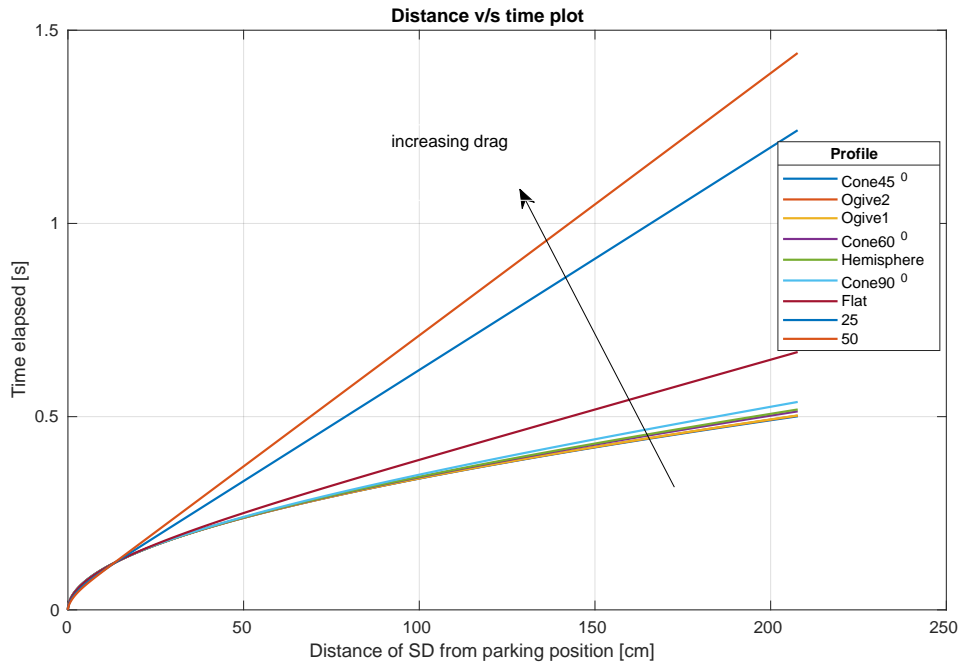


Figure 6.35: Variation of distance with time for different form drag coefficients

Figure 6.36 graphically represents this variation and a two factor power function is fit to the data as given in Equation 6.30.

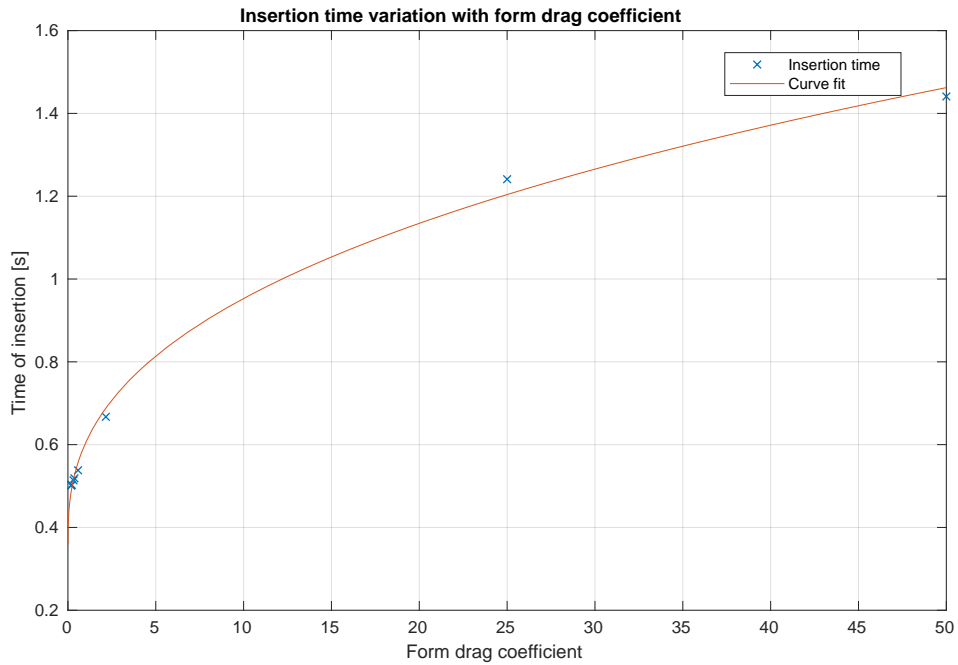


Figure 6.36: Variation of time of insertion with drag coefficient

$$t_{insertion} = (0.2454 \pm 0.1283) * C_D^{(0.384 \pm 0.114)} + (0.3583 \pm 0.1098) \quad (6.30)$$

6.4 Transient Analysis

A transient system analysis was performed using the multi point dynamics code, BELLA [10]. Primarily developed using MATLAB and SIMULINK, it is based on a lumped parameter approach, consisting of a point wise description of the reactor components, the core, primary system, steam generator and secondary system. It is designed to simulate the group of high probability ATWS accidents, namely the *unprotected loss of flow* (ULOF), the *unprotected loss of heat sink* (ULOHS) and the *unprotected transient overpower* (UTOP). Currently under development for SEALER-UK reactor, the passive shutdown system was incorporated into this code. Figure 6.37 shows the schematics of the point wise approximation and coupling between the different components. The core is considered a point like system, performing multi physics calculations for the thermal hydraulics, reactivity and the neutronics. This interlinking between the systems is presented in Figure 6.38. Strictly speaking about the thermal hydraulic calculation, for each numerical step, BELLA solves the heat transfer equations and determining the temperatures of the coolant in the core, of the fuel centerline and of the clad, similar to the thermal hydraulics calculations performed during the beginning of the thesis, in Chapter 5. The temperatures are fed to the reactivity block which computes the total reactivity changes in the core, using Equation 5.26. Two additional terms are included here, the external reactivity of CR bank and reactivity of the shutdown system. The reactivity of the core is passed on to the neutronics block, which solves the point kinetics Equation 6.31 and 6.32.

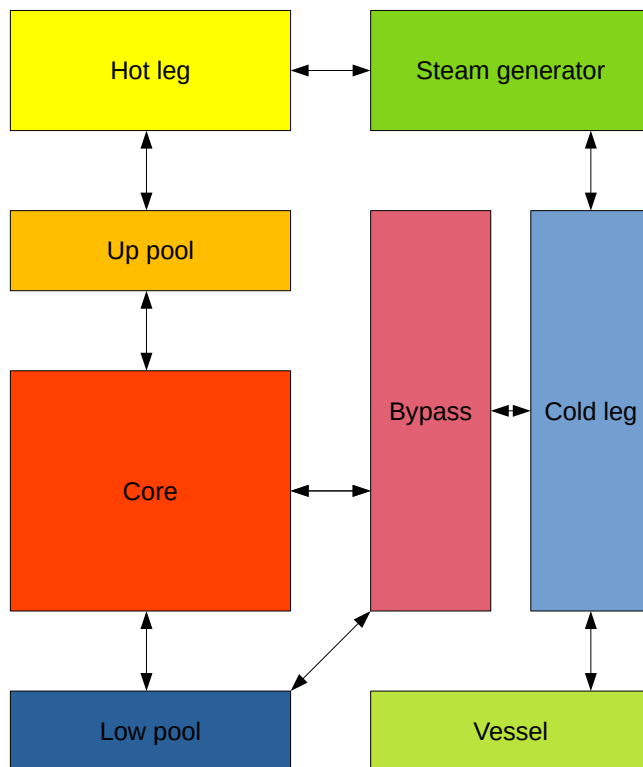


Figure 6.37: Schematics of the different components of BELLA

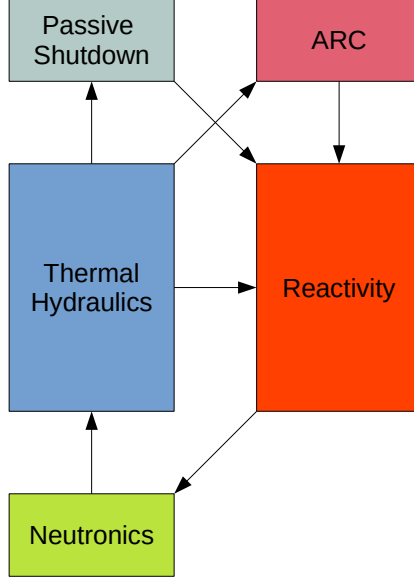


Figure 6.38: Schematics of the core components of BELLA

$$\frac{dn(t)}{dt} = \frac{\rho(t) - \beta_{eff}}{\Lambda_{eff}} n(t) + \sum_{i=1}^k \lambda_i C_i(t) = 1 \quad (6.31)$$

$$\frac{dC_i(t)}{dt} = \frac{\beta_i}{\Lambda_{eff}} n(t) - \lambda_i C_i(t) \quad (6.32)$$

$\rho(t)$ is the instantaneous reactivity, β_{eff} is the effective delayed neutron fraction, Λ_{eff} is the effective neutron reproduction time, $C_i(t)$ is the delayed precursor group concentration, β_i and λ_i are the delayed fraction and decay rate for the precursor groups. The power evolution is determined using the neutron density $n(t)$ parameter as shown in Equation 6.33.

$$\dot{Q}(t) = \frac{\dot{Q}(0)}{n(0)} n(t) \quad (6.33)$$

Figure 6.38 shows the interlinking between two additional blocks. The *Autonomous Reactivity Control* (ARC) is a self-driven passive safety system similar to the lithium injection module explained in the preliminary background studies on passive safety. This system was implemented specifically to control minor but quick reactivity changes occurring in the reactor passively [63]. The passive shutdown system block, the schematics of which is shown in Figure 6.39, is incorporated in the code, which effectively provides the time dependent reactivity of the shutdown system. The reactivity of the shutdown system as a function of length of insertion was determined by fitting a 7th degree polynomial to the S-curve of the SD bank, see Figure 5.16.

$$\rho_{SD}(h) = p_1 * h^7 + p_2 * h^6 + p_3 * h^5 + p_4 * h^4 + p_5 * h^3 + p_6 * h^2 + p_7 * h + p_8 \quad (6.34)$$

p_1	p_2	p_3	p_4	p_5	p_6	p_7	p_8
-299.2	2229	-6108	7206	-3061	175.7	229.1	0.5169
± 250.7	± 7.2	± 4993	± 6436	± 3661.4	± 618	± 251.1	± 30

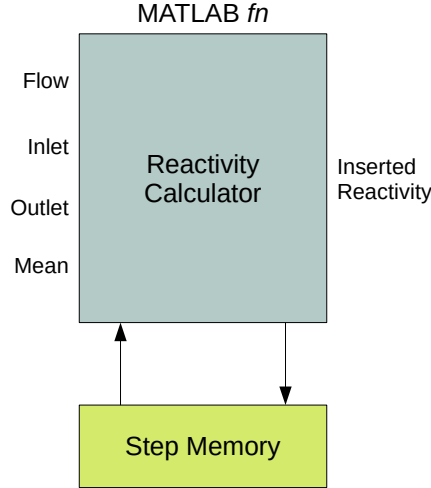


Figure 6.39: Schematics of the passive shutdown block of BELLA

The main block is the MATLAB function which is very similar to the code developed for the study of passive gravity assisted insertion. What is different from that code is that, in the dynamic analysis the coolant conditions vary for each time step. The system has the following inputs, coolant flow rate, inlet coolant temperature, mean coolant temperature and outlet coolant temperature. The flow rate is required to dynamically compute the coolant velocity and subsequently the drag force, temperatures are required to account for buoyancy forces. Unlike the rest of the systems, the shutdown system relies on absolute values of time, this requires storing of the previous step parameters, such as velocity and height inserted. To store these variables a step memory block is used which delays the signal propagation by a step. The function outputs the inserted reactivity that is used by the neutronics block to compute the total reactivity in the core. One must remember that the transient is generally not unprotected because the insertion of SD system is a protected transient.

6.4.1 Results

At MoL the CR bank is inserted to a height above 45cm above bottom of AZ and the approximate reactivity worth of the bank is 700pcm. For the analysis here it is assumed that half the CR assemblies are withdrawn in 1s, this insertion of 350pcm is roughly 50pcm greater than $0.5\beta_{eff}$ and is a highly unlikely scenario. However to have a conservative study the insertion of 350pcm is considered. Additionally two kinds of delay is considered. One, assuming that a Curie Point Electro Magnet (CPEM) or latch is implemented in the upper pool of the core. The second case considered is a constant delay of 10s after onset of transient. The former is to see how the system behaves under changing temperature fields. The CPEM material is considered to be made of pure iron having Curie temperature of 770°C [76]. This is

a reasonable assumption as the higher temperature limit is possible in LFRs having high boiling point of coolant. The latter depends on the type of control systems in place, and how the control system manages the reactor trip, it is required to see how the reactivity feedback affect the reactor. Additionally depending on the type of self actuated systems incorporated in the future, the initiation of shutdown can be ideally adjusted for different Curie temperatures. The power evolution for the transient is shown in Figure 6.40, while the reactivity evolution during the transient is shown in Figure 6.41.

The power spikes to 680MW from the nominal 140MW , on insertion of 350pcm reactivity. However due to reactivity feedback from the changes in temperature of fuel and coolant the power is brought back to the nominal case, in the instance where the reactor is not tripped. In the case when the reactor is shutdown, the power level drastically falls to near zero state. The code incorporates decay heat generation, and thus the power level is seen to stagnate slightly above zero. The total reactivity for the case with no scram, is seen to quickly increase with the sudden withdrawal of CR, however the reactivity feedback brings the arrests the increase and brings it to normal critical state. Not very large difference is seen between the cases when the shutdown systems are inserted. The temperature⁴ of the coolant spikes and surpasses the Curie temperature in short delay period of 14s after the onset of transient. When the core is shutdown, the absorbers have a worth of $868\pm 28\text{pcm}$ which is seen as the constant negative reactivity, bringing the core sub-critical by 220pcm . The total reactivity in this case is seen to abruptly stagnate at this value after 200s , mainly due to the core components reaching the cold nominal temperatures.

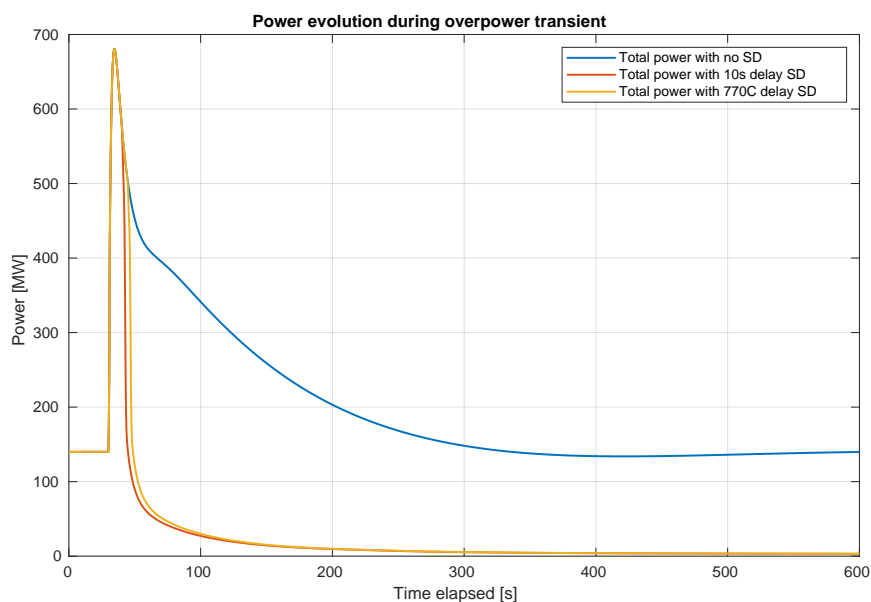


Figure 6.40: Total power changes during transient overpower scenario

⁴The temperature plots are provided in Appendix A

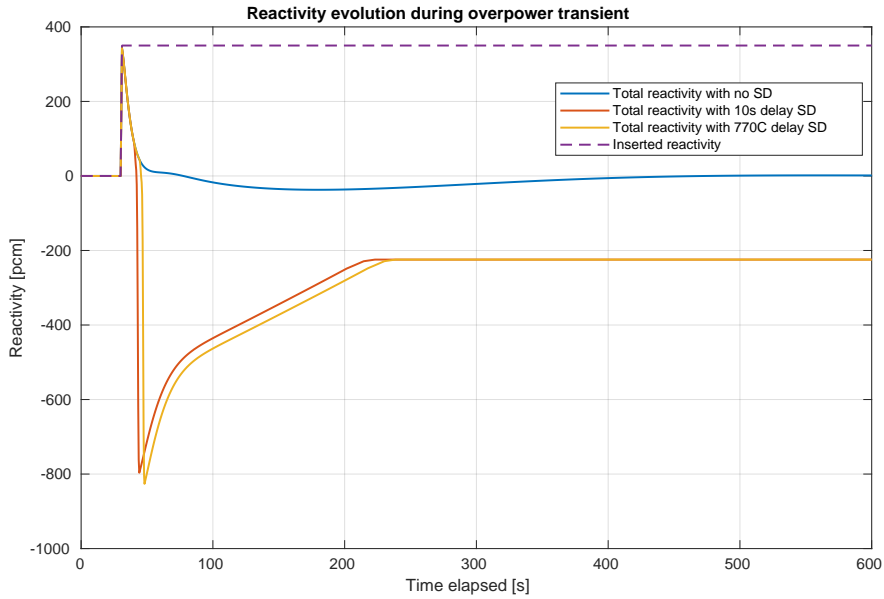


Figure 6.41: Total reactivity changes during transient overpower scenario

It may seem to be a very drastic change on the component materials, inducing very harsh thermal shock, while this stagnation causes the individual components of reactivity, namely the Doppler reactivity, fuel axial and radial reactivity, core radial reactivity and coolant density reactivity to also reach a constant value. The enlarged plot of reactivity changes for the different cases of delayed actuation is presented in Figure 6.42, and the corresponding temperature plot enlarged to the same limits is shown in Figure 6.43. The ideal case is when no CR is abruptly ejected, but a benchmark against the earlier MATLAB code, by inserting only the shutdown system assisted by gravity.

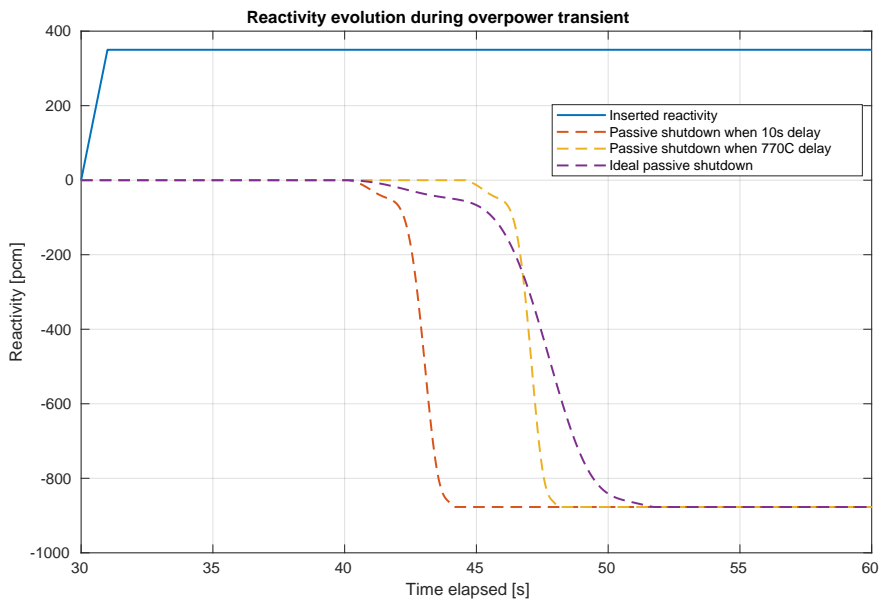


Figure 6.42: Reactivity changes of the shutdown system during transient overpower scenario for different cases of actuation

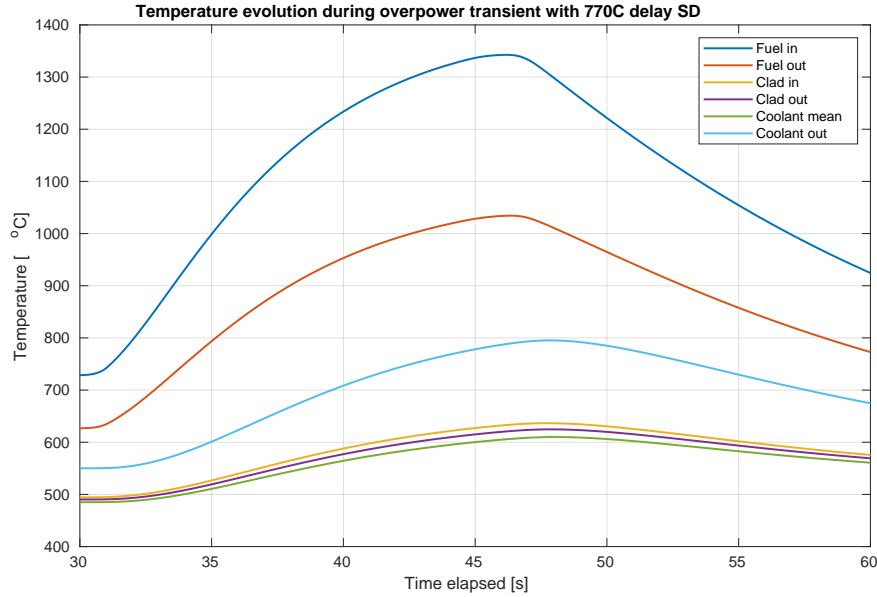


Figure 6.43: Temperature changes during shutdown delayed by the deactivation of the Curie point latch

It can be identified that just when the coolant outlet temperature crosses the 770°C mark the insertion of shutdown assembly starts (yellow dashed line) at approximately 44s . The total times of insertion by gravity for the cases vary, because of changing core temperatures and flow conditions⁵. The insertion periods are, respectively for 10s delay, CPEM actuated passive insertion and nominal case, 4.3s , 4.1s and 11.9s . The faster insertion times can be attributed to drastic changes in coolant density, thereby affecting buoyancy forces, in addition to reduction in coolant velocity thereby reducing the drag forces. It must be noticed that the nominal case insertion period is slightly greater in comparison to 10.609s computed by the code. The reasons might include the interference from various subsystems, the arguably large time steps adopted by the numerical ODE15s solver of MATLAB/SIMULINK.

This transient with the ejection of CR, worth 350pcm is highly unlikely. A more realistic value to study the transient is about 0.2% , which translates to about 120pcm , the approximate worth of a single CR assembly. The CR bank made of B_4C is very buoyant and the withdrawal in case of control rod drive mechanism failure, which is the major cause for this transient, requires 0.5s to be extracted from the initial position inside the core. This value was calculated by modifying the code developed for buoyancy insertion calculations. However in keeping track with the previous transient it was assumed to occur in 1s . Results for this case are presented in the Appendix A.

⁵See Appendix A for the temperature and coolant flow plots

The thesis presents a detailed investigation into the possibility of passive shutdown system implementation in a small lead cooled fast reactor. The initial neutronics assessment was followed by rigorous study on the gravity driven shutdown system, the main objective of the thesis. The forces identified to affect the insertion were identified. Some approximations had to be made in order to simplify the system and also due to unavailability of precise information regarding the designs. This however was not a setback, as designs were proposed that could potentially solve the issues encountered by performing sensitivity analyses. The issues that were encountered, relates to excessive drag forces that hamper effective insertion of shutdown system by gravity.

The study showed that having a carefully designed shutdown assembly can indeed be passively inserted by gravity in a lead cooled reactor. Sensitivity analysis of the drag coefficient showed that its reduction plays effective role as any, in reducing the time of insertion. The study concluded that there is a limit to the maximum form drag coefficient a foot profile can have, above which gravity driven shutdown is not possible. This is in line with the early impression that solving for drag forces is the crux of the problem. Addition of ballasts is concluded to be a mandatory requirement to achieve reasonably quick insertion speeds. Finally the sensitivity analysis on the bypass coolant flow in the shutdown assembly channel showed that the coolant velocity does affect the speed of insertion.

The thesis satisfactorily achieves three of the initial thesis objectives, while the results obtained in the hope of attaining the final objective were not overly satisfactory. The potent transient code BELLA was substituted for the comprehensive dynamic analysis using a full core simulation in OpenFOAM, due to constraints in time. Nevertheless, the shutdown system model was successfully incorporated in BELLA, which revealed that during particular transients the core conditions are more favourable for passive insertion by gravity than previously thought. This should be a pointer, that a systems utility is to be assessed in scenarios that it is actually intended to function in. Finally, given that very few published literature exists advocating the application of gravity-driven shutdown system in heavy liquid metal reactors, it is hoped that this work is a step in the right direction to bridge the gap.

7.1 Practical Implications

The application of passive safety systems is sought after by many designers working on modern and Gen. IV systems. Passive shutdown systems, especially, has its benefits to solving many issues related to safety, reliability or economics of reactor design. This study provides, a first order approximation nevertheless, proof that gravity driven shutdown is possible in lead cooled fast reactors, given certain criteria are met regarding the design. Incorporating gravity-driven shutdown system could potentially reduce probability of core damage during accidents, as passive systems have smaller chances of failure than active systems. In the practical aspect introduction of ballasts in the shutdown assembly is suggested, to improve speeds of insertion. This would incur additional cost for the expensive ballast material. Drag coefficient needs to be minimised, which demands very precise design and development of the assembly. An effect of shutdown is reduction in temperatures, which increases buoyancy forces. This may have a tendency to eject the inserted assembly, which therefore must be restrained once inserted. Implications of adopting a buoyancy assisted system bring challenges to redesign the small reactor to accommodate assembly insertion from below the core. This is against the objective of developing a small lead-cooled reactor.

7.2 Future Research

The study focused on different aspects of the topic ranging from fluid mechanics and thermal hydraulics to reactor physics. Over the course of the study several approximations were made to simplify modelling while compromising on accuracy. It would be worthwhile to include additional components such as pressure energy, additional fluid mechanical effects such as vortices and eddies in the MATLAB code. In the same field, study aimed at streamlining the assembly is a viable option. As this is a fairly newer perspective to gravity driven passive shutdown in heavy metal cooled reactors, the possibility to expand the research base is very broad.

The study focused on CFD simulations for extracting drag coefficient data. CFD is always to be supplemented with rigorous experimental testing. This, is an open field for research to study and validate the results presented herein.

Another possible extension to the present work is to research on potential self or passive actuators that can fully passivise the shutdown system. Several such devices were introduced in this work but were not elaborated in much details, and could be the basis for future research.

Penultimately, the BELLA code requires modification to account for shutdown characteristics and behaviour of the core as was discovered during the transient system analysis. The same code can be used in analysis of other ATWS namely LOHS and LOF, the latter being of interest because of sensitivity of coolant flow to the insertion mechanism. This is very much needed, as it was seen that in a TOP scenario the system response is more effective than during nominal conditions.

Incorporation of the full core model and utilising the multi-physics solver GeN-Foam would provide better clarity and validation for the work performed here. Additionally one can venture a step further to implement a neutronics coupling between OpenFOAM and a Monte Carlo code such as OpenMC or Serpent.

BIBLIOGRAPHY

- [1] UNFCCC, *Paris Agreement*. United Nations Framework Convention on Climate Change (UNFCCC), 2015.
- [2] D. Siqueira, J. Meystre, M. Hilário, D. Rocha, G. Menon, and R. Silva, “Current perspectives on nuclear energy as a global climate change mitigation option,” *Mitigation and Adaptation Strategies for Global Change*, Sep 2018.
- [3] IAEA, *Energy, electricity and nuclear power estimates for the period up to 2050*, vol. 1. Vienna: International Atomic Energy Agency (IAEA), 2017.
- [4] WNA, *World Nuclear Performance Report 2018*. World Nuclear Association (WNA), Aug 2018.
- [5] NEA/IEA, *Technology Roadmap: Nuclear Energy 2015 Edition*. Nuclear Energy Agency (NEA), International Energy Agency (IEA), 2015.
- [6] GIF, *A Technology Roadmap for Generation IV Nuclear Energy Systems 2002*. U.S. DOE Nuclear Energy Research Advisory Committee and the Generation IV International Forum (GIF), 2002.
- [7] LeadCold Reactors, “SEALER-UK.” <https://www.leadcold.com/sealer.html>, Accessed 2019/05/25.
- [8] J. Wallenius, S. Qvist, I. Mickus, S. Bortot, P. Szakalos, and J. Ejenstam, “Design of sealer, a very small lead-cooled reactor for commercial power production in off-grid applications,” *Nuclear Engineering and Design*, vol. 338, 2018.
- [9] UKRI, “Nuclear advanced modular reactors, feasibility and development competition.” <https://www.ukri.org/freedom-of-information/foi-disclosure-log/ukri-foi-2018-0075-iuk-pdf/>, 2018.
- [10] S. Bortot, E. Suvdantsetseg, and J. Wallenius, “Bella: a multi-point dynamics code for safety-informed design of fast reactors,” *Annals of Nuclear Energy*, vol. 85, 2015.
- [11] K. Mikityuk, S. Pelloni, P. Coddington, E. Bubelis, and R. Chawla, “Fast: An advanced code system for fast reactor transient analysis,” *Annals of Nuclear Energy*, vol. 32, no. 15, 2005.

- [12] C. Fiorina, I. Clifford, M. Aufiero, and K. Mikityuk, “GeN-Foam: a novel OpenFOAM® based multi-physics solver for 2D/3D transient analysis of nuclear reactors,” *Nuclear Engineering and Design*, vol. 294, 2015.
- [13] EC-JRC, *Guidance Document for Integrated Safety Assessment Methodology (ISAM) – (GDI)*. European Commission, Joint Research Centre (EC-JRC), 2014.
- [14] S. Ross, M. El-Genk, and R. Matthews, “Uranium nitride fuel swelling correlation,” *Journal of Nuclear Materials*, vol. 170, no. 2, 1990.
- [15] G. Muller, A. Heinzl, J. Konys, G. Schumacher, A. Weisenburger, F. Zimmermann, V. Engelko, A. Rusanov, and V. Markov, “Behavior of steels in flowing liquid PbBi eutectic alloy at 420-600°C after 4000-7200 h,” *Journal of Nuclear Materials*, vol. 335, no. 2, 2004.
- [16] J. Ejenstam, M. Halvarsson, J. Weidow, B. Jonsson, and P. Szakalos, “Oxidation studies of Fe10CrAl-RE alloys exposed to Pb at 550°C for 10,000h,” *Journal of Nuclear Materials*, vol. 443, no. 1, 2013.
- [17] A. Lech, *Synthesis, Structure, and Properties of Refractory Hard-Metal Borides*. eScholarship, University of California, 2014. PhD Thesis.
- [18] A. Lech, C. Turner, J. Lei, R. Mohammadi, S. Tolbert, and R. Kaner, “Superhard rhenium-tungsten diboride solid solutions,” *Journal of the American Chemical Society*, vol. 138, no. 43, 2016.
- [19] IAEA, *The Fukushima Daiichi Accident-Report by the Director General*. Vienna: International Atomic Energy Agency (IAEA), 2015.
- [20] IAEA, *Safety related terms for advanced nuclear plants*. Vienna: International Atomic Energy Agency (IAEA), 1991.
- [21] I. Cameron, *Nuclear Fission Reactors*. New York: Springer US, 1982.
- [22] J. Nims and P. Zweifel, *Preliminary Report On Sodium Temperature Coefficients In Large Fast Reactors*. Atomic Power Development Associates, 1959.
- [23] J. Whitlock, W. Garland, and M. Milgram, “Effects contributing to positive coolant void reactivity in CANDU,” *Transactions of the American Nuclear Society*, vol. 72, 1995.
- [24] J. Josephson and E. Sowa, “The Design and Testing of a Self-Actuated Shutdown System for the Protection of Liquid Metal Fast Breeder Reactors (LMF-BRS),” *IEEE Transactions on Nuclear Science*, vol. 24, 05 1977.
- [25] L. Burgazzi, “Analysis of solutions for passively activated safety shutdown devices for SFR,” *Nuclear Engineering and Design*, vol. 260, 2013.
- [26] M. Kambe, “Experimental and analytical investigation of the fast reactor passive shutdown system: Lim,” *Journal of Nuclear Science and Technology*, vol. 43, no. 6, 2006.

- [27] J. DeWitte, N. Todreas, and M. Driscoll, "Self-actuated shutdown system performance in sodium fast reactors," *Transactions of the American Nuclear Society*, vol. 103, 2010.
- [28] G. Grasso, C. Petrovich, D. Mattioli, C. Artioli, P. Sciora, D. Gugiu, G. Bandini, E. Bubelis, and K. Mikityuk, "The core design of ALFRED, a demonstrator for the European lead-cooled reactors," *Nuclear Engineering and Design*, vol. 278, no. 1, 2014.
- [29] P. Baeten, M. Schyns, R. Fernandez, E. Bruyn, and G. V. den Eynde, "MYRRHA: A multipurpose nuclear research facility," *EPJ Web of Conferences*, vol. 79, 2014.
- [30] A. Zrodnikov, G. Toshinsky, O. Komlev, Y. Dragunov, V. Stepanov, N. Klimov, V. Generalov, I. Kopytov, and V. Krushelnitsky, "Innovative nuclear technology based on modular multi-purpose lead bismuth cooled fast reactors," *Progress in Nuclear Energy*, vol. 50, no. 2, 2008.
- [31] I. Hwang, M.H.Kim, H. Joo, K. Woo, B. Yoo, H. Kim, S. Rok, J. Yoon, J. Gye, Shin, M. Kwang, J. Yong, D. Y. and J. Han, H. Lim, J. Hyun, Y. Cho, C. Hyo, and Kim, "PASCAR-A Small Modular Reactor for PEACER Demonstration," *Transactions of the Korean Nuclear Society Spring Meeting*, 05 2008.
- [32] D. Cacuci, *Handbook of Nuclear Engineering*. New York: Springer US, 1982.
- [33] T. Inagaki, K. Ohba, H. Tazawa, and T. Murakami, "Design study of the demonstration fbr in japan," *Progress in Nuclear Energy*, vol. 37, no. 1, 2000.
- [34] S. Kotake, Y. Sakamoto, T. Mihara, S. Kubo, N. Uto, Y. Kamishima, K. Aoto, and M. Toda, "Development of advanced loop-type fast reactor in japan," *Nuclear Technology*, vol. 170, no. 1, 2010.
- [35] Y. Shin, S. Choi, J. Cho, J. Kim, and I. Hwang, "Advanced passive design of small modular reactor cooled by heavy liquid metal natural circulation," *Progress in Nuclear Energy*, vol. 88, 2015.
- [36] IAEA, *Technical Meeting on Passive Shutdown Systems for Liquid Metal-Cooled Fast Reactors*. Vienna: International Atomic Energy Agency (IAEA), 2015.
- [37] V. Babu, R. Vijayashree, S. Govindarajan, G. Vaidyanathan, G. Muralikrishna, T. S. S. Chetal, K. Raghavan, and S. Bhoje, "Design philosophy of PFBR shutdown systems," *IAEA-TECDOC-884*, 1996.
- [38] G. Petrangeli, *Nuclear safety*. Butterworth-Heinemann, 2006.
- [39] E. Blandford and P. Peterson, "A buoyantly-driven shutdown rod concept for passive reactivity control of a Fluoride salt-cooled High-temperature Reactor," *Nuclear Engineering and Design*, vol. 262, 2013.
- [40] E. Blandford and P. Peterson, "A novel buoyantly-driven shutdown rod design for passive reactivity control of the PB-AHTR," *ASME Fourth International Topical Meeting on High Temperature Reactor Technology*, vol. 2, 2008.

- [41] E. Blandford, “Physical similitude in hierarchical engineered systems,” *Doctoral Dissertation*, 2010.
- [42] Z. Lin, L. Zhai, L. Zhu, X. Wang, X. Zhang, Y. Cao, and N. Wang, “Control rod drop dynamic analysis in the TMSR-SF1 based on numerical simulation and experiment,” *Nuclear Engineering and Design*, vol. 322, 2017.
- [43] V. Babu, G. Thanigaiyarasu, and P. Chellapandi, “Mathematical modelling of performance of safety rod and its drive mechanism in sodium cooled fast reactor during scram action,” *Nuclear Engineering and Design*, vol. 278, 2014.
- [44] J. Donis and H. Goller, “A mathematical model of a control rod drop,” *Nuclear Engineering and Design*, vol. 23, no. 1, 1972.
- [45] S. Taliyan, D. Roy, R. Grover, M. Singh, and G. Govindarajan, “Dynamics of shut-off rod drop in a PHWR,” *Nuclear Engineering and Design*, vol. 147, no. 3, 1994.
- [46] H. Andriambololona, D. Bosselut, and P. Massin, “Methodology for a numerical simulation of an insertion or a drop of the rod cluster control assembly in a PWR,” *Nuclear Engineering and Design*, vol. 237, no. 6, 2007.
- [47] A. Rabiee and A. Atf, “Control rod drop hydrodynamic analysis for a pressurized water reactor,” *Progress in Nuclear Energy*, vol. 88, 2016.
- [48] MathWorks Inc., “MATLAB & SIMULINK,” R2019a.
- [49] P. Romano, N. Horelik, B. Herman, A. Nelson, B. Forget, and K. Smith, “OpenMC: A state-of-the-art Monte Carlo code for research and development,” *Annals of Nuclear Energy*, vol. 82, 2015.
- [50] J. Leppanen, M. Pusa, T. Viitanen, V. Valtavirta, and T. Kaltiainenaho, “The Serpent Monte Carlo code: Status, development and applications in 2013,” *Annals of Nuclear Energy*, vol. 82, 2015.
- [51] ANSYS Inc., “FLUENT,” R18.2 Academic.
- [52] A. Waltar, D. Todd, and P. Tsvetkov, *Fast Spectrum Reactors*. Springer US, 2012.
- [53] S. Hayes, J. Thomas, and K. Peddicord, “Material property correlations for uranium mononitride: I. Physical properties,” *Journal of Nuclear Materials*, vol. 171, no. 2, 1990.
- [54] L. Luzzi, S. Lorenzi, D. Pizzocri, D. Rozzia, and A. Nevo, *Modeling and analysis of nuclear fuel pin behavior for innovative lead cooled FBR*. Agenzia nazionale per le nuove tecnologie, l’energia e lo sviluppo economico sostenibile (ENEA), 2014. ADPFISS-LP2-054.
- [55] Y. Kim and G. Hofman, *AAA Fuels Handbook*. Argonne National Laboratory (ANL), 2003.
- [56] L. Buiron, *CP ESRF Working Horses Core Concept Definition*. Commissariat à l’énergie atomique et aux énergies alternatives (CEA), 2009. D SP2.1 2. 0 D1.

- [57] T. Dengg, V. Razumovski, L. Romaner, G. Kresse, P. Puschnig, and J. Spitaler, “Thermal expansion coefficient of WRe alloys from first principles,” *Journal of Physics B: Solid State Physics*, vol. 96, 2017.
- [58] K. Field, M. Snead, Y. Yamamoto, and K. Terrani, *Handbook on the material properties of FeCrAl alloys for nuclear power production applications*. Oak Ridge National Laboratory (ORNL), Brookhaven National Laboratory (BNL), 2017. ORNL/TM-2017/186.
- [59] H. Hayashi, T. Saitou, N. Maruyama, H. Inaba, K. Kawamura, and M. Mori, “Thermal expansion coefficient of yttria stabilized zirconia for various yttria contents,” *Solid State Ionics*, vol. 176, no. 5, 2005.
- [60] S. Qvist, “Reactivity swing as a function of burnup for uranium-fueled fast reactors,” *Nuclear Technology*, vol. 190, no. 1, 2015.
- [61] J. Leppänen, M. Aufero, E. Fridman, R. Rachamin, and S. Marck, “Calculation of effective point kinetics parameters in the Serpent 2 Monte Carlo code,” *Annals of Nuclear Energy*, vol. 65, 2014.
- [62] J. Leppänen, *Serpent User’s Manual*. VTT Technical Research Center of Finland Ltd., 2015.
- [63] F. Dehlin, *Implementation of an Autonomous Reactivity Control (ARC) system in a small lead-cooled fast reactor*. KTH Royal Institute of Technology, 2019. MSc Thesis.
- [64] D. Mahagin, “Fast reactor neutron absorber materials,” *Office of Scientific and Technical Information (OSTI)*, 1979.
- [65] J. Wallenius, *Shutdown rod for lead-cooled reactors*. World Intellectual Property Organization (WIPO), 2017. Patent No WO2017105325A1.
- [66] X. Deschanel, P. Bry, J. Koci, and B. Provot, *Absorbent neutronic composite material and method for producing same*. United States Patent And Trademark Office (USPTO), 2002. Patent No US6334963B1.
- [67] OECD/NEA, *JEFF3.3 Cross Section Library*. Organisation for Economic Cooperation and Development (OECD), Nuclear Energy Agency (NEA), Accessed 2019/05/25.
- [68] Thermalloys AB, *Properties of FeCrAl alloys*. Thermalloys AB, Thermal Alloys Engineering, Accessed 2019/05/25.
- [69] BGS, *GB Land Gravity Survey*. British Geological Survey (BGS), Accessed 2019/05/25.
- [70] A. Kirshenbaum, J. Cahill, and A. Grosse, “The density of liquid lead from the melting,” *Journal of Inorganic and Nuclear Chemistry*, vol. 22, 1961.
- [71] H. Yang, M. Fan, A. Liu, and L. Dong, “General formulas for drag coefficient and settling velocity of sphere based on theoretical law,” *International Journal of Mining Science and Technology*, vol. 25, 2015.

- [72] Y. Cengel, *Fluid Mechanics*. Tata McGraw-Hill Education, 2010.
- [73] S. Hoerner, *Fluid Dynamic Drag*. Hoerner fluid dynamics, 1965.
- [74] E. Mayo, *Newtonian Aerodynamics For Tangent Bodies Of Revolution*. National Aeronautics And Space Agency-Goddard Space Flight Center (NASA-GSFC), 1965.
- [75] Wolfmet, *Wolfmet Tungsten Alloys Technical Information*. Wolfmet, M&I Materials, Accessed 2019/05/25.
- [76] T. Misao, S. Takashi, A. Takafumi, U. Masato, and K. Shoji, “Demonstration of control rod holding stability of the self actuated shutdown system in joyo for enhancement of fast reactor inherent safety,” *Journal of Nuclear Science and Technology*, vol. 44, 2007.
- [77] OECD/NEA, *Handbook on Lead-bismuth Eutectic Alloy and Lead Properties, Materials Compatibility, Thermal-hydraulics and Technologies*. Organisation for Economic Co-operation and Development (OECD), Nuclear Energy Agency (NEA), 2015.
- [78] K. Mikityuk, “Heat transfer to liquid metal: Review of data and correlations for tube bundles,” *Nuclear Engineering and Design*, vol. 239, 2009.

APPENDIX A

SUPPLEMENTARY DATA AND CALCULATIONS

A.1 Convective Heat Transfer Coefficient

Figure A.1 shows the cross section of a typical triangular lattice. The diameter D is the outer diameter of the clad and P is the pitch. The heat transfer coefficient (h) ($W/m^2/K$) for a fluid in forced convection case is given by Equation A.1.

$$h = \frac{Nu * k}{D_H} \quad (A.1)$$

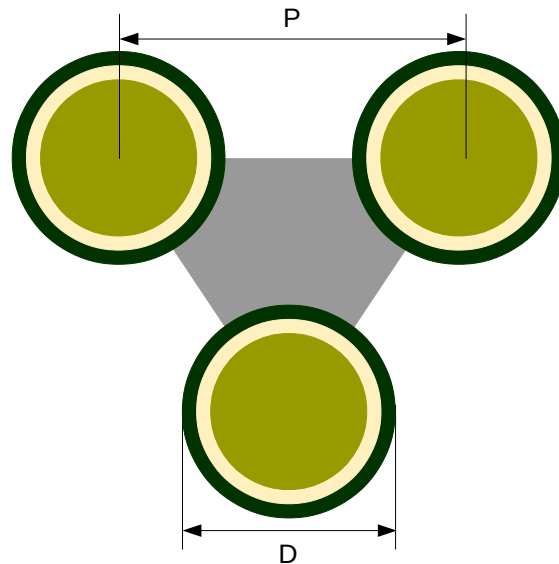


Figure A.1: Triangular sub channel in a hexagonal assembly

k is the thermal conductivity ($W/m/K$) of the fluid. For such an arrangement the hydraulic diameter D_H is given by Equation A.2 where A is cross sectional area of the coolant flow region and P_{wet} is the wetted perimeter.

$$D_H = \frac{4A}{P_{wet}} \quad , \quad D_H = D \left[\frac{2 * \sqrt{3}}{\pi} X^2 - 1 \right] \quad (A.2)$$

X is the ratio of pitch to diameter. This ratio is very important factor in the analysis of coolant flow in rod bundles as it effectively demonstrates what kind of Nusselt (Nu) correlation to be used. These correlations depend on flow conditions such as Reynolds number (Re), Peclet number (Pe) and Prandtl number (Pr) which are given in Equation A.3.

$$Re = \frac{\rho v D_H}{\mu} \quad , \quad Pr = \frac{\mu c_p}{k} \quad , \quad Pe = Re * Pr \quad (A.3)$$

ρ is the density of fluid (kg/m^3), μ is the dynamic viscosity of the fluid, v is the velocity of flow, k is the thermal conductivity of the fluid. These four thermo physical properties ρ , c_p , μ , k are all temperature dependent. The functions relating the properties to temperatures¹ considered in this study is presented below [77].

Density (kg/m^3) of lead:

$$\rho = 11470 - 1.3174T \quad (A.4)$$

$$633 - 1973K$$

Specific heat capacity ($J/kg/K$) of lead:

$$c_{p,b} = 175.1 - 4.961 * 10^{-2}T + 1.985 * 10^{-5}T^2 - 2.099 * 10^{-9}T^3 - 1.524 * 10^{-6}T^{-2} \quad (A.5)$$

$$601 - 2016K$$

Dynamic viscosity (Pas) of lead:

$$\mu = 5.43 * 10^{-4} e^{\frac{938.5}{T}} \quad (A.6)$$

$$603 - 1073K$$

Thermal conductivity ($W/m/K$) of lead:

$$k = 9.2 - 0.011T \quad (A.7)$$

$$603 - 2000K$$

Mikityuk [78] analysed the various Nusselt correlations from available literature and made exhaustive comparison of when to use a particular correlation. He also suggested a new correlation for the available data, as given in Equation A.8.

$$Nu = 0.047(1 - e^{-3.8(X-1)})(Pe^{0.77} + 250) \quad (A.8)$$

$$1.1 < X < 1.95 \quad , \quad 30 < Pe < 5000$$

Having knowledge of the Nusselt number merely from the correlation, the convective heat transfer coefficient is found using Equation A.1. For the thermal hydraulic calculations, the properties are calculated for the coolant temperature at each iteration and corresponding heat transfer coefficient is found which is then used to find clad outlet temperature.

Thermal conductivity ($W/m/K$) of uranium nitride (UN) fuel [53]:

$$k_{fuel} = 1.5048T^{0.3610} \quad (A.9)$$

¹Temperatures are in K unless specified otherwise

Thermal conductivity ($W/m/K$) of 1515Ti steel [8]:

$$k_{clad} = 7.598 + 2.391 * 10^{-2}T - 8.899 * 10^{-6}T^2 \quad (A.10)$$

Thermal conductivity ($W/m/K$) of the gas gap [8]:

$$k_{gap} = 0.27237 \quad (A.11)$$

A.2 Thermal Expansion

The typical variation of thermal expansion coefficient as a function of temperature of the material is shown in Figure A.2. The blue line shows the variation according to set of correlation, for an absolute change in temperature from T_1 to T_2 .

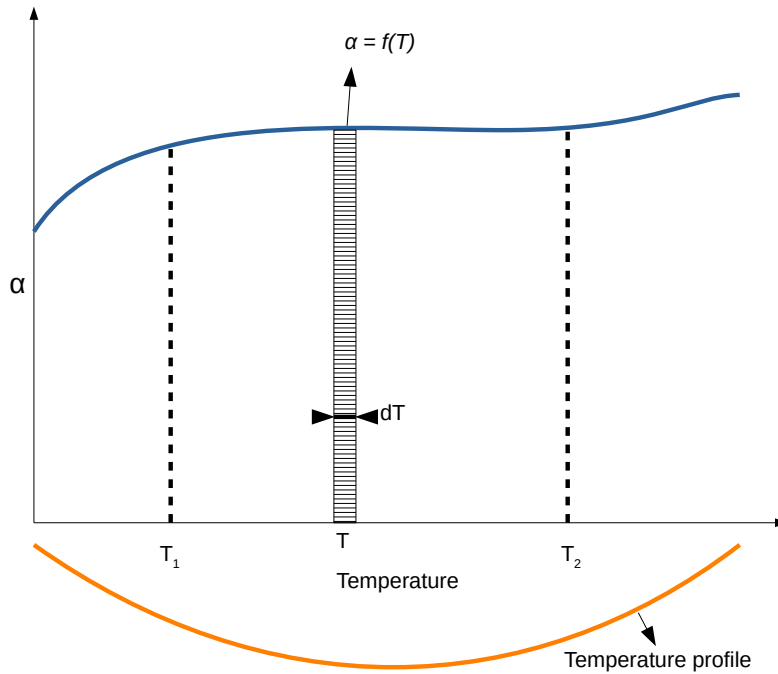


Figure A.2: Temperature dependence of thermal expansion coefficient

It was mentioned while explaining the thermal expansion to hot core geometry that the code was loosely coupled to thermal mechanics to compute elemental expansions after each iteration. Figure A.3 shows the element wise expansion along the height of the fuel pellet. In the first run starting with cold dimensions, the elements expand according to the profile, that is middle elements are expanded more than the peripherals. However in second run, the change in temperature for the thermal expansion is very less, as all the elements have already almost reached their steady state values and thus the elemental expansion is minimal. While this would amount to a more accurate approach for calculating, taking just the mean temperatures was seen to not have any detrimental effect, because while the middle portion expand more than the mean, the peripherals expand less than the mean elements. This partly balances each other, and hence the discrepancy is minimal.

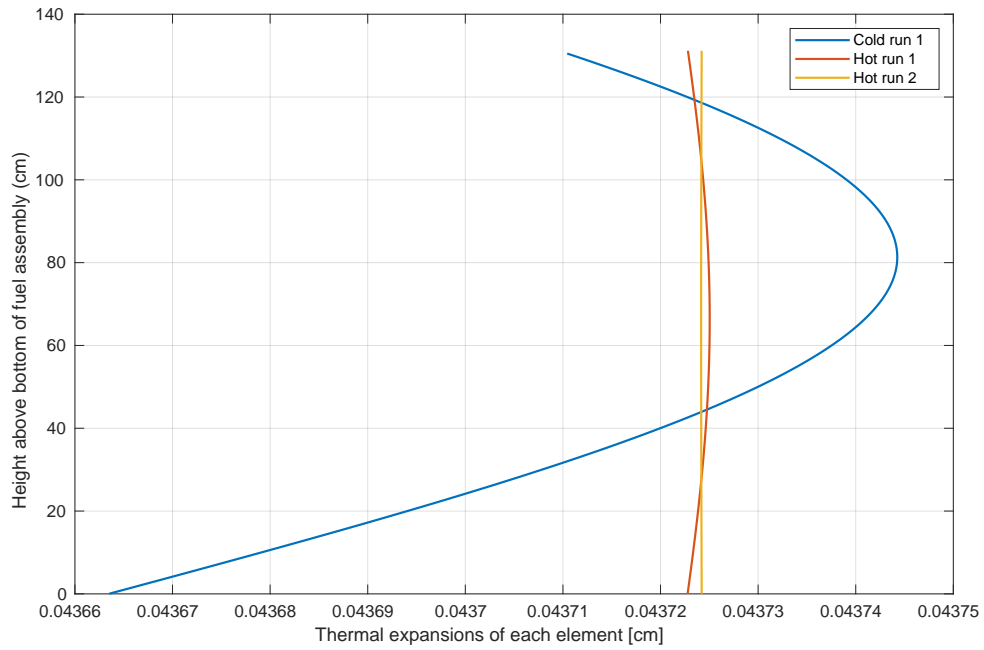


Figure A.3: Thermal expansion of each discretised element

The thermal expansion coefficient of the materials that were used in this study is given in Table 5.2.

A.3 Neutronics: Reactivity Coefficients

The fuel clad coefficient is shown in Figure A.4 and the wrapper coefficient is presented in Figure A.5.

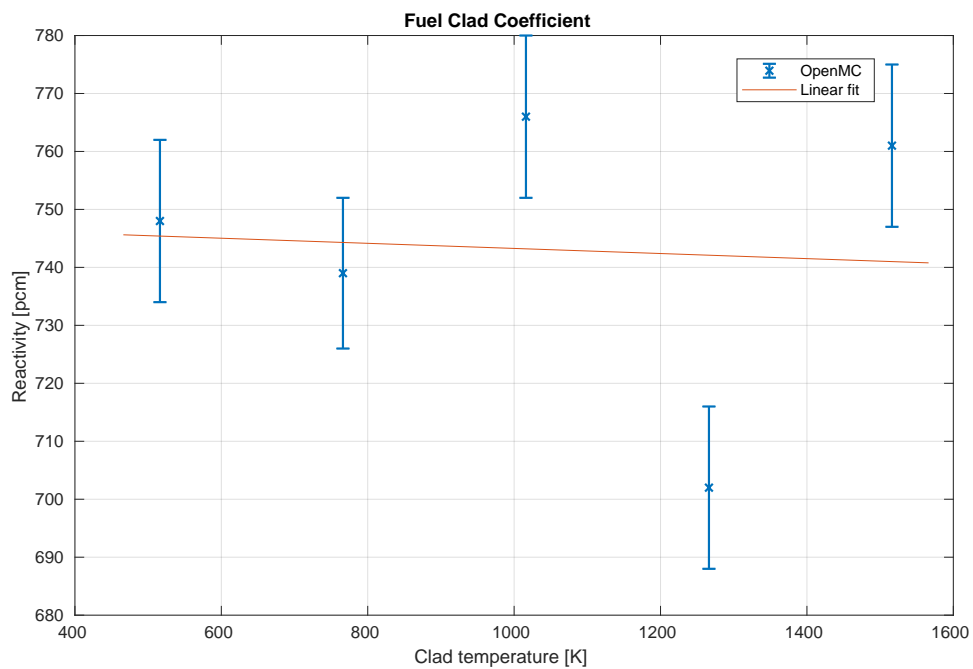


Figure A.4: Variation of reactivity with fuel clad temperature

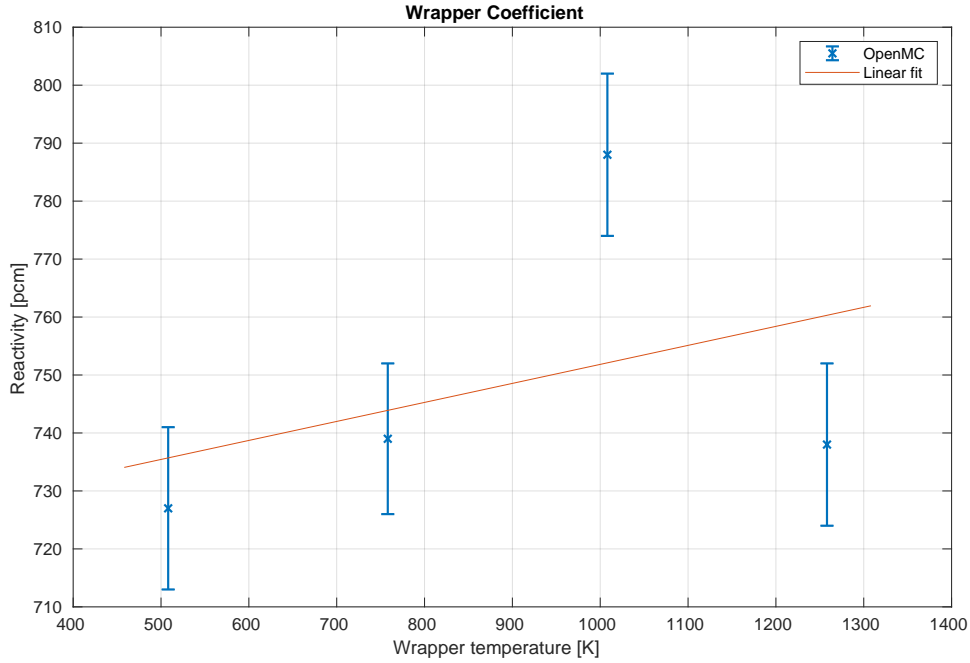


Figure A.5: Variation of reactivity with wrapper temperature

$\alpha_{fuel-clad}$ from the linear fitting is found to be $-0.004 \pm 0.117 pcm/K$ while $\alpha_{wrapper}$ is found to be $+0.033 \pm 0.236 pcm/K$. As it can be seen the uncertainties of the Monte Carlo code dominates the actual value.

A.4 Transient Analysis

Reactivity plot for a transient of insertion of $350 pcm$ and $10s$ delayed shutdown.

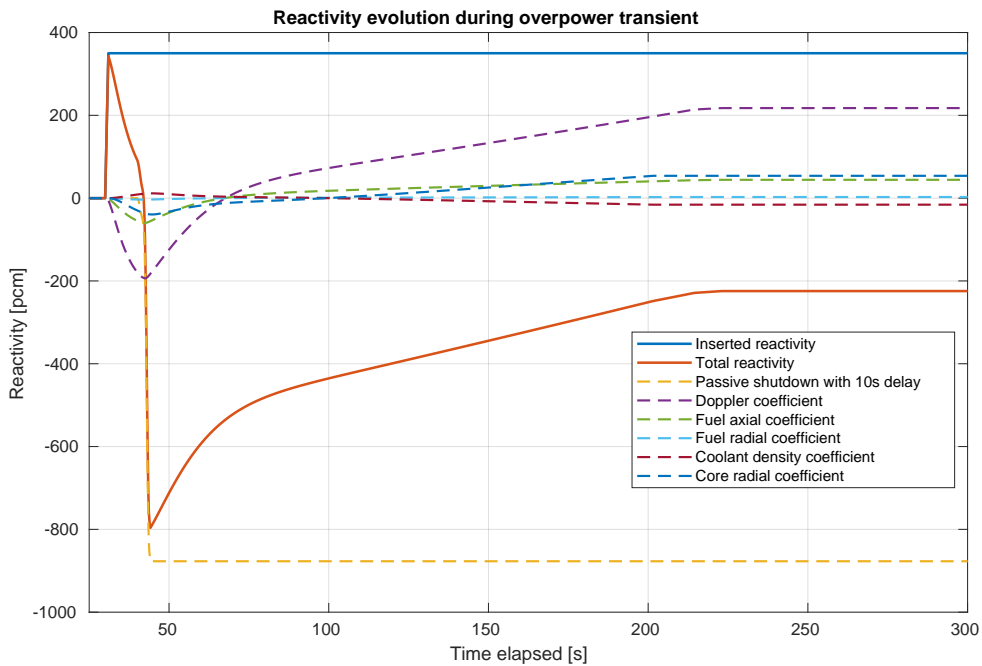


Figure A.6: Reactivity coefficient contribution during transient overpower scenario

Flow rate changes in different scenarios, for a transient of insertion of 350pcm .

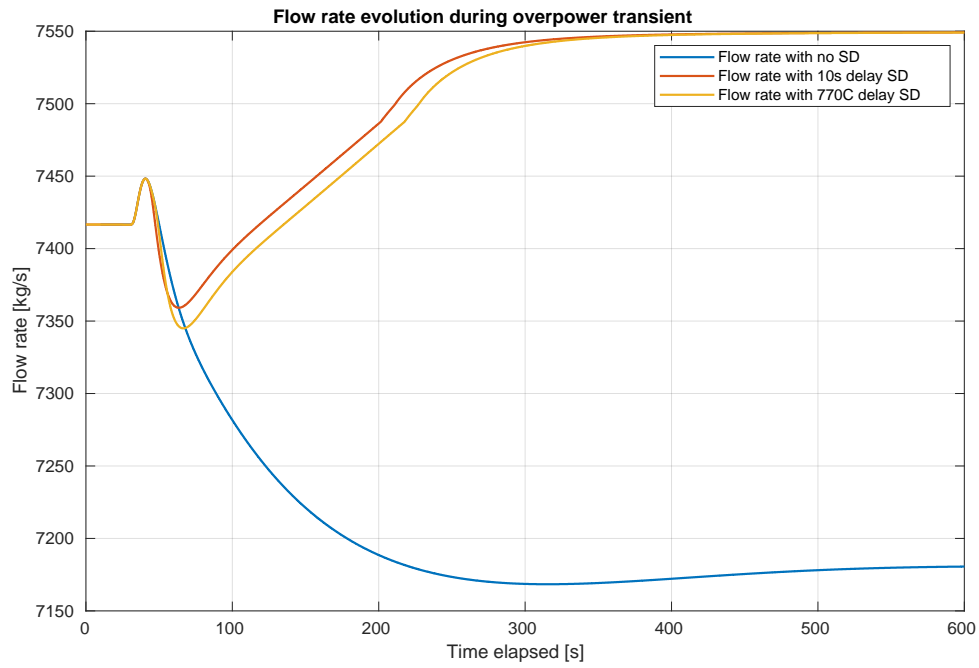


Figure A.7: Coolant flow rate changes during transient overpower scenario

Results for a transient of insertion of 120pcm in 1s is provided here.

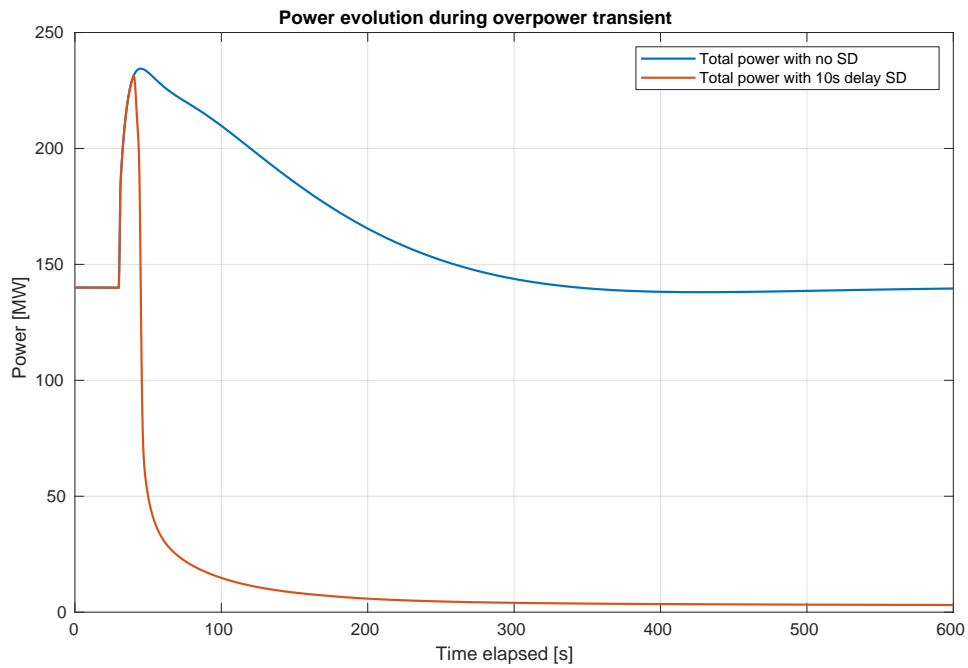


Figure A.8: Total power changes during transient overpower scenario

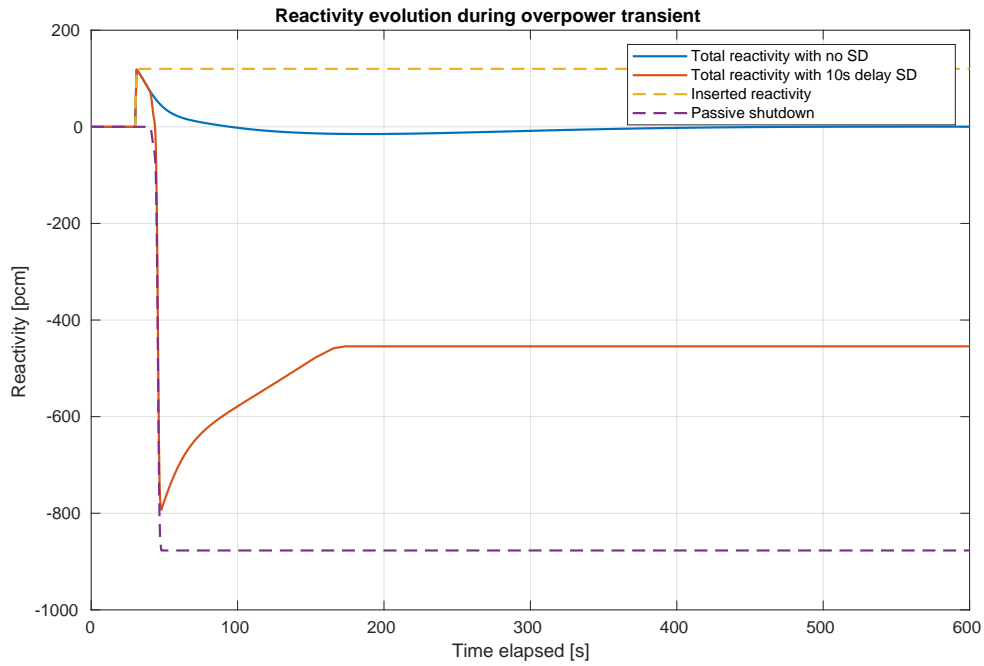


Figure A.9: Total reactivity changes during transient overpower scenario

It should be noticed here that the temperatures of the coolant outlet, see Figure A.10, does not go beyond 770°C to trigger self actuated insertion, and relies on reactivity feedback to return to normalcy.

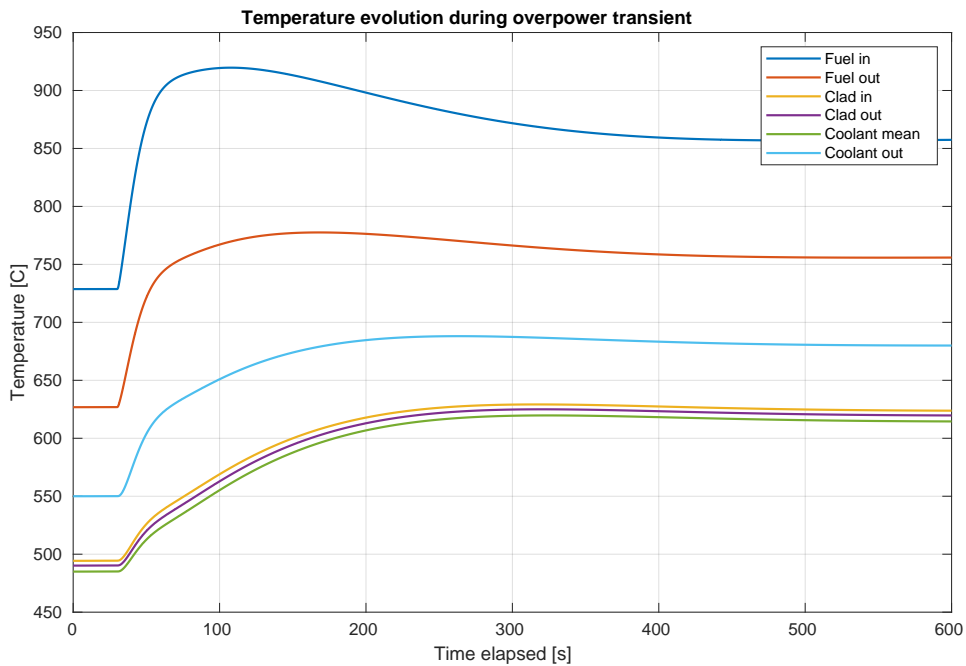


Figure A.10: Temperature changes during transient overpower scenario

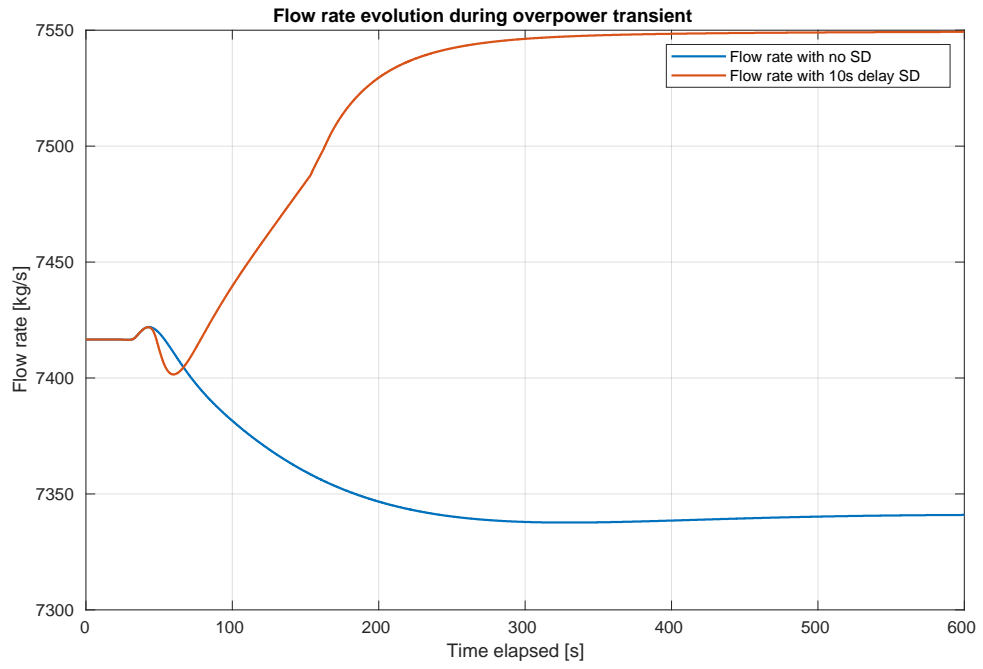


Figure A.11: Coolant flow rate changes during transient overpower scenario

TRITA SCI-GRU 2019:127